공학박사학위논문

환경 및 운행적 불확실성에 강건한 유성 기어박스의 진동기반 고장진단

Robust vibration-based fault diagnosis of a planetary gearbox under environmental and operational uncertainties

2017 년 08 월

서울대학교 대학원
기계항공공학부
하 종 문

Abstract

Robust vibration-based fault diagnostics of a planetary gearbox under environmental and operational uncertainties

Jong Moon Ha
Department of Mechanical and Aerospace Engineering
The Graduate School
Seoul National University

Vibration-based fault diagnosis of planetary gearboxes can effectively prevent many undesired failures and thereby reduce the maintenance costs of large-scale engineering systems. However, this type of fault diagnosis is often challenging due to various uncertainties, such as the uncertain operating conditions that affect the vibration characteristics of the gearbox. To cope with the uncertainty-related challenges of vibration-based fault diagnosis of planetary gearboxes, this thesis presents three research thrusts: 1) quantitative definition of the stationary operating condition of a gearbox, 2) data-efficient fault diagnosis using autocorrelation-based time synchronous averaging (ATSA), and 3) tooth-wise fault identification using a health data map (HDmap), without the use of an encoder system. The first research thrust presents a class-wise fault diagnosis methodology to solve the challenges that arise from the uncertain operating conditions of a gearbox. In the proposed method, the operating condition of the gearbox is quantitatively divided into multiple classes in such a way that the vibration signals in each class are homogeneous. The second research thrust presents a data-efficient time synchronous averaging (TSA) method

for a planetary gearbox. To enhance the signal-to-noise ratio, conventional TSA for a planetary gearbox extracts the vibration signals using a narrow-range window function, which requires a significant amount of stationary vibration signals. However, in practice, stationary vibration signals are rarely obtainable due to the uncertain operating conditions of the system. In this research, an autocorrelation function is used to extend the range of the window function to enable reliable fault diagnosis, even with a small amount of stationary vibration signals. The third research thrust proposes an original idea for tooth-wise fault identification of a planetary gearbox. The proposed method is based on a health data map that can be used even with uncertain vibration characteristics. The two-dimensional health data map can sketch the health data corresponding to every pair of gear teeth to isolate the location of the faulty gear tooth. In addition, a Hilbert transform-based phase estimation technique is employed for an encoder-less health data map that is suitable even under the slightly varying rotational speed.

Keywords: Fault diagnosis
Planetary gearbox
Classification of operating condition
Autocorrelation-based time synchronous averaging
Health data map

Student Number: 2013-30953

Table of Contents

Abstract ..... **i**

Nomenclatures ..... **xv**

Chapter 1. Introduction **1**

1.1 Motivation 1

1.2 Scope of Research 2

1.3 Structure of the Thesis 6

Chapter 2. Technical Background and Literature Review **7**

2.1 Fault Diagnosis of a Gearbox uncer the Varying Operating Condition ... 7

2.2 Fault Diagnosis of a Spur Gearbox 10

2.2.1 Time Synchronous Averaging 10

2.2.2 Definition of Residual Signal and Difference Signal 13

2.2.3 Definition of Health Data (HD) 14

2.2.4 Local Meshing Plane 20

2.3 Fault Diagnosis of a Planetary Gearbox 22

2.3.1 Dynamics Characteristics of Planetary Gearbox 22

2.3.2 Time Synchronous Averaging for a Planetary Gearbox with Window Function 26

2.4 Summary and Discussion 31

Chapter 3. Analytical Model and Testbed for Planetary Gearbox 37

3.1 Analytical Model for Planetary Gearbox.....37

3.1.1 Analytical Model for Normal Condition 37

3.1.2 Examining Faults for the Analytical Model.....39

3.2 Testbed for Planetary Gearbox 41

Chapter 4. Quantitative Definition of the Stationary Operating Condition 44

4.1 Analytical Modeling of Wind Turbine (WT) Performance.....45

4.2 Mathematical Derivation of the PDF of Power and Rotor Speed 48

4.2.1 The *PDF* of Power 49

4.2.2 The *PDF* of Rotor Speed.....52

4.3 Classification of the Operating Conditions of a WT.....54

4.3.1 A Classification Method for Operating Conditions of a WT.....54

4.3.2 Definition of Quantitative Classification Criteria 57

4.4 Case Studies.....63

4.4.1 Case Study with the Analytical WT Model.....64

4.4.2 Case Study with a 2.5 Megawatt Wind Turbine 66

4.5 Validation Study for Classification of Stationary Operating Conditions69

4.5.1 Homogeneity Evaluation of the Vibration Signals.....70

4.5.2 Vibration-based Condition Monitoring 71

4.6 Summary and Discussion 73

Chapter 5. Autocorrelation-based Time Synchronous Averaging (ATSA) 76

5.1 Monitoring Position and Meshing Tooth of Planet Gears 76

5.2 In-depth Study on the Autocorrelation Function for Vibration Signals 78

5.3 Autocorrelation-based TSA 81

5.3.1 Representative Autocorrelation Function 81

5.3.2 Design of the Window Function 82

5.3.3 Application of Window Function for TSA 85

5.4 Case Studies 87

5.4.1 Case Study #1: Analytical Model 88

5.4.2 Case Study #2: Testbed 89

5.5 Summary and Discussion 92

Chapter 6. Tooth-wise Fault Identification of Gearbox using Health Data Map (HDMap) 94

6.1 TSA and Difference signal for One Hunting Tooth Cycle (HTC) in Sample Domain 95

6.2 Health Data for One Hunting Tooth Cycle (HTC) in Sample Domain 97

6.3 Health Data (HD) in Tooth Domain: HDmap 101

6.4 Encoder-less Health Data Map 104

6.5 Case Study 106

6.5.1 Case Study #1: Analytical Model 106

6.5.2 Case Study #2: Testbed 111

6.6 Summary and Discussion 120

Chapter 7. Conclusions **122**

7.1 Contributions and Significance 122

7.2 Suggestions for Future Research 124

References **128**

Abstract (Korean) **143**

List of Tables

Table 2-1 List of health data 16

Table 4-1 Classification criteria defined using Methods 1 and 2 for the WT model with different levels of uncertainties 65

Table 4-2 The criteria for defining the stationary operating condition of the on-shore WT, as defined based on the two proposed methods 67

List of Figures

Figure 2-1 Active power bins proposed by IEC 8

Figure 2-2 Condition monitoring scheme suggested by DNV GL 9

Figure 2-3 Concept of “active range”: (a) proposed by SKF, and (b) proposed by Oneprod 10

Figure 2-4 Procedures of conventional TSA for a spur gear 12

Figure 2-5 Local meshing plane of a spur gearbox with configuration of Z_a=7 and Z_b=5: (a) divided vibration signal based on tooth meshing period and (b) vibration signal represented in tooth domain. 22

Figure 2-6 Planetary gearbox 23

Figure 2-7 Representative window functions for TSA for a planetary gearbox: (a) full range view and (b) narrow range view. 26

Figure 2-8 TSA for a planet gear in planetary gearbox with configuration of Z_r=95, Z_p=31 and Z_s=31 28

Figure 2-9 TSA for a sun gear in planetary gearbox with configuration of Z_r=99, Z_p=35 and Z_s=27 30

Figure 2-10 Position of gears where each planet gear is positioned under the sensor 33

Figure 3-1 Analytical model of planetary gearbox: (a) Planet # 1, (b) Planet # 2, (c) Planet # 3, and (d) combined signal. 39

Figure 3-2 Simulation of faulty condition of the analytical model: (a) Fault of a planet gear, (b) Fault of a sun gear meshing with planet # 1, (c) Fault of a sun gear meshing with planet # 2, (d) Fault of a sun gear meshing with planet # 3 40

Figure 3-3 Testbed for planetary gearbox 42

Figure 3-4 Target planetary gearbox: (a) overview of the gearbox and (b) inner side of the gearbox 43

Figure 3-5 Fault of the gears: (a) fault of a planet gear with two thin lines, (b) partial tooth breakage of a planet, (c) line-type fault of a planet gear and (d) line-type fault of a sun gear 43

Figure 4-1 Region of wind speed for control of wind turbines: (a) wind speed-power relationship and (b) wind speed-rotor speed relationship 46

Figure 4-2 The probability density functions (PDFs) of wind speeds modeled by Rayleigh distribution with the average wind speeds of 7.5 m/s, 8.5 m/s, and 10 m/s. 48

Figure 4-3 The CDF and PDF of power: (a) the CDF of power, (b) the PDF of power and (c) the PDF of power with uncertainties. 52

Figure 4-4 The CDF and PDF of rotor speed: (a) the CDF of rotor speed, (b) the PDF of rotor speed and (c) the PDF of rotor speed with uncertainties 54

Figure 4-5 The proposed classification rule for operating conditions of a wind turbine. 55

Figure 4-6 Sample results of the proposed method for classification of operating conditions of a wind turbine. 56

Figure 4-7 The probability density function (PDF) for the operating conditions of the WT model around the rated condition where an average wind speed of 7.5 m/s was used: (a) power and (b) rotor speed. 59

Figure 4-8 The probability density function (PDF) for operating conditions using a WT model fitted by a Gaussian mixture model with four Gaussian distributions where average wind speed of 7.5 m/s was used: (a) power and (b) rotor speed. 62

Figure 4-9 Criteria for the stationary operating condition where solid vertical lines represent the results from Method 1 and dashed vertical lines represent the results from Method 2: (a)-(c) power with average wind speed of 7.5, 8.5, and 10 m/s, respectively and (d)-(f) rotor speed with average wind speed of 7.5, 8.5, and 10 m/s, respectively. 64

Figure 4-10 A three-dimensional histogram of power and rotor speed of the on-shore WT for one year: (a) full data and (b): data in which power is zero are filtered out. 66

Figure 4-11 A relative histogram of the operating conditions of a WT for one year. Data in which power is equal to zero are filtered out for graphically tidy representation: (a) power and (b) rotor speed. 67

Figure 4-12 Classification results of the wind turbine data. 68

Figure 4-13 Representative operating conditions for control of the WT testbed: (a) Class I, (b) Class II and (c) Class III. 70

Figure 4-14 Homogeneity evaluation results of the vibration signals: (a) Class I, (b) Class II and (c) Class III 71

Figure 4-15 *FM0* obtained from normal and anomaly conditions of the planetary gearbox: (a) Class I, (b) Class II and (c) Class III. 72

Figure 4-16 *FM0* obtained from normal and anomaly conditions of the planetary gearbox without considering operating condition. 73

Figure 5-1 Meshing tooth matrix of the planet gear and the ring gear. 77

Figure 5-2 Autocorrelation function of vibration measured from a sensor attached to a gearbox housing. 79

Figure 5-3 Meshing condition and transfer path along with rotation of planet gear. 80

Figure 5-4 Representative autocorrelation function: (a) for 1 HTC and (b) for the period of one-tooth meshing around 46 rotations of the planet gear. .. 82

Figure 5-5 Maximum distance of the planet gear of interest to the sensor and corresponding position of the gears. 83

Figure 5-6 Derivation of the window function based on representative autocorrelation function: (a) extraction of window function and (b) window function along with ring gears' tooth. 84

Figure 5-7 Autocorrelation-based window function. 85

Figure 5-8 Averaging of signal for ATSA. 86

Figure 5-9 DIF of vibration signal produced by a planet gear from the simulation: (a) data length: 393 carrier cycles and (b) data length: 131 carrier cycles. 89

Figure 5-10 Two health data (*FM4* and *M6A*) using 393 carrier cycles of operational data measured from the testbed: (a) processed with TSA and (b) processed with ATSA. 91

Figure 5-11 Two health data (*FM4* and *M6A*) using 131 carrier cycles of operational data measured from the testbed: (a) processed with TSA and (b) processed with ATSA 91

Figure 5-12 Three health data (*FM4*, *M6A* and *FM0*) using 131 carrier cycles of operational data measured from the testbed: (a) processed with TSA and (b) processed with ATSA. 92

Figure 6-1 Procedures for calculating time synchronous averaging signal and difference signal for one hunting tooth cycle 95

Figure 6-2 FM4 with sliding window: (a) difference signal and (b) enveloped FM4 with the sliding window. 100

Figure 6-3 Meshing tooth matrix of a ring gear and a planet gear for one hunting tooth cycle 101

Figure 6-4 Health data map using an enveloped difference signal: (a) fault of a planet gear and (b) fault of a sun gear. 104

Figure 6-5 Health data map: (a) Difference signal for planet gear fault, (a) Difference signal for sun gear fault, (a) FM4 for planet gear fault and (d) FM4 for sun gear fault 107

Figure 6-6 Positions of the planet gears: (a) initial state and (b) instance that the faulty tooth of the sun gear meshes with planet #2 under the sensor. 108

Figure 6-7 Typical range of the tooth-meshing matrix of a ring gear and a planet gear when the faulty tooth of the planet gear is engaged under the sensor 109

Figure 6-8 Health data map with noise of 0.1: (a) Difference signal for planet gear fault, (b) Difference signal for sun gear fault, (c) FM4 for planet gear fault and (d) FM4 for sun gear fault 110

Figure 6-9 Fault diagnosis performance of maximum values of an enveloped difference signal and *FM4*, along with the size of noise: (a) fault of a planet gear and (b) fault of a sun gear. 111

Figure 6-10 Planetary gearbox with two sensors 112

Figure 6-11 Health data map using an enveloped difference signal: (a) fault of a planet gear with Sensor #1, (b) fault of a sun gear with Sensor #1, (c) fault of a planet gear with Sensor #2, (d) fault of a sun gear with Sensor #2. 114

Figure 6-12 Health data map using an enveloped *FM4*: (a) fault of a planet gear with Sensor #1, (b) fault of a sun gear with Sensor #1, (c) fault of a planet gear with Sensor #2, (d) fault of a sun gear with Sensor #2. 115

Figure 6-13 Difference signal from sensor # 1 using conventional TSA with five-teeth Tukey window function: (a) fault of a planet gear and (b) fault of a sun gear 116

Figure 6-14 Difference signal from sensor # 1 using TSA with adjusted position of the window function: (a) fault of a planet gear with window positioned around T_r=43 and (b) fault of a sun gear with window positioned around T_r=7 116

Figure 6-15 Phase estimation results: (a) fault of a planet gear with Sensor #1, (b) fault of a sun gear with Sensor #1, (c) fault of a planet gear with Sensor #2, (d) fault of a sun gear with Sensor #2. 118

Figure 6-16 Health data map using an enveloped difference signal without encoder system: (a) fault of a planet gear with Sensor #1, (b) fault of a sun gear with Sensor #1, (c) fault of a planet gear with Sensor #2, (d) fault of a sun gear with Sensor #2. 119

Figure 6-17 Health data map using an enveloped *FM4* without encoder system : (a) fault of a planet gear with Sensor #1, (b) fault of a sun gear with Sensor #1, (c) fault of a planet gear with Sensor #2, (d) fault of a sun gear with Sensor #2. 120

Nomenclatures

v_{re}	Resampled vibration signal
v_{TSA}	Vibration signal processed with time synchronous averaging (TSA)
v_{RES}	Residual signal
v_{DIF}	Difference signal
$\mu_{(\cdot),i}$	i^{th} statistical moment of the target signal $(\cdot)$
$A(f_i)$	Amplitude of i^{th} gear mesh frequency (GMF)
$A(s_i^{fj})$	Amplitude of i^{th} sideband of j^{th} GMF
N_p	The number of planet gears
Z_r	The number of teeth of the ring gear
Z_p	The number of teeth of the planet gear
T_s	Tooth number of the sun gear
T_r	Tooth number of the ring gear
T_p	Tooth number of the planet gear
T_s	The number of teeth of the sun gear
n_c	The number of rotation of the carrier
n_{pr}	The number of rotation of the planet gear relative to the ring gear
HTC_p	Hunting tooth cycle for the planet gear
HTC_s	Hunting tooth cycle for the sun gear
$n_{c\|reset\_p}$	The number of carrier rotation for HTC_p
$n_{c\|reset\_s}$	The number of carrier rotation for HTC_s
$n_{pr\|reset\_p}$	The number of rotation of the planet gear for HTC_p
v_{win}	Windowed vibration signal
v_n	Vibration signal generated from n^{th} planet gear
a_n	Signal transfer function of n^{th} planet gear

A_{noise}	Noise factor
r	Non-coherent random noise
w_c	Rotational speed of the carrier
ψ_n	Position of the n^{th} planet gear in angle
v	Wind speed
$v_{cut\text{-}in}$	Cut-in wind speed
v_{rated}	Rated wind speed
P	Power
w	Rotor speed
P_n	Power with Gaussian noise
w	Rotor speed with Gaussian noise
ε	Gaussian noise
$F_{(\cdot)}$	Cumulative density function (CDF) of (·)
$f_{(\cdot)}$	Probability density function (PDF) of (·)
C_p	Criterion of power for stationary operating condition
C_w	Criterion of rotor speed for stationary operating condition
f_{rev_pr}	The number samples assigned during one rotation of the pla net gear relative to the ring gear
M_p	Meshing tooth matrix of the planet gear
M_r	Meshing tooth matrix of the ring gear
R_{vv}	Autocorrelation function of resampled vibration signal
$R_{vv(i)}$	Autocorrelation function during i^{th} *HTC*
$\bar{R}_{vv}$	Representative autocorrelation function
n_{near}	Number of rotations of the planet gear at which the planet gear of interest is near the sensor
D_{max}	Maximum distance of the planet gear to the sensor
v_{trans}	Transformed vibration signal
W_{trans}	Transformed window function

$v_{(i,k)}$	k^{th} teeth meshing vibration vector of tooth number i of the planet gear
$W_{(i,k)}$	k^{th} window vector of tooth number i of the planet gear
v_{DIF_env}	Enveloped difference signal in sample domain
$FM4\_env$	Enveloped FM4 in sample domain
T_{pf}	Fault characteristics period of planet gear
T_{sf}	Fault characteristics period of sun gear
M_{p_con}	Continuous meshing tooth matrix of the planet gear
M_{r_con}	Continuous meshing tooth matrix of the ring gear
$HDmap_{DIF\_planet}$	Health data map using v_{DIF_env} for planet gear fault
$HDmap_{DIF\_sun}$	Health data map using v_{DIF_env} for sun gear fault
$HDmap_{FM4\_planet}$	Health data map using $FM4\_env$ for planet gear fault
$HDmap_{FM4\_sun}$	Health data map using v_{DIF_env} for sun gear fault

Chapter 1. Introduction

1.1 Motivation

Large-scale engineering systems, such as wind turbines (WTs) and helicopters, often suffer from high maintenance costs and downtime due to undesired failures. Y. Feng et al. found that operation and maintenance costs account for 18% of total cost of energy (COE) in offshore WTs, and 12% of the total COE in onshore WTs [1]. J. Land reported that the maintenance cost of helicopters accounts for 24% of operating cost [2]. Condition-based maintenance (CBM) can effectively prevent many undesired failures and thereby reduce system maintenance costs. David McMillan et al. studied the benefits of CBM for wind turbines and concluded that 76,784£ can be saved from the maintenance costs of each offshore wind turbine per year with the proper use of CBM. [3]. Honeywell reported that 75% of unscheduled maintenance of an aircraft (which costs about $75,500 USD per system) can be saved annually with CBM [4].

One of the most critical components for CBM in large-scale engineering systems (such as wind turbines and helicopters) is the planetary gearbox. This is because unexpected failure of a gearbox leads to significant downtime loss [5]. Thus, there have been a variety of attempts to diagnose faults of planetary gearboxes by monitoring various parameters, such as oil quality, oil temperature, and vibration signals. Among the various approaches available, vibration-based fault diagnosis is considered to be the most efficient and effective.

Despite relevant prior studies, currently available signal processing techniques for vibration-based fault diagnosis of planetary gearboxes are still challenging for several reasons that arise from environmental and operational uncertainties. First, vibration signals are heterogeneous and non-stationary due to the uncertain nature of the operating conditions of a gearbox [6]. There are a considerable amount of works reporting that the vibration signals are dependent to the varying load [7]–[14] and rotating speed [15]–[18]. It is thus often challenging to evaluate the conditions of a system using readily-available signal processing techniques (e.g., fast Fourier transform). Second, conventional signal processing techniques require an extensive amount of stationary vibration signals; these cannot be measured in the field due to environmental and operational uncertainties. Third, the vibration modulation characteristics of the gearbox, which should be identified for condition monitoring, are frequently unknown or uncertain. Undesired vibration modulation characteristics can be made by various factors including design and manitenance issues such as a flexible ring gear rim [19], gear manufacturing errors [20], [21], assembly errors [22] and varying radial load [23]. Fourth, gearboxes must be equipped with a high-cost encoder system to process the vibration signals under the varying operating conditions with uncertainties. These high-cost systems are not typically available in real-world settings.

1.2 Scope of Research

To cope with the abovementioned uncertainty-related issues, this thesis

proposes three key ideas in the following research thrusts: 1) quantitative definition of the stationary operating condition of a gearbox, 2) data-efficient fault diagnosis using autocorrelation-based time synchronous averaging (ATSA), 3) tooth-wise fault identification under unexpected vibration characteristics using a health data map (HDMap), without using an encoder system.

Research thrust 1: Quantitative definition of the stationary operating condition of a gearbox

The first research thrust presents a general method that can be used to classify the operating condition of a gearbox in terms of rotating speed and power to aid in the selection of an optimal operating condition for CBM [24]. Five distinct classes are defined in such a way that the gearbox in each particular class has unique operating characteristics, thus leading to homogeneous vibration signals in each class. In particular, to produce the most valuable vibration signal for condition monitoring of a gearbox, quantitative criteria for the stationary operating condition are defined, while considering inherent randomness in the performance of the system. In this research thrust, a representative case study is presented that examines wind turbines.

Research thrust 2: Data-efficient fault diagnosis of a planetary gearbox using autocorrelation-based time synchronous averaging (ATSA)

Time synchronous averaging (TSA) is known to be effective for vibration-based fault diagnosis of a planetary gearbox. To perform TSA, narrow-range window functions are used to extract the vibration signals of interest to enhance the signal-to-noise ratio. However, use of the narrow-range window function requires an extensive amount of stationary vibration signals; these are difficult to measure in real-world field settings. Research thrust 2 proposes autocorrelation–based time synchronous averaging (ATSA) to cope with the aforementioned challenge associated with the current practice of TSA with its narrow-range window functions [24]. In the proposed approach, an autocorrelation function, which represents physical interactions between the ring, sun, and planet gears, is used to extend the range of the window function, while optimizing shapes based on actual kinetic responses of the planetary gearbox.

Research thrust 3) Tooth-wise fault identification under unexpected vibration characteristics using a health data map (HDMap)

Vibration characteristics are frequently unknown or unexpected due to various operational uncertainties, such as varying torque, radial load, and assembly & manufacturing tolerances. This thesis proposes an original idea for tooth-wise fault identification of a planetary gearbox that is based on a health data map. The proposed method can be used even with unexpected vibration characteristics. Enveloped kurtosis in a moving window is calculated for the health data in the

sample domain and aligned on a health data map in the domains of a pair of gear teeth (i.e., ring-planet gear teeth pairs and ring-sun gear teeth pairs); this leads to a synthesized visualization of faults in planet gears and a sun gear. In addition, an encoder-less health data map is also proposed to avoid using a high-cost encoder system; such systems are frequently not available in real-world applications. In this method, Hilbert-based phase estimation is employed to obtain rotational information. Based on this information, a rough resampling is performed. With the roughly resampled vibration signal, a health data map can be drawn to visually detect the fault(s) of the gears.

1.3 Structure of the Thesis

This thesis is organized as follows. Chapter 2 presents a technical background and literature review of conventional vibration-based fault diagnosis for planetary gearboxes. Chapter 3 introduces an analytical model and a testbed of a planetary gearbox, which is used to demonstrate the fault diagnosis method proposed in this thesis. In Chapter 4, the stationary operating condition of a gearbox is quantitatively defined in terms of rotating speed and power. To demonstrate the proposed technique, a representative case study is presented that examines wind turbines. Chapter 5 proposes autocorrelation-based time synchronous averaging (ATSA). The proposed method is more efficient than conventional TSA that uses narrow-range window function. Chapter 6 introduces procedures for tooth-wise fault identification of a planetary gearbox under the unexpected vibration characteristics. The new method uses the original idea of a health data map (HDMap). In addition, Hilbert transform-based phase estimation is applied to the vibration signal for an encoder-less HDmap. Chapter 7 summarizes the thesis and presents the conclusions, along with suggestions for future research.

Chapter 2. Technical Background and Literature Review

2.1 Fault Diagnosis of a Gearbox uncer the Varying Operating Condition

Due to the uncertain nature of environmental and operational condition, heterogeneous and non-stationary vibration signals are prevalent during the operation of a engineering system. There are a considerable amount of works reporting that the vibration signals are dependent to the varying load [7]–[14] and rotating speed [15]–[18]. Thus, it is often challenging to evaluate the conditions of the system using readily-available signal processing techniques (e.g., fast Fourier transform) which is vulnerable to heterogeneous and non-stationary vibration signals [25], [26].

To cope with the challenges that arise from the varying operating condition for fault diagnosis, a considerable number of researches have been made. Bartelmus and Zimorz (2009) developed a spectrum based feature model that is dependent to the rotating speed of the gearbox [27]. Bertelmus et al. (2010) advanced the previous work by incorporating the dynamics model that describe the speed and load variation for fault diagnosis of the gearbox [15]. Villa et al. (2012) also found that the diagnosis features are dependent to the rotating speed and load of the gearbox [17]. In [17], speed and load data are used to develop a statistical fault model that has high significance when the gearbox is faulted. Zappala et al. from national renewable energy laboratory (NREL) reported that

the fault diagnosis feature is dependent to the power of wind turbine [9]. Thus, fault diagnosis was independently performed at each load condition using a spectrum based feature [9]. Bartelmus and Zimorz (2009) found that the load variation affect level of the amplitude modulation of vibration signal when the gear is faulted [23]. Zappala et al. (2013) [9] and Zimroz el al. (2014) [7] developed fault feature curves along with the level of power that affects the vibration amplitudes. Toshkova et al. suggested to consider power and speed variation simultaneously for fault diagnosis because they affect the level of fault diagnosis features [16].

Despite the relevant studies to consider the variation of operating conditions, they are not consistent and generalized. An alternative approach is to adaptively use homogeneous vibration signals across a limited range of operating conditions of the system. For example, the International Electrotechnical Commission (IEC), an organization that proposes international standards for wind turbine condition monitoring, has recommended that “active power bins” should be used to classify the range of power as shown in Figure 2-1 [28]. Vibration signals in a particular

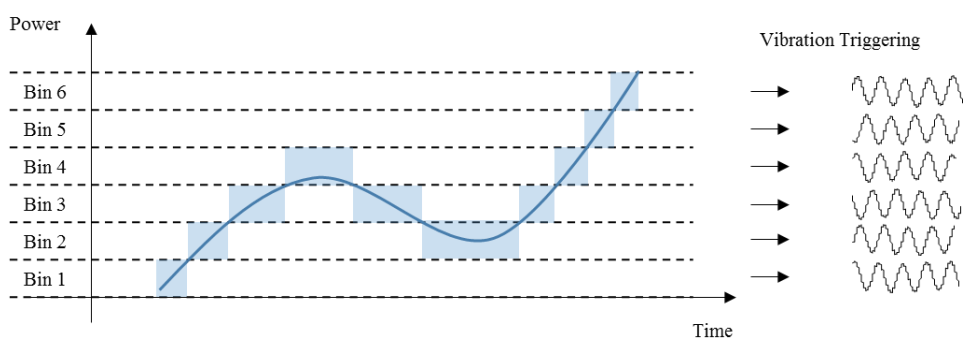

Figure 2-1 Active power bins proposed by IEC

bin are more homogeneous and exhibit only small variations. Thus, it would be expected that a condition monitoring technique could be effectively used with each bin due to the homogeneous nature of the vibration signals in that "bin."

However, it is well known that vibration characteristics are also dependent on rotational speed [17], [29]. Therefore, the IEC's recommendation of using "active power bins" is not appropriate when rotational speed fluctuates. Another organization, DNV GL, proposed a renewables certification that divides the operating conditions of the system into two parts based on the amount of variation of the rotational speed of the system as shown in Figure 2-2 [30]. In this strategy, computationally efficient signal processing techniques (such as fast Fourier transform) are used only when the system operate with minimal speed variation. When the system operate with frequent speed variation, it is recommended that more advanced condition monitoring techniques be employed [30].

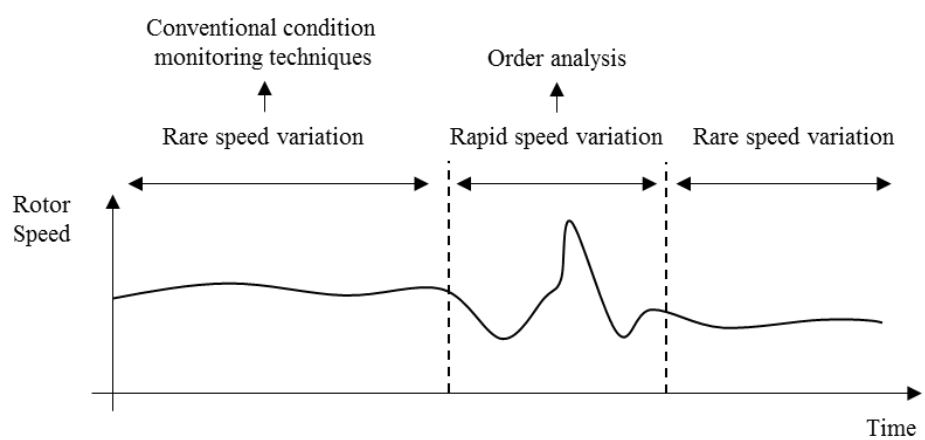

Figure 2-2 Condition monitoring scheme suggested by DNV GL

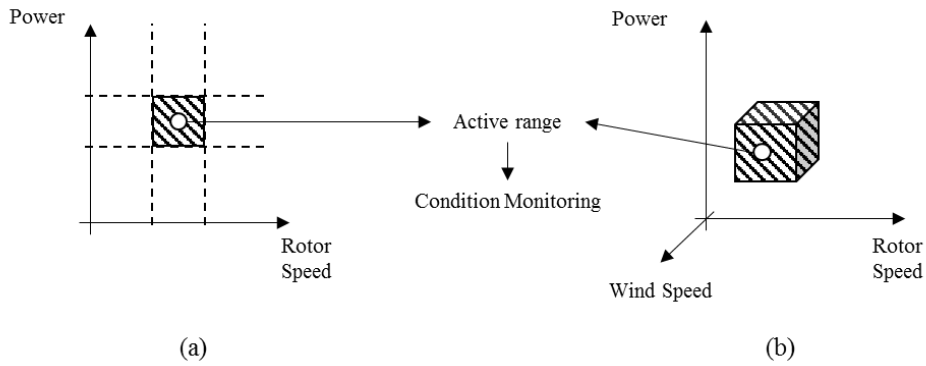

Figure 2-3 Concept of "active range": (a) proposed by SKF, and (b) proposed by Oneprod

To effectively monitor condition of the system, some commercial condition monitoring systems also try to use the existing signal processing techniques only when the systems are operating in a pre-defined narrow range of operating conditions [31]. For example, "Windcon," developed by SKF, uses the concept of an "active range." This strategy performs active condition monitoring only while rotor speed and power remain in the "active range" [32]. The "Oneprod Wind System," developed by Oneprod, uses wind speed as an additional variable for defining the "active" range for condition monitoring [33]. Concepts of "active range" proposed by SKF and Oneprod are compared in Figure 2-3.

2.2 Fault Diagnosis of a Spur Gearbox

2.2.1 Time Synchronous Averaging

Vibration signal measured from a sensor can be expressed as: [34]

$$v(\theta) = S(\theta) + N(\theta) + R(\theta) \tag{2.1}$$

where $S(\theta)$ is the synchronous coherent signal; $N(\theta)$ is the non-synchronous coherent signal; $R(\theta)$ is the non-coherent random signal.

Synchronous coherent signal is produced by meshing of the gear of interest, and non-synchronous coherent signal is generated from other rotating components such as bearings. Non-coherent random signal is considered as Gaussian noise. For condition monitoring of a particular gear of interest, it is essential to extract the synchronous coherent signal while reducing the effect the other components in the signal.

Time synchronous averaging (TSA) is used, among other applications, to isolate the synchronous coherent signal produced by a particular gear of interest from noisy sensory signal for efficient condition monitoring of the gear [35]. The conventional TSA is composed of three main steps as shown in Figure 2-4:

1) Angular resampling of the vibration signal,

2) Dividing the sensory signal into N segments based on the rotational frequency of the gear of interest,

3) Ensemble averaging for the divided segments.

It is worth noting that vibration signals are collected with a pre-determined sampling rate but the system operates with a varying rotational speed in practice. As a result, the divided segments in Figure 2-4 may have different number of samples if the raw vibration signal is used. For TSA, thus, the vibration signals should be resampled so that the number of samples assigned during a single revolution of the gear remains constant [36]. This can be achieved by

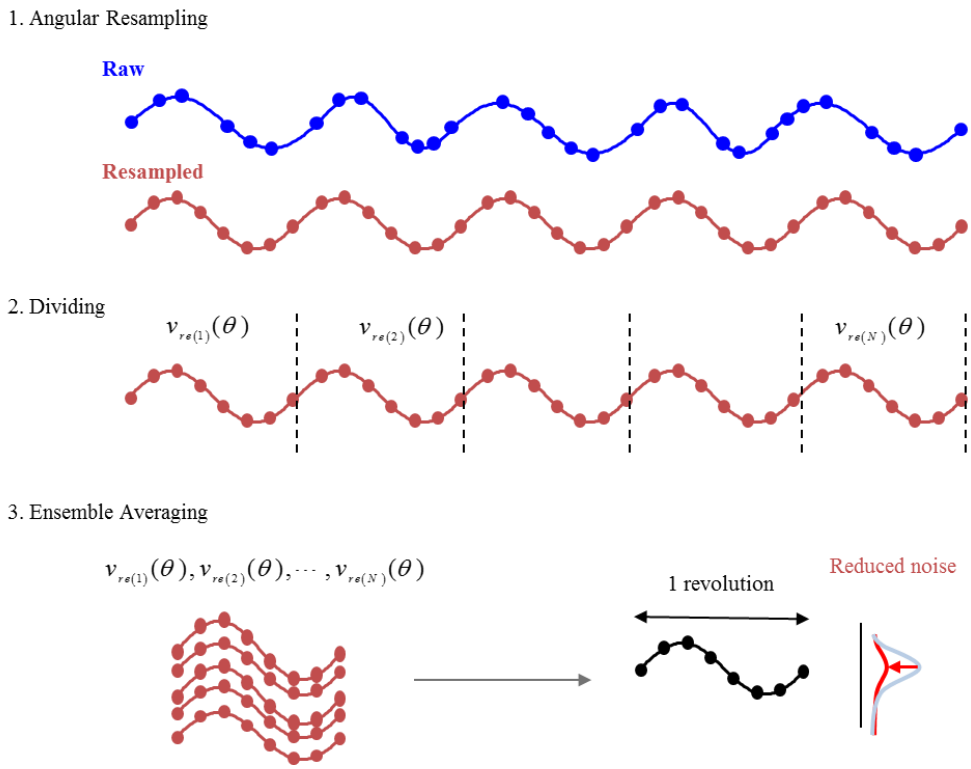

Figure 2-4 Procedures of conventional TSA for a spur gear

interpolating the vibration signal with the constant angle interval of the consecutive samples. There are various interpolation methods for resampling of data such as linear, cubic, and spline interpolation, while a linear interpolation method is known to be efficient in terms of accuracy and computation time [37].

Resampled vibration signal can be simply divided into multiple segments (i.e., $v_{re(i)}(\theta)$) as shown in Figure 2-4 as a second step. TSA signal can be defined by ensemble averaging the divided segments, which is formulated as:

$$v_{TSA}(\theta) = \frac{1}{N}\sum_{i=1}^{N} v_{re(i)}(\theta) \tag{2.2}$$

With TSA, vibration signal produced by the gear of interest remains in its own shape because every divided segment contains similar vibration patterns created by meshing of the gear of interest. On the other hand, non-synchronous coherent signal and non-coherent random signal converges to zero as a considerable number of segments accumulates.

2.2.2 Definition of Residual Signal and Difference Signal

Despite the TSA processing, fault-related features can be buried by the remaining regular components generated from gear meshes. Thus, for an effective fault diagnostics of a gearbox, it is suggested to define residual signal (v_{RES}) or difference signal (v_{DIF}) from the TSA signal (v_{TSA}) [38].

Residual signal is calculated by removing the fundamental gear meshing frequency (GMF) and its harmonics from the TSA signal so that it contains sideband signals [39]. Because the energy contained in the sidebands is related to distributed fault of the gears (e.g., heavy uniform wear of gear teeth) [40], statistical moments of the residual signal can be used as a health data of gearboxes [41].

Difference signal is obtained from TSA signal by excluding sidebands as well as the fundamental GMF and its harmonics. Ideally difference signal should not contain any normal vibration components because there are no primary vibration sources, i.e., vibration due to gear dynamics. Hence, difference signal should follow a Gaussian distribution with a mean of zero (i.e., Gaussian noise) [38]. As the localized faults in a gear (e.g., local crack and spall) exite the systems at the

short-term meshing instances, however, the magnitude of vibration with unexpected frequencies which are out of normal vibration components could become large which would lead to an increase in difference signal [40]. Difference signal is more sensitive to these changes compared to residual signal because rise in any unexpected frequency in vibration will be the only vibration component in difference signal whereas residual signal is dominated by vibration from the sidebands. For this reason, it is useful to track the shape and energy of difference signal to identify the fault of the gearbox.

2.2.3 Definition of Health Data (HD)

There are a number of health data (HD) exploiting residual signal and difference signal to perform fault diagnosis of the gears. For example, a statistical moment for TSA signal, residual signal and difference signal (e.g., mean) can be used as three HDs for fault diagnosis of the gearbox.

M. Lebold et al. (2000) [38], P. Vecer et al. (2005) [42], J. Zakrajsek et al. (1994) [43], A. Aherwal et al. (2012) [44], M. Mosher et al. (2002) [45] and P. Samuel (2005) [41] summarized various health data for fault diagnosis of a gearbox and discussed their physical meanings. In addition, M. Mosher et al. (2002) [45] summarized several health data and suggested their threshold values.

Most health data are related to the i^{th} statistical moment of the target signal (·) which can be defined as:

$$\mu_{(\bullet),\,i} = \frac{1}{N_{samples}} \sum_{n=1}^{N_{samples}} \left[v_{(\bullet)}(n) - \frac{1}{N_{samples}} \sum_{k=1}^{N_{samples}} v_{(\bullet)}(k) \right]^{i} \tag{2.3}$$

where $_{(\cdot)}$ can be $_{(TSA)}$, $_{(RES)}$ or $_{(DIF)}$; $N_{samples}$ is the number of samples of the signal. Health data for fault diagnosis of a gearbox is listed in Table 2-1, and summarized by followings.

Table 2-1 List of health data

Signal	Health data	Physical Meaning
v_{TSA} (TSA signal)	*FM0*	Peak-to-peak normalized by magnitude of GMFs
	SER (Sideband Energy Ratio)	Magnitude of sidebands normalized by magnitude of fundamental GMF
v_{RES} (Residual signal)	*NA4*	4^{th} moment of v_{RES} normalized by previous mean variance
	*NA4**	4^{th} moment of v_{RES} normalized by mean variance at normal condition
	NA4 reset	*NA4* normalized by load (i.e., torque)
v_{DIF} (Difference signal)	*FM4*	Normalized 4^{th} moment of v_{DIF}
	M6A	Normalized 6^{th} moment of v_{DIF}
	M8A	Normalized 8^{th} moment of v_{DIF}
	ER (Energy Ratio)	Energy of difference signal normalized by magnitude of a regular components

FM0

FM0 is the magnitude of peak-to-peak of the waveform normalized by the sum of amplitude of the fundamental gear mesh frequency and their harmonics [46]. M. Alattas et al. (2007) verified it can detect heavy wear and scoring of gears [47]. *FM0* can be defined as:

$$FM0 = \frac{\max(v_{TSA}) - \min(v_{TSA})}{\sum_{i=1}^{N_{harminics}} A(f_i)} \tag{2.4}$$

where $A(f_i)$ is amplitude of i^{th} gear mesh frequency; $N_{harmonics}$ is the number of harmonics.

***SER* (Sideband energy ratio)**

Sideband energy ratio (*SER*) is defined as the magnitude of sidebands normalized by the amplitude of the fundamental gear mesh frequency, which can be formulated by [48]:

$$SER = \frac{\sum_{i=1}^{N_{sidebands}} A(s_i^{f_1})}{A(f_1)} \tag{2.5}$$

where $A(s_i^{f1})$ denotes amplitude of i^{th} sideband of fundamental gear mesh frequency, $N_{sidebands}$ is the number of sidebands. If the defects of a gear become severe, magnitude of sideband will increase compared to the gear mesh

frequency. S. Sheng (2012) from National Renewable Energy Laboratory (NREL) employed *SER* for fault diagnosis of a gearbox in a wind turbine [49].

NA4

J. Zakrajsek el al. (1993) developed *NA4* to detect progress of defect in gears. *NA4* employs information from previous data records as well as the currently acquired data [50]. Information from previous data records, which is calculated as mean variance of residual signal from N_{prev} sets of data, is used to normalize the currently measured fourth moment of residual signal as defined by:

$$NA4 = \frac{\mu_{(RES),4}}{\left\{\frac{1}{N_{prev}}\sum_{j=1}^{N_{prev}}\left[\mu_{(RES_j),2}\right]\right\}^2} \tag{2.6}$$

where N_{prev} is the number of previous sets of data to consider.

NA4*

H. Decker and J. Zakrajsek (1994) revised the *NA4* to reflect the trend of parameters in a statistical manner [51]. The denominator of *NA4* is modified to the second moment of RES of a normal gearbox instead of the previous information. The state of the normal gearbox is defined in a quantitative way where “normal” is assigned to the gearbox until the denominator value exceeds the threshold value (*Thres_NA4**) which is defined as [51]:

$$Thres\_NA4^{*} = \overline{\mu_{(RES),2}} + Z\sqrt{\frac{\mu_{(RES),2}}{N_{samples}}} \tag{2.7}$$

where Z is probability coefficient for a normal distribution

NA4 reset

NA4 is sensitive to the varying torque [14]. Thus, P. Dempsey et al. (2001) proposed NA4 *reset* to minimize the effect of varying torque [14]. The difference from *NA4* is that it resets its denominator when the applied load gets out of the bound which is defined as 10 percent of the current average load.

FM4, M6A* and *M8A

FM4 can be obtained by calculating the normalized kurtosis of difference signal which should follow Gaussian distribution without faults [46]. Thus, the health state of the gearbox can be evaluated by analyzing trend of *FM4*.

$$FM\,4 = \frac{\mu_{(\mathrm{DIF}),4}}{\mu_{(\mathrm{DIF}),2}^{\ 2}} \tag{2.8}$$

H. Martin (1989) developed *M6A* and *M8A* to detect surface damage of gears [52]. The parameters are a revised version of *FM4* where higher moments of the difference signal are employed as:

$$M6A = \frac{\mu_{(\mathrm{DIF}),6}}{\mu_{(\mathrm{DIF}),2}^{\ 3}} \tag{2.9}$$

$$M8A = \frac{\mu_{(\mathrm{DIF}),8}}{\mu_{(\mathrm{DIF}),2}^{\ 4}} \tag{2.10}$$

***ER* (Energy Ratio)**

N. Swansson (1980) proposed to define the energy of difference signal normalized by magnitude of a regular components such as fundamental gear mesh frequency, harmonics and their sidebands as:

$$ER = \frac{RMS_{(DIF)}}{\sum_{i=1}^{N_{harmonics}} \left[A(f_i) + \sum_{j=1}^{N_{sidebands}} A(s_j^{\ f_i}) \right]} \tag{2.11}$$

where $RMS_{(DIF)}$ is root mean square of the difference signal. P. Samuel et al. (2005) reported that *ER* is effective for fault diagnosis of a gearbox because energy of difference signal increases while the magnitudes of regular components decrease when the "heavy uniform wear" occurs to the gear surface.

2.2.4 Local Meshing Plane

Fault of the gears will be represented as anomalies in v_{TSA}, v_{RES} and v_{DIF}. The anomalies in sample domain can be quantified by health data. However,

analyzing periodicity of anomalies is also important [53]. For a general gear system, fault-induced features are generated based on the rotational period of the faulty gear. Thus, frequency analysis of the enveloped signal can be simply used to analyze the periodicity of the anomalies. However, it is time-consuming to check the tooth information and periodicity of the anomaly in sample domain all the time.

The concept of a local meshing plane was proposed to visualize the periodicity of the anomalies of a spur gear system in terms of the gear teeth [54]. Representative values for each tooth-meshing combination are represented in terms of the tooth of a pinion and a gear to evaluate the quality of the gears. Figure 2-5 illustrates the concept of a local meshing plane using a gear pair with 7 and 5 teeth, respectively (i.e., Z_a=7 and Z_b=5, where $Z_{(\cdot)}$ denotes the number of teeth of the gear "(·)"). Because the number of teeth in gear "a" (Z_a=7) and gear "b" (Z_b=5) are relatively prime in this case, the number of tooth-meshing combinations that can be made between the two gears is 35. First, the vibration signal is divided into multiple segments based on the tooth-meshing period, as shown Figure 2-5 (a). Each segment represents the vibration signal from each meshing combination of each tooth pair. From each segment, representative values are defined to quantify the quality of the teeth pairs. In [54], maximum values of the enveloped vibration signal at each segment were employed as the representative values. Calculated values for each tooth-meshing combination can be represented in the tooth domain to enable a visualization of the results, as shown in Figure 2-5 (b). As the gearbox rotates, signals proceed with sequentially increasing tooth numbers of the gears. After one rotation of gear "b"

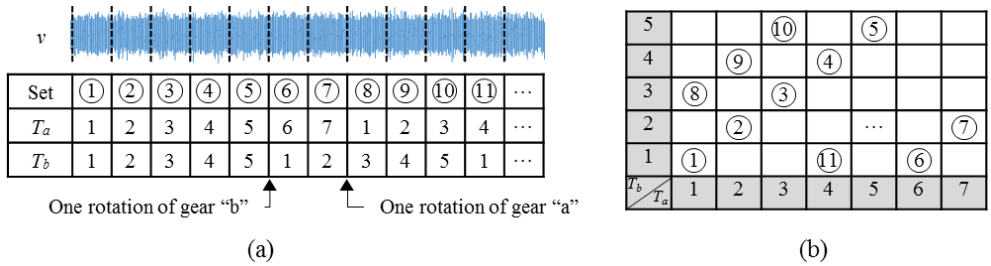

Figure 2-5 Local meshing plane of a spur gearbox with configuration of Z_a=7 and Z_b=5: (a) divided vibration signal based on tooth meshing period and (b) vibration signal represented in tooth domain.

(i.e., ⑤ in Figure 2-5), signals start to proceed from tooth number 1 of gear "b" while the tooth number of gear "a" continues to increase, as indicated by ⑥ in Figure 2-5. For a while after, entire cells in Figure 2-5 (b) are filled with representative values [54]. If a tooth of a gear has a fault, representative values corresponding to the faulty tooth will be highlighted in the meshing plane.

2.3 Fault Diagnosis of a Planetary Gearbox

2.3.1 Dynamics Characteristics of Planetary Gearbox

Planetary gearboxes have four main components, including a ring gear, a sun gear, a carrier, and multiple planet gears. The axes of the planet gears are linked to the carrier, which is connected to the low-speed shaft. A sun gear is connected to the high-speed shaft and meshes with the multiple planet gears simultaneously. Figure 2-6 represents an example of a planetary gearbox with three planet gears; the number of teeth of the ring gear (Z_r), planet gear (Z_p), and sun gear (Z_s) are 95, 31, and 31, respectively. Teeth numbers for the ring gear, planet gear of interest,

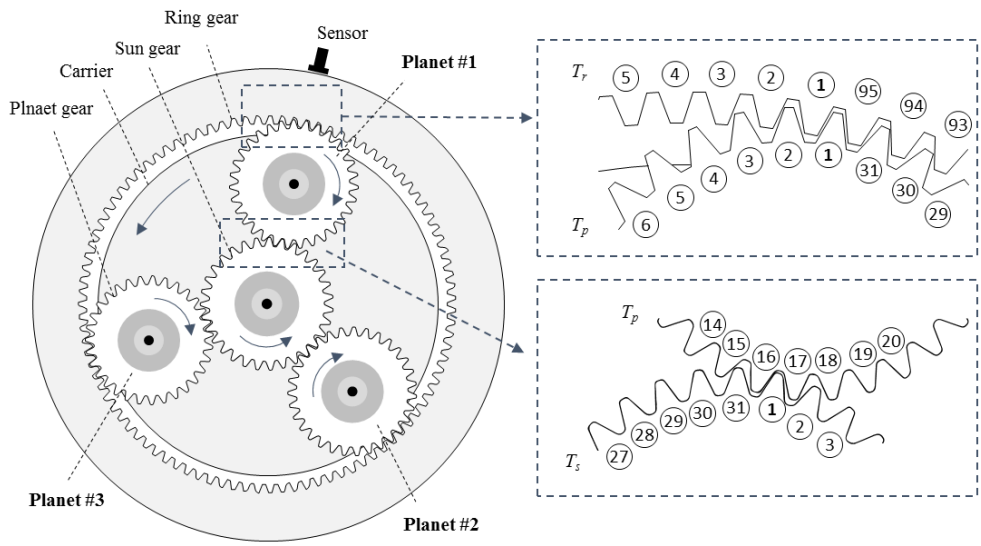

Figure 2-6 Planetary gearbox

and the sun gear (i.e., T_r, T_p, and T_s) can be assigned to each tooth of each gear for further analysis. The meshing of the teeth of the ring gear and the planet gear of interest (indicated as "Planet #1" in Figure 2-6 can be set to be "1" at the initial condition. At the same time, the number "1" can be assigned to the sun gear tooth that meshes with the planet gear of interest.

Vibration generated from meshing of the ring-planet gear pairs and ring-sun gear pairs is mainly transferred to the sensor through the revolving planet gears [55]. Because the signal transfer path is periodically varying due to the revolving nature of the planet gears, the measured vibration signal is modulated. In general, it is assumed that the vibration signal can be most effectively measured at the point when the planet gears are positioned directly under the sensor. It is thus important to identify which tooth of each gear is meshing with the planet gear under the sensor at all times. The tooth number of the planet gear of interest that

meshes with the ring gear (T_p), and tooth number of the sun gear that meshes with the planet gear (T_s) positioned under the sensor at n_c rotations of the carrier can be identified by the following relationships:

$$T_p\left(n_c\right) = \mathrm{mod}\left(n_c Z_r, Z_p\right) + 1 \tag{2.12}$$

$$T_s\left(n_c\right) = \mathrm{mod}\left(n_c Z_r, Z_s\right) + 1 \tag{2.13}$$

where $T_p(n_c)$ is the tooth sequence of the planet gear; $T_s(n_c)$ is the tooth sequence of the sun gear; $mod(a,b)$ is the remainder of a/b; n_c is the number carrier rotations which is zero at the initial condition.

The number of carrier rotations that is required for T_r and T_p or T_r and T_s to reset to be "1" again can be defined by the following expressions:

$$n_{c|\mathrm{reset\_p}} = \frac{LCM\left(Z_r, Z_p\right)}{Z_r} \tag{2.14}$$

$$n_{c|\mathrm{reset\_s}} = \frac{LCM\left(Z_r, Z_s\right)}{Z_r} \tag{2.15}$$

where $LCM(a,b)$ is the least common multiple of a and b.

The number of instances that n_c becomes $n_{c|reset\_p}$ or $n_{c|reset\_s}$ is called a *hunting tooth cycle* for the planet gear (HTC_p) or the sun gear (HTC_s), respectively. For example, $i \cdot n_{c|reset\_p}$ or $j \cdot n_{c|reset\_s}$ rotations of the carrier can be simply denoted as $i \cdot HTC_p$ or $j \cdot HTC_s$, respectively. At every HTC_p, tooth number 1 of the planet gear

of interest (i.e., T_p=1) meshes with the tooth number 1 of the ring gear (i.e., T_r=1) under the sensor. In a similar way, at every HTC_s, tooth number 1 of the sun gear (i.e., T_s=1) meshes with the planet gear of interest that is positioned under the sensor. Data for one HTC_p or HTC_s contain the signals from every possible tooth-meshing combination of ring-planet gear teeth pair and ring-sun gear teeth pair. In some cases, it is meaningful to monitoring position of the planet gears in terms of tooth number of the ring gear. Tooth sequence of the ring gear (T_r), which represents tooth number of the ring gear that meshes with the planet gear at the n_{pr} rotation, can be defined as:

$$T_r\left(n_{pr}\right) = \mathrm{mod}\left(n_{pr}Z_p, Z_r\right) + 1 \tag{2.16}$$

where $T_r(n_{pr})$ is tooth sequence of the ring gear at n_{pr} rotation of the planet gear relative to the ring gear. Hunting tooth cycle for the planet gear can be defined in terms of the number of rotation of the planet gear relative to the ring gear as:

$$n_{pr|\mathrm{reset}\_p} = \frac{LCM\left(Z_r, Z_s\right)}{Z_p} \tag{2.17}$$

For each $n_{c|reset\_p}$ cycles of carrier, planet gear rotates as much as $n_{pr|reset\_p}$ cycles in such a way that Eqs. (2.14) and (2.17) have the following relationship:

$$n_{c|\mathrm{reset}\_s}Z_r = n_{pr|\mathrm{reset}\_p}Z_p \tag{2.18}$$

2.3.2 Time Synchronous Averaging for a Planetary Gearbox with Window Function

TSA for a planetary gearbox is significantly more complicated due to its complex dynamic characteristics, as described above. Unlike spur gears, the axis of the planet gear rotates, as forced by the carrier. Thus, the relative distance of the planet gear from the fixed sensor varies with the rotation of the gears, which leads to challenge in using conventional TSA methods for planetary gearbox. McFadden and Howard (1990) reported that the shorter the relative distance from the sensor to the planet gear of interest, the more accurately the vibration signal of the gear can be measured [56]. Vibration produced by the planet gear of interest, thus, can be monitored by acquiring vibration signals only when the relative distance of the gear from the sensor is short. This is achieved by using window functions that have values only when the planet gear of interest passes the sensor. Thus, various vibration extraction window functions such as

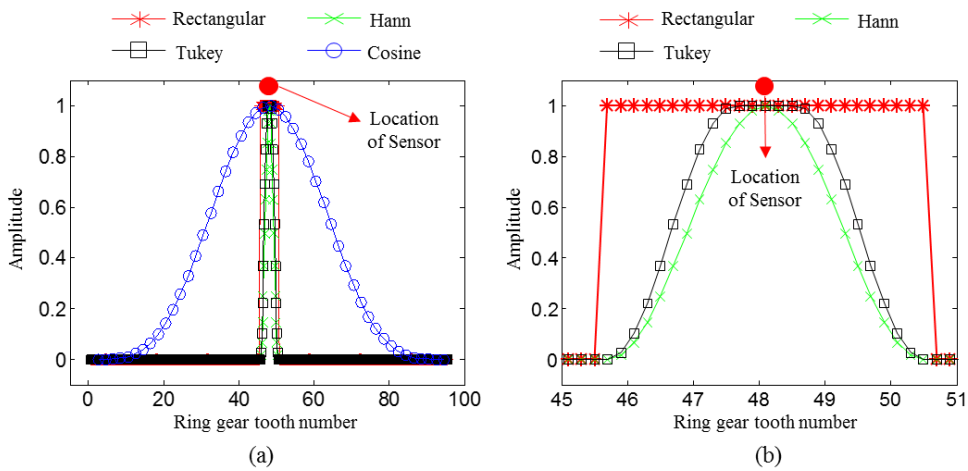

Figure 2-7 Representative window functions for TSA for a planetary gearbox: (a) full range view and (b) narrow range view.

rectangular window [56]–[58], Hann window [59], [60], Tukey window [61], [62], wide-range cosine window [63], [64] and autocorrelation-based window [65] have been proposed as shown in Figure 2-7.

In 1990 and 1991, McFadden firstly proposed a method to separate the vibration signals from the individual planet gears using a rectangular-shape window function [56], [58]. However, rectangular-shape window function causes discontinuity at the end of the window functions. Later, McFadden (1994) investigated various kinds of smooth-edge window functions such as Hann window function to solve the abovementioned challenge [59]. In 2004, Samuel et al. (2004) compared the performance of various window functions for TSA for a planetary gearbox, and reported that the Tukey window function with five-tooth width performs best due to its flat-top and smooth-edge shape [62]. Accordingly, recent studies including Lewicki et al. (2011), Liang et al. (2016), D'Elia et al. (2017), and Wang et al. (2017) employed the Tukey window function for TSA for a planetary gearbox. Lewicki et al. (2011) evaluated performance of TSA with Tukey window function for fault detection of planetary gearbox in helicopters. Liang et al. (2016) extracted vibration signals for each tooth of the planet gear using Tukey window functions for a tooth-wise fault identification of the planet gear. D'Elia et al. (2017) tried to find optimal position of the Tukey window function for TSA using a instantaneous power flow of gear mesh frequency. Wang et al. (2017) reorganized the proposed method in Ref. [58] and advanced the method for the non-stationary operating condition by employing computed oder traking (COT) technique.

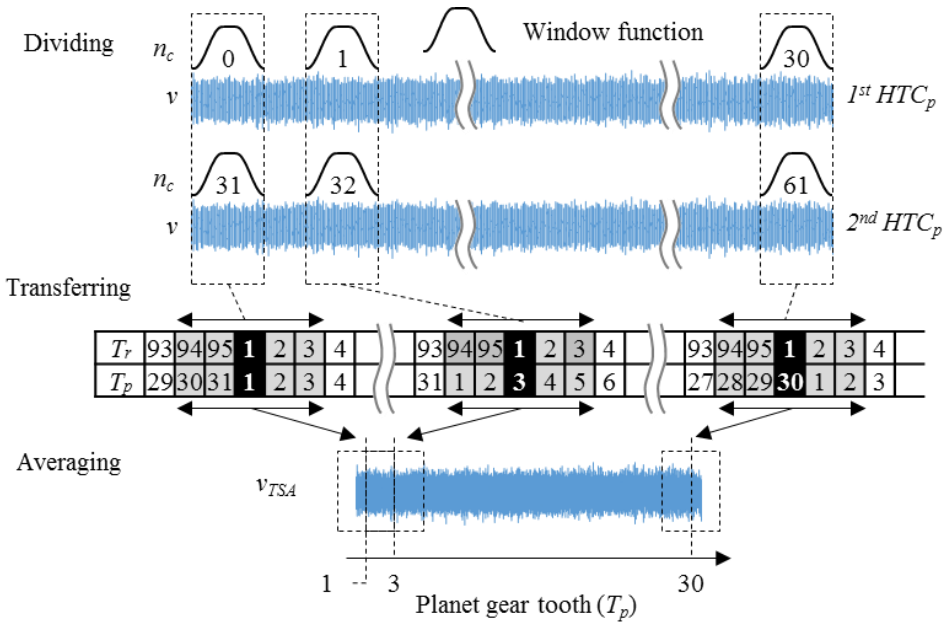

Figure 2-8 TSA for a planet gear in planetary gearbox with configuration of Z_r=95, Z_p=31 and Z_s=31

Figure 2-8 shows an illustrative example of TSA for a planet gear, where the numbers of teeth of the ring gear, planet gears, and sun gear are respectively 95, 31, and 31. TSA for the planet gear starts from dividing the signal by HTC_p. Because Z_r and Z_p are relatively prime in this case, $n_{c|\text{reset\_p}}$ is Z_p=31 carrier cycles, according to (2.14). Window functions are located with the intervals of a carrier rotational period to extract the signals at the instances that the planet gear of interest passes the sensor. In this example case, window width was set to be 5. A windowed signal (v_{win}) can be defined as:

$$v_{win} = v_{re}(\theta) \times W \tag{2.19}$$

where $v_{re}(\theta)$ is the resampled vibration signal; W is window function.

Vibration signals extracted by the window functions are transferred to the tooth domain of the planet gear using the tooth sequence (i.e., Eq. (2.12)) as shown in table of Figure 2-8. Sequential meshing teeth numbers are listed in the table, in which extraction regions defined by the window functions are indicated by shaded columns. It is noteworthy that the centers of the window functions, which are marked with black columns, are located at tooth number 1 of the ring gear (i.e., T_r=1) where the sensor is mounted. The signals in the tooth domain are ensemble-averaged by considering the tooth information. If the width of the window function is wider than one tooth-meshing period, signals with different ring-planet gear teeth pairs (e.g., (T_r, T_p) = (1, 1) pairs and (T_r, T_p) = (94, 1) pairs) can be ensemble-averaged to represent the signals from a typical planet gear tooth (e.g. T_p=1).

Signals from the sun gear are transferred to the sensor through the planet gears. Thus, although the sun gear does not directly contact the ring gear, it is necessary to examine the meshing combinations of the ring-sun gear teeth pairs. There are two ways to perform TSA for the sun gear. First, signals measured through the planet gears can be individually constructed at each set of TSA signals up to the total number of planet gears. Second, signals measured through all planet gears can be transferred to an identical tooth domain of the sun gear and ensemble-averaged to construct one set of TSA signals. It has been reported that the first method performs better than the second method [57], [60]. Basically, the overall procedures of TSA for sun gear using the first method are identical to the procedures of TSA for a planet gear excluding that the signals should be divided by HTC_s at the first step.

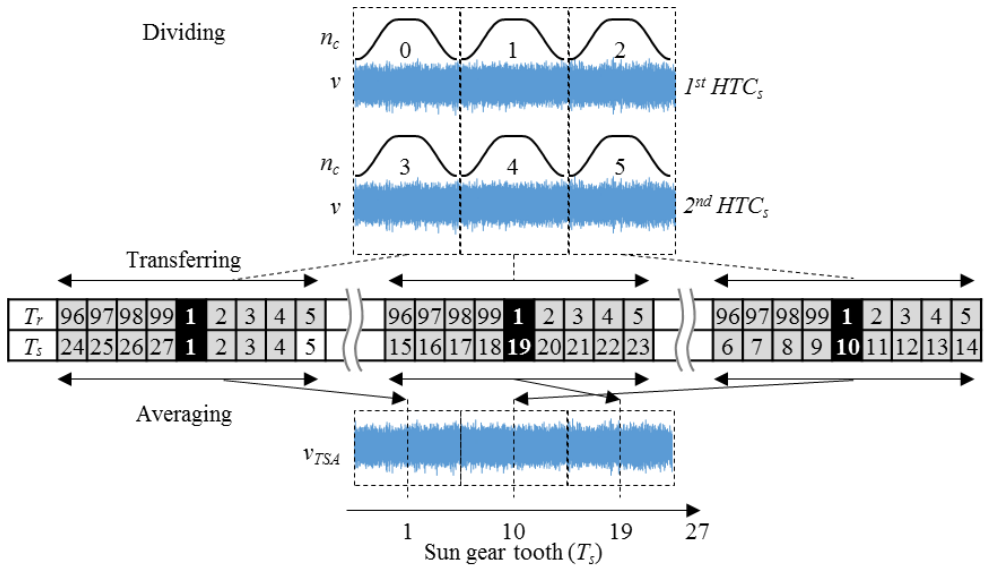

Figure 2-9 TSA for a sun gear in planetary gearbox with configuration of Z_r=99, Z_p=35 and Z_s=27

If the number of teeth of the target gear (i.e., planet gear or sun gear) and the ring gear are not relatively prime, the width of the window function should be adjusted to construct the signal from the gears. For example, TSA for a sun gear using a configuration of a gearbox adopted from Refs. [57], [60] (i.e., N_r=99, N_p=35, and N_s=27) can be considered.

Because the number of teeth of the ring gear and the sun gear are not relatively prime, $n_{c|\text{reset\_s}}$ is calculated as 3, based on Eq. (2.15). First step is to divide the vibration signal into multiple segments by HTC_s as shown in Figure 2-9. Tooth sequence ($T_s(n_c)$) of the sun gear during one HTC_s is calculated by Eq. (2.13) as 1, 19 and 10 which is indicated by black columns shown in the table in Figure 2-9. This means that signals corresponding to only three teeth of the sun gear can be captured through the planet gear that exactly passes the sensor. Thus,

in this case, the width of the window function should be at least 9 tooth-meshing periods to construct the signals for an entire rotation of the sun gear [57]. Lewicki et al. reported that the Tukey window with a width of 27 tooth-meshing periods performed best [60]. The signals extracted by the window function are transferred to the domain of the sun gear tooth, and ensemble-averaged. Because the width of the window function is quite wide, vibration modulation characteristics are complicated within the window function. Although signals only from the identical tooth of the sun gear are ensemble-averaged, the signal could be distorted during the transferring and averaging steps.

2.4 Summary and Discussion

Fault Diagnosis of a Gearbox under the Uncertain Operating Condition

A number of studies have been made to consider varying operating condition for a robust fault diagnosis of the gearbox. Despite the previous studies, fault diagnosis under the varying operating condition is challenging because the presented techniques are system-dependent. Thus, they are rarely used in real field for condition monitoring of the systems. Although an strategy to fully utilize currently available signal processing techniques across a limited range of operating (see Chapter 2.1) have been widely employed, it should be noted that to do this, the criteria for the operating conditions of interest (e.g., the criteria for the "active range" of the "WindCon" method in Figure 2-3) must be pre-defined by the users. Thus, implementations of the guidelines and options specified by IEC [28], DNV GL [30], SKF [32] and Oneprod [33] in Figure 2-1, Figure 2-2

and Figure 2-3 are not feasible unless the quantitative criteria for the operating conditions of the systems are given. To the best of my knowledge, there is no practical guideline that quantitatively classifies operating conditions of a rotating system to provide an effective range for an optimal condition monitoring strategy. Thus, it is essential to develop a general method for classification of the operating conditions of systems. In particular, stationary operating condition, which is considered to be the most valuable for fault diagnosis, should be quantitatively defined. Then, vibration signal under the intermittent stationary operating condition can be used for TSA-based fault diagnosis of the planetary gearbox without much concern about the varying operating condition.

TSA-based Fault Diagnosis of a Planetary Gearbox under the Intermittent Stationary Operating Condition

Although various kinds of narrow-range window functions has been employed to enhance the performance of TSA under the stationary operating condition, there is room for further improvement to make it directly applicable for fault diagnosis of planetary gearboxes in real field. As described above, vibration signals should be extracted as the planet gears approach the sensor to enhance the signal-to-noise ratio. However, TSA with such narrow-range window functions require extensive stationary vibration signals. In practice, it is difficult to collect the amount of data because stationary signal is rarely obtainable under the actual operating conditions of the system with operational uncertainties. This means that the range of the window functions should be

extended to fully utilize the rarely obtainable stationary vibration signals for TSA.

TSA with a full-range window function (e.g., cosine window) may serve as an alternative method because it utilizes the entire range of signals without any loss of data [64]. However, previous studies pointed out that TSA with such a full-range window function can distort the vibration signal of interest [61], [62]. Figure 2-10 illustrates an example case to explain how this undesirable distortion occurs by investigating position of the planet gears. When the planet gear of interest is positioned under the sensor (Figure 2-10 (a)), signal of interest is effectively captured by the sensor. As the planetary gearbox operates, planet gear of interest recedes from the sensor, whereas another planet gear (Planet #2) approaches the sensor (Figure 2-10 (b)). At this instance, vibration produced by Planet #2 dominates the sensory data. Full-range window function takes an entire range of sensory data into account for TSA regardless of the fact that a significant portion of sensory data are dominated by the other planet gears which are out of interest. For condition monitoring of a particular planet gear in the gearbox, vibration signals from other planet gears which are out of interest may

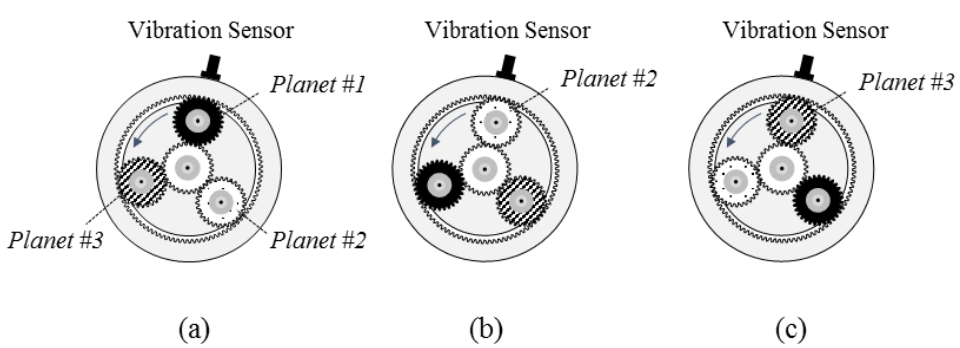

Figure 2-10 Position of gears where each planet gear is positioned under the sensor

serve as a noise. Although the full-range window function gives a small weight when the planet gear of interest is far from the sensor, it is more reasonable to exclude the signals when it is clear that the sensory data is mainly dominated by vibration from the other gears. Thus, it is imperative to design a new wider-range window that optimizes shape and range to maximize the performance of TSA while preventing distortion of the vibration signal.

Fault Diagnosis of a Planetary Gearbox under the Uncertain Vibration Modulation Characteristics

To determine the position of the window function for TSA, vibration modulation should be characterized in terms of the positions of the planet gears that determines the signal transfer path. However, vibration modulation characteristics of the gearbox is frequently unknown or unexpected. In real case, it is almost impossible to trace the position of the planet gears during the entire life of the gearbox. Even if the positions of the planet gears are exactly recorded, undesired vibration modulation characteristics can be made by various factors such as varying radial load [23], a flexible ring gear rim [19], gear manufacturing errors [20], [21], and assembly errors [22]. If the assumption about vibration modulation characteristics is not assured, faulty signals could be discarded by the abuse of the window function. To solve this challenge, D'Elia et. al. proposed to determine the optimal position of the window function for TSA by calculating power flow of the vibration signals [66]. However, optimal position of the window function cannot be exactly determined if the power flow of the signal

vary with the fluctuating operating conditions and unequal load sharing of the gears.

Another basic assumption for TSA with the window function is that the vibration signals are homogeneous within the window functions. Thus, vibration signals from different tooth meshing combinations (e.g., (T_r, T_p)=(1,1) and (2,1) where T_r and T_p denotes tooth number of the ring gear and planet gear of interest) are ensemble averaged to represent the signals from a typical tooth of the planet gear (e.g., T_p=1). However, as stated above, vibration signals are quite complex, thus may resulting in heterogeneous signal characteristics within the window function [59], [67]. To solve this challenge, Liang et al. proposed to use a narrow-range window function which has range of one tooth meshing period with smoothed edges (i.e., Tukey window) to reduce the signal distortion caused by averaging signals from different tooth meshing combinations [67]. However, it can cause data loss at the window boundaries because the Tukey window function has smoothed edges with weight lower than one.

To utilize the entire signal without the use of the window function, periodicity analysis of anomalies in time-domain can be used. In general, frequency analysis of the enveloped signal can be simply used to analyze the periodicity of anomalies that are generated based on the rotational period of the faulty gear. To advance the periodicity analysis of anomalies in spur gear system, Maczak et al. proposed ‘local meshing plane’ which visualizes periodicity of the anomalies in terms of tooth of the gears as introduced in Chapter 2.2.4 [54]. However, it requires further improvement and verification to be used for fault diagnosis of a planetary gearbox that generates modulated vibration signals. Thus, it is required

to develop a generalized methodology for fault diagnosis of a planetary gearbox that can be used even with the uncertain vibration modulation characteristics without using the conventional window function.

Chapter 3. Analytical Model and Testbed for Planetary Gearbox

3.1 Analytical Model for Planetary Gearbox

This chapter introduces an analytical model that will be used to describe the proposed method throughout the thesis. Here, we assume a gearbox configuration set to be Z_r=95, Z_p=31, Z_s=31, and N_p=3 to make it consistent with the one from the case study with the testbed described in Chapter 3.2.

3.1.1 Analytical Model for Normal Condition

An analytical model for a planetary gearbox can be designed from the sum of the vibration signals from the planet gears that are transferred to the sensor, as [68]:

$$v = \sum_{n=1}^{N_p} v_n a_n + A_{noise} r \tag{3.1}$$

where v_n is the vibration signals generated from n^{th} planet gear; a_n is the signal transfer function that represents the relative distance from the n^{th} planet gear to the sensor; A_{noise} is noise factor, r is non-coherent random noise to emulate many noise sources including measurement error, environmental noise, etc.

Figure 2-10 represents the instances that each planet gear is positioned under the sensor while having minimum signal transfer function to the sensor As the

planet gears rotate in a counter-clockwise manner, three planet gears indicated as "Planet #1," "Planet #2," and "Planet #3" sequentially pass the sensor. Although the three planet gears produce the same amount of vibration energy, the relative distance of each planet gear from a sensor affects the intensity of the signal measured by the sensor. The transfer factor of the n^{th} planet gear (a_n), thus, was designed and multiplied to the vibration produced by the n^{th} planet gear. When the planet gear approaches the sensor, the transfer factor gives greater weight. One the other hand, less weight [69], [70] or zero weight [71]–[73] are assigned when the planet gear recedes from the sensor.

Planet gears in a gearbox theoretically produce the same amount of vibration energy (v_p) with slight meshing phase difference when simultaneously meshing with a ring gear. Therefore, the vibration signals from one planet gear (v_p) before applying the signal transfer function are defined as [68]:

$$v_n(t) = \cos\left(Z_r w_c t + Z_r \psi_n\right) \tag{3.2}$$

where Z_r is the number of teeth on the ring gear; w_c is rotational speed of the carrier; ψ_n is position of the n^{th} planet gear in angle.

Vibration signals from the planet gears with the effect of the signal transfer functions are represented in Figure 3-1 (a)-(c) where it is assumed that the sensor is mounted around tooth number 17 of the ring gear. The signal transfer function of planet gear #*n* (i.e., a_n in Eq. (3.1)) has maximum amplitude when the planet gear #*n* passes the sensor, and decreases as the gear recedes from the sensor. For illustration, the analytical model was designed to have zero weight when the planet gear recedes from the sensor in this case. As a result, combined vibration

signal, which is defined by Eq. (3.1), is modulated as shown in Figure 3-1 (d).

3.1.2 Examining Faults for the Analytical Model

Anomaly from faulty tooth of the planet gear and the sun gear can be simulated as an additional half-period sine wave during the mesh of the faulty tooth [65]. To represent the signal transfer characteristics to the sensor, anomalies from faulty tooth of the planet gear and the sun gear are multiplied by the signal transfer function which is denoted as a_n in Eq. (3.1).

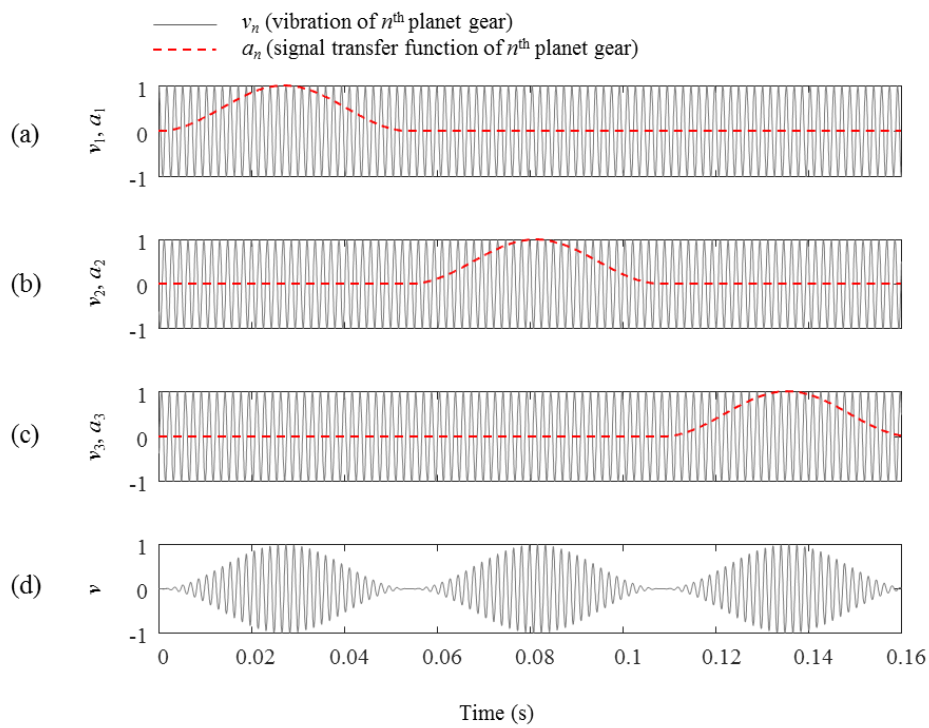

Figure 3-1 Analytical model of planetary gearbox: (a) Planet # 1, (b) Planet # 2, (c) Planet # 3, and (d) combined signal.

Figure 3-2 represents an illustrative example of signals from faulty tooth of the planet gear and the sun gear for one carrier rotation of the gearbox. Maximum amplitude of the anomalies from the faulty tooth was set to be 1 for the illustration. Raw vibration generated from the planet gears and the corresponding signal transfer functions are represented as high-frequency sinusoidal signals and a half-period dotted sinusoidal signals respectively. Meshing instances of the faulty tooth and the corresponding anomalies transferred to the sensor are

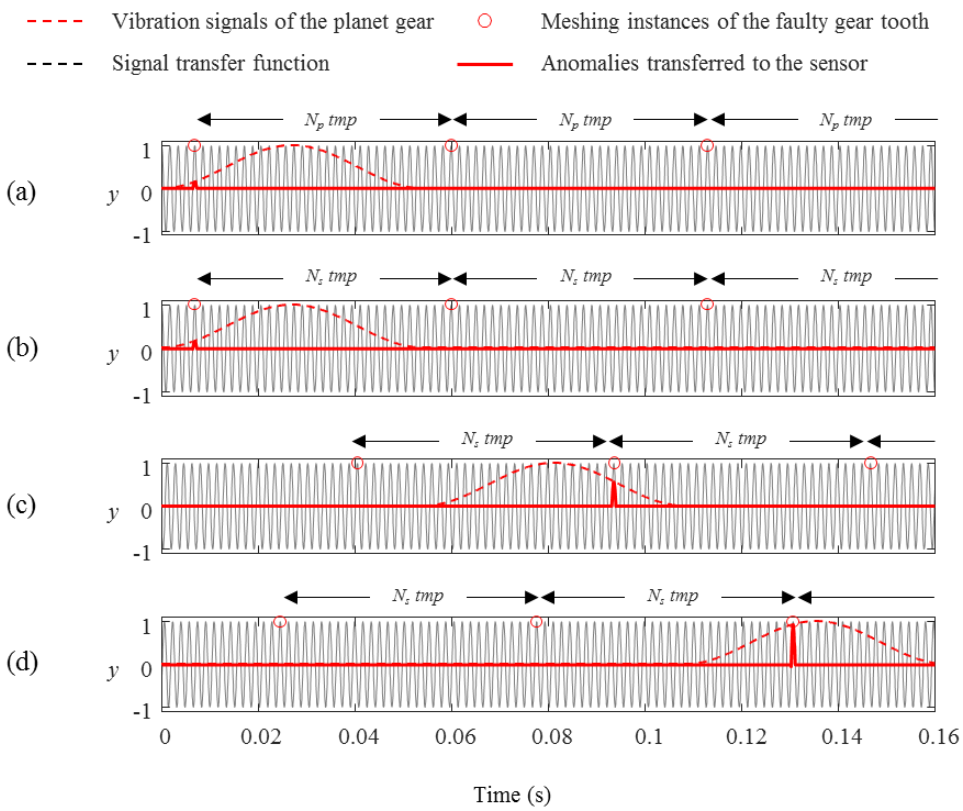

Figure 3-2 Simulation of faulty condition of the analytical model: (a) Fault of a planet gear, (b) Fault of a sun gear meshing with planet # 1, (c) Fault of a sun gear meshing with planet # 2, (d) Fault of a sun gear meshing with planet # 3

represented by red circles at the top of the plots and red thick lines respectively.

In this thesis, tooth number 5 of the first planet gear (T_p=5), or tooth number 5 of the sun gear (T_s=5) is designed to have a fault. Because the faulty tooth of the planet gear meshes with the ring gear at every rotation of the gear, meshing instances is at the intervals of Z_p tooth meshing period (*tmp*) as shown in Figure 3-2 (a). On the other hand, faulty tooth of the sun gear meshes with the multiple planet gears. For example, if the sun gear rotates in counter clock-wise as shown in Figure 2-6 and Figure 2-10, faulty tooth of the sun gear sequentially meshes with the Planet #1, #3 and #2. This phenomenon is also considered to generate the signals from faulty tooth of the sun gear. Meshing instances of the faulty tooth of the sun gear are sequentially made by planet gear #1 (Figure 3-2 (b)), #3 (Figure 3-2 (d)) and #2 (Figure 3-2 (c)).

3.2 Testbed for Planetary Gearbox

A 2kW testbed was designed to emulate planetary gearboxes as shown in Figure 3-3. The testbed is comprised of two servo motors, a main bearing, a flywheel, gearboxes, and a measurement system with eight vibration sensors. Two servo motors at each side of the testbed are respectively controlled by speed and torque to simulate a typical industrial gearbox that operates with a controllable speed and external load. Vibration data was acquired by the vibration sensor attached on the top of the planetary gearbox at 25.6 kHz of sampling rate.

Detailed view of the target gearbox is shown in Figure 3-4. The target gearbox

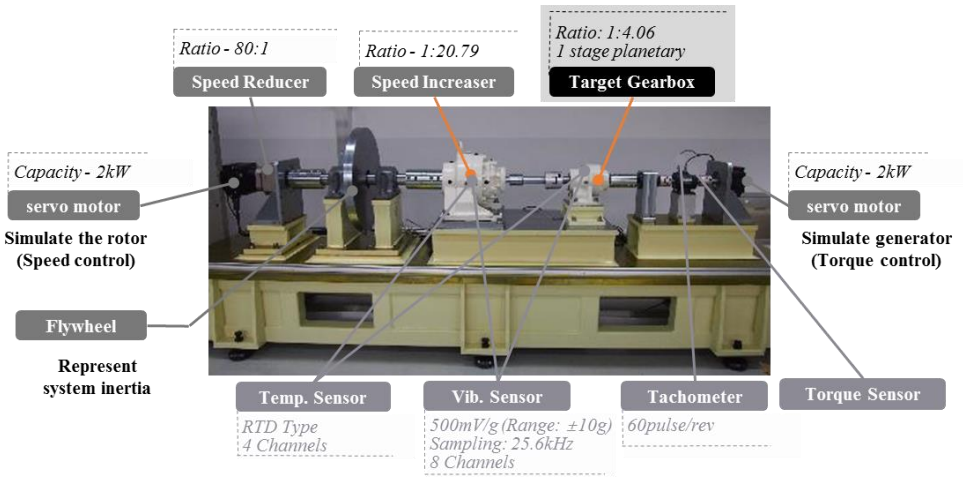

Figure 3-3 Testbed for planetary gearbox

has a ring gear with 95 teeth, a sun gear with 31 teeth and three planet gears with 31 teeth. At every test, the housing of the planetary gearbox was disassembled and every location of contact points of inner gears were reset to the identical initial condition as shown in Figure 3-4 (b). During the tests, position of the planet gears could be exactly tracked by using encoder. To simulate the faulty condition of the gearbox, partial tooth breakage and line-type defect are manufactured on the surface of the planet gear and the sun gear as shown in Figure 3-5.

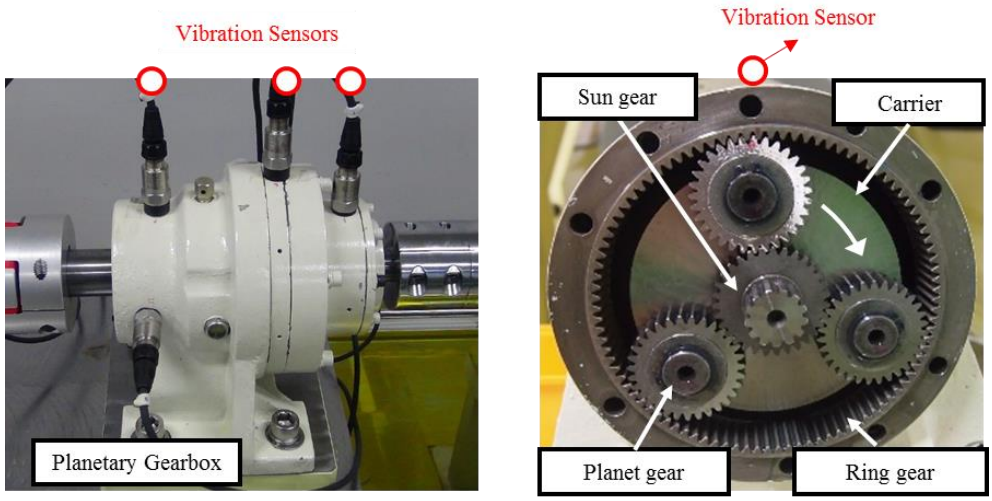

Figure 3-4 Target planetary gearbox: (a) overview of the gearbox and (b) inner side of the gearbox

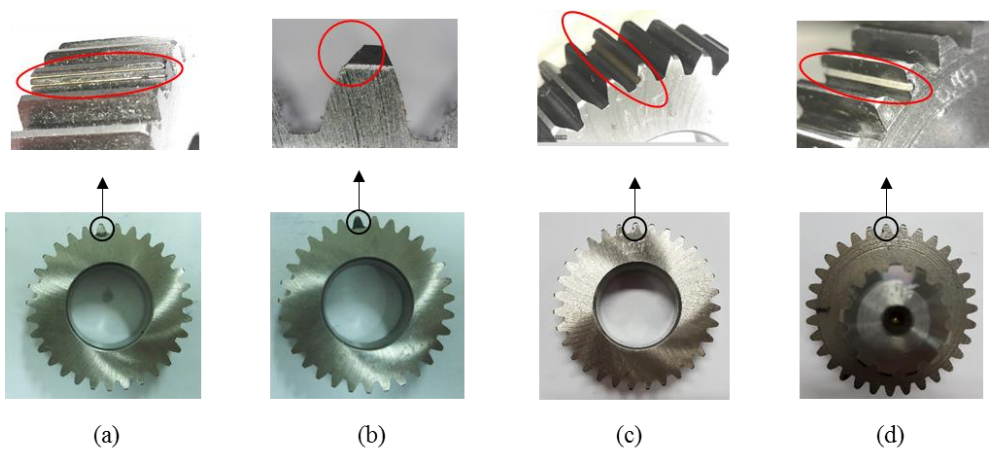

Figure 3-5 Fault of the gears: (a) fault of a planet gear with two thin lines, (b) partial tooth breakage of a planet, (c) line-type fault of a planet gear and (d) line-type fault of a sun gear

Chapter 4. Quantitative Definition of the Stationary Operating Condition

This chapter proposes a general method for classification of the operating conditions of systems in terms of rotational speed and power. In particular, to produce the most valuable vibration signal for condition monitoring of a gearbox, quantitative criteria for the stationary operating condition are defined, while considering inherent randomness in the performance of the system. The ultimate goal is to use these classifications to establish an optimal strategy for condition monitoring of the system. Among various engineering systems equipped with the gearbox, wind turbine (WT) is the most representative application for this purpose due to the uncertain nature of wind profiles. Thus, in this thesis, classification of operational condition of WT is presented as a representative study. This concept can be extended to other kinds of applications with a minor revision.

Chapter 4.1 introduces an analytical WT model that calculates the relationship between input wind speed and power or rotor speed based on a generic control logic for variable-speed WTs. In Chapter 4.2, the probability density functions (PDFs) of power and rotor speed are mathematically derived from the analytical WT model to provide a theoretical rationale for the classification method and the criteria for the operating conditions. In Chapter 4.3, five distinct classes are developed in such a way that WTs in a particular class have unique operating characteristics, thus leading to homogeneous condition monitoring signals in

each class. In particular, to produce the most valuable vibration signal for condition monitoring of WTs, quantitative criteria for the stationary operating condition of WTs are defined, while considering inherent randomness in the performance of WTs. Chapter 4.4 presents two case studies: (1) a WT model with various levels of average wind speed and (2) an actual 2.5 MW wind turbine in the field. Chapter 4.5 discusses the applicability of the proposed classification-based condition monitoring strategy to the industry and presents condition monitoring results for a 2 kW gearbox testbed under various operating conditions.

4.1 Analytical Modeling of Wind Turbine (WT) Performance

Different control logic strategies are implemented to achieve optimal performance in variable-speed wind turbines (WTs) [74]. As illustrated in Figure 4-1, in Region 1, the wind speed is less than the "cut-in" wind speed ($v_{cut\text{-}in}$). In this region, the wind energy is considered to be insufficient to produce power. Consequently, the WT is directed not to generate power, and instead stays in an idle mode. When the wind speed exceeds the cut-in wind speed, the rotor starts to rotate at the cut-in rotor speed ($w_{cut\text{-}in}$). In Region 2, the output power of the WT can be characterized as being proportional to the cube of the wind speed [75]. The rotor speed is controlled to maximize the efficiency of the WT's energy production in such a way that the rotor speed can be approximated as being linearly proportional to the wind speed [76]. When the wind speed becomes high enough to generate the rated power (P_{rated}) and the rated rotor speed (w_{rated}) of the

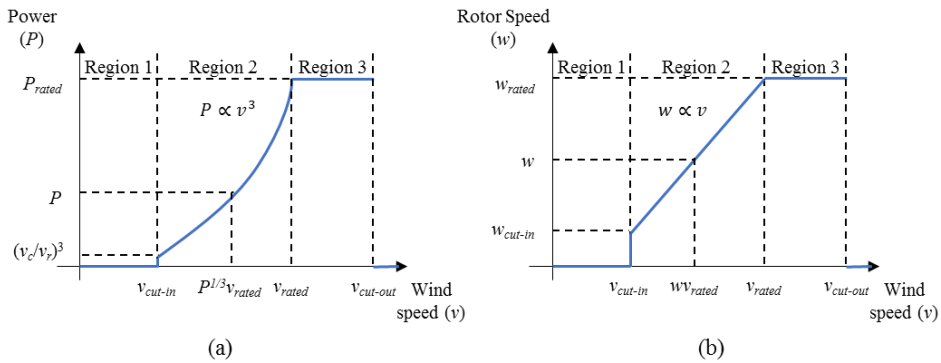

Figure 4-1 Region of wind speed for control of wind turbines: (a) wind speed-power relationship and (b) wind speed-rotor speed relationship

WT, the blade pitch is controlled to maintain the power and rotor speed at constant levels (Region 3). Based on the WT control logic outlined here, the relationship between the wind speed (v) and normalized power (P), or normalized rotor speed (w), can be represented as:

$$P = \begin{cases} 0 & v < v_{cut-in} \\ \left(v / v_{rated}\right)^3 & v_{cut-in} \le v < v_{rated} \\ 1 & v_{rated} \le v \end{cases} \tag{4.1}$$

$$w = \begin{cases} 0 & v < v_{cut-in} \\ v / v_{rated} & v_{cut-in} \le v < v_{rated} \\ 1 & v_{rated} \le v \end{cases} \tag{4.2}$$

On the other hand, it has been reported that any engineered system including wind turbines has considerable uncertainties due to several issues, such as randomness in geometry, material property and loading (e.g., stochastic nature of the wind property) [77], [78]. Based on the work of Tondan and Zhigang, power

and rotor speed with random noise can be defined by incorporating Gaussian noise as [79]:

$$P_n = P + \varepsilon_P \tag{4.3}$$

$$w_n = w + \varepsilon_w \tag{4.4}$$

where ε_p and ε_w represent the Gaussian noise with a mean of zero and a standard deviation of σ (i.e., $\varepsilon_p \sim N(0, \sigma_P^2)$, and $\varepsilon_w \sim N(0, \sigma_w^2)$).

To calculate the power and rotor speed using the WT model, wind speed (v) must be known. Prior research recommends that wind distribution should be assumed to follow a Rayleigh distribution whose CDF (F_v) and PDF (f_v) can be defined as [80], [81]:

$$F_v\left(v;\bar{v}\right) = 1 - e^{-\frac{\pi}{4}\left(\frac{v}{\bar{v}}\right)^2},\ v \geq 0 \tag{4.5}$$

$$f_v\left(v;\bar{v}\right) = \frac{\pi}{2}\frac{v}{\left(\bar{v}\right)^2} e^{-\frac{\pi}{4}\left(\frac{v}{\bar{v}}\right)^2},\ v \geq 0 \tag{4.6}$$

where $\bar{v}$ stands for average wind speed. The IEC 61400-1 certification provides three representative average wind speeds (i.e., $\bar{v}$=7.5, 8.5, and 10 m/s) that should be considered for Eqs. (4.5) and (4.6) to explain the general behavior of wind at different sites [82]. Rayleigh distributions with average wind speeds of 7.5 m/s, 8.5 m/s, and 10 m/s are compared in Figure 4-2.

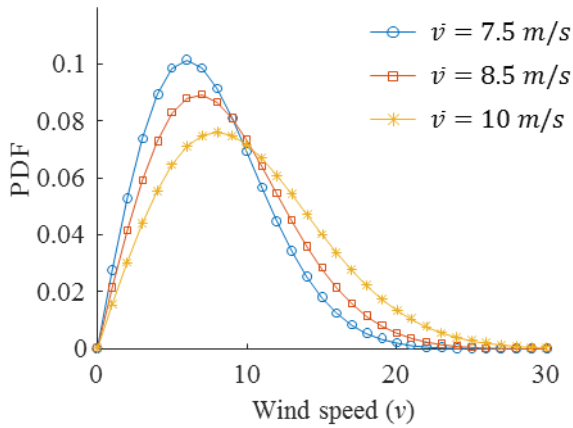

Figure 4-2 The probability density functions (PDFs) of wind speeds modeled by Rayleigh distribution with the average wind speeds of 7.5 m/s, 8.5 m/s, and 10 m/s.

4.2 Mathematical Derivation of the PDF of Power and Rotor Speed

This chapter proposes a two-step procedure to derive the statistical description (i.e., PDF) of WT performance in terms of power and rotor speed. This procedure consists of (1) a uncertainty propagation technique to consider propagation of uncertainty in wind speed and (2) convolution of two main sources of the randomness, such as uncertain system performance and Gaussian noise. Detailed procedures for determining the PDFs of the power and the rotor speed are provided in Chapter 4.2.1 and 4.2.2, respectively.

4.2.1 The *PDF* of Power

In this work, a random variable transformation technique was employed to show the PDF of power in terms of the PDF of wind speed. Mathematically, when y (e.g., power) is a function of a random variable x (e.g., wind speed) with a relationship of $y=g(x)$, the uncertainty of x is propagated to the one of y, formulating a cumulative distribution function (CDF), (F_Y) as [83]:

$$F_Y\left(y\right)=P\left(Y\le y\right)=P\left(g\left(x\right)\le y\right)=P\left(X\in B_y\right), \tag{4.7}$$

where

$$B_y=\left\{x\in \mathrm{IR}:g\left(x\right)\le y\right\} \tag{4.8}$$

Using the random variable transformation technique, the CDF of the power from Eq. (4.1) becomes:

$$F_P\left(P\right)=\begin{cases} 0 & P<0 \\ \mathrm{P}\left(v\le v_{cut-in}\right)=1-e^{-\frac{\pi}{4}\left(\frac{v_{cut-in}}{\bar{v}}\right)^2} & 0\le P<\left(v_{cut-in}/v_{rated}\right)^3 \\ \mathrm{P}\left(v\le P^{1/3}v_{rated}\right)=1-e^{-\frac{\pi}{4}\left(\frac{P^{1/3}v_{rated}}{\bar{v}}\right)^2} & \left(v_{cut-in}/v_{rated}\right)^3\le P<1 \\ 1 & 1\le P \end{cases} \tag{4.9}$$

In (4.9), jump discontinuities exist for C_0 (when P=0) and C_1 (when P =1):

$$C_0=F_P\left(0\right)-\lim_{P\to 0^-}F_P\left(P\right)=1-e^{-\frac{\pi}{4}\left(\frac{v_{cut-in}}{\bar{v}}\right)^2} \tag{4.10}$$

$$C_1 = F_P(1) - \lim_{P \to 1^-} F_P(P) = 1 - \left(1 - e^{-\frac{\pi}{4}\left(\frac{v_{rated}}{\bar{v}}\right)^2} \right) = e^{-\frac{\pi}{4}\left(\frac{v_{rated}}{\bar{v}}\right)^2} \tag{4.11}$$

The differentiation of (4.9) with respect to *P* becomes:

$$\tilde{f}_P(P) = \begin{cases} \frac{\pi}{6}\left(\frac{v_{rated}}{\bar{v}}\right)^2 P^{-1/3} e^{-\frac{\pi}{4}\left(\frac{P^{1/3} v_{rated}}{\bar{v}}\right)^2} & \left(v_{cut-in} / v_{rated}\right)^3 < P < 1 \\ 0 & \text{otherwise} \end{cases} \tag{4.12}$$

The PDF of the power (f_P) is obtained by combining Eq. (4.12) with Eqs. (4.10) and (4.11):

$$f_P(P) = C_0 \delta(P) + C_1 \delta(P-1) + \tilde{f}_P(P) \tag{4.13}$$

Next, the Gaussian noise term (ε_P) is added to Eq. (4.13) to incorporate the effect of the inherent randomness in wind turbines. The PDF of a sum of two random variables is calculated by convolution [83]. The PDF of the power with the noise term is presented as:

$$\begin{aligned} f_{Pn}(P) &= \left(f_P * \varepsilon_P\right)(P) = \int_{-\infty}^{\infty} f_P(y) \times \varepsilon_P(P-y)\, dy \\ &= \int_{-\infty}^{\infty} f_P(y) \times \frac{1}{\sigma_P \sqrt{2\pi}} e^{-\frac{(P-y)^2}{2\sigma_P^2}} dy \\ &= \frac{C_0}{\sigma_P \sqrt{2\pi}} e^{-\frac{P^2}{2\sigma_P^2}} + \frac{C_1}{\sigma_P \sqrt{2\pi}} e^{-\frac{(P-1)^2}{2\sigma_P^2}} + \tilde{f}_{Pn}(P), \end{aligned} \tag{4.14}$$

where $\tilde{f}_{Pn}(P)$ is calculated through the following equation:

$$\begin{aligned}\tilde{f}_{Pn}(P) &= \int_{-\infty}^{\infty} \tilde{f}_P(y) \times \frac{1}{\sigma_P\sqrt{2\pi}} e^{-\frac{(P-y)^2}{2\sigma_P^2}} dy \\ &= \int_{(v_{cut-in}/v_{rated})^3}^{1} \frac{\pi}{6}\left(\frac{v_{rated}}{\bar{v}}\right)^2 y^{-1/3} e^{-\frac{\pi}{4}\left(\frac{y^{1/3}v_{rated}}{\bar{v}}\right)^2} \times \frac{1}{\sigma_P\sqrt{2\pi}} e^{-\frac{(P-y)^2}{2\sigma_P^2}} dy\end{aligned} \quad (4.15)$$

In Eq. (4.14), the PDF was defined as the sum of three terms. The first two terms were derived from the impulse function with the magnitudes of C_0 and C_1 near zero and the rated power, respectively. The power in the mid-range is dominated by the third term in Eq. (4.14), which cannot be calculated analytically. Several numerical integration methods can be used, such as the Trapezoidal rule and adaptive Gauss-Kronrod quadrature [20]. Figure 4-3 (a) and (b) respectively show the CDF and PDF of the power where the noise term is not considered. It is noteworthy that C_0 and C_1, which are generated from the idle and pitch control mode of the wind turbine, are represented as discontinuities of the CDF (C_0 and C_1) in Figure 4-3 (a) and as impulse functions with magnitude of C_0 and C_1 in Figure 4-3 (b). The PDF of the power subjected to uncertainties is shown in Figure 4-3 (c). The standard deviation of the Gaussian noise was set to be 2.5 percent of the rated operating condition (i.e., σ_P=0.025) for the study [85]. The discontinuities were reconstructed as clusters around zero and rated power, as shown in Figure 4-3 (c).

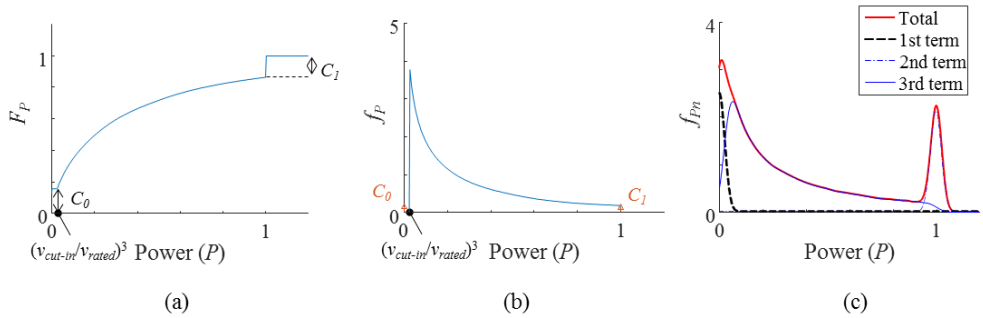

Figure 4-3 The CDF and PDF of power: (a) the CDF of power, (b) the PDF of power and (c) the PDF of power with uncertainties.

4.2.2 The *PDF* of Rotor Speed

Identical procedures were used in our study to define the PDF of rotor speed. Using the random variable transformation technique, the CDF of the rotor speed becomes:

$$F_w(w)=\begin{cases} 0 & w<0 \\ \mathrm{P}\left(v\le v_{cut-in}\right)=1-e^{-\frac{\pi}{4}\left(\frac{v_{cut-in}}{\bar{v}}\right)^2} & 0\le w<v_{cut-in}/v_{rated} \\ \mathrm{P}\left(v\le wv_{rated}\right)=1-e^{-\frac{\pi}{4}\left(\frac{wv_{rated}}{\bar{v}}\right)^2} & v_{cut-in}/v_{rated}\le w<1 \\ 1 & 1\le w \end{cases} \tag{4.16}$$

The PDF of the rotor speed (f_w) is presented as:

$$f_w(w)=C_0\delta(w)+C_1\delta(w-1)+\tilde{f}_w(w) \tag{4.17}$$

where C_0 at w=0 and C_1 at w=1 are as defined in Eqs. (4.10) and(4.11). The

third term is obtained by differentiating F_w with respect to w.

$$\tilde{f}_w(w) = \begin{cases} \frac{\pi}{2}\left(\frac{v_{rated}}{\bar{v}}\right)^2 w e^{-\frac{\pi}{4}\left(\frac{wv_{rated}}{\bar{v}}\right)^2} & v_{cut-in}/v_{rated} < w < 1 \\ 0 & \text{otherwise} \end{cases} \quad (4.18)$$

The PDF of the rotor speed with uncertainties then becomes:

$$f_{wn}(w) = (f_w * \varepsilon_w)(w) = \frac{C_0}{\sigma_w\sqrt{2\pi}} e^{-\frac{w^2}{2\sigma_w^2}} + \frac{C_1}{\sigma_w\sqrt{2\pi}} e^{-\frac{(w-1)^2}{2\sigma_w^2}} + \tilde{f}_{wn}(w) \quad (4.19)$$

where $\tilde{f}_{wn}(w)$ is calculated using the following equation.

$$\tilde{f}_{wn}(w) = \int_{v_{cut-in}/v_{rated}}^{1} \frac{\pi}{2}\left(\frac{v_{rated}}{\bar{v}}\right)^2 y e^{-\frac{\pi}{4}\left(\frac{yv_{rated}}{\bar{v}}\right)^2} \times \frac{1}{\sigma_w\sqrt{2\pi}} e^{-\frac{(w-y)^2}{2\sigma_w^2}} dy \quad (4.20)$$

The CDF and PDF of the rotor speed, and the PDF of the rotor speed with uncertainties are shown in Figure 4-4 (a)-(c).

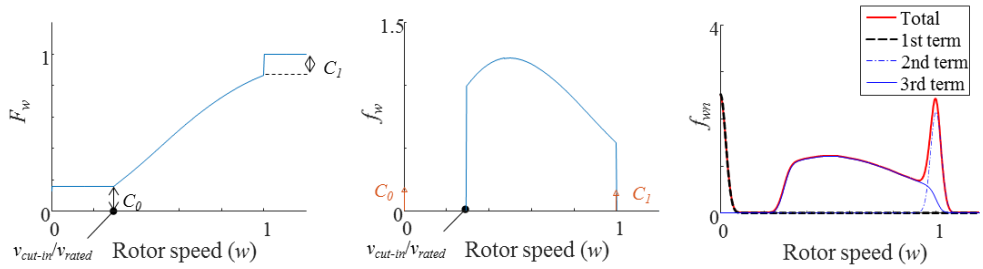

Figure 4-4 The CDF and PDF of rotor speed: (a) the CDF of rotor speed, (b) the PDF of rotor speed and (c) the PDF of rotor speed with uncertainties

4.3 Classification of the Operating Conditions of a WT

This chapter proposes a method for classification of WT operating conditions. Then, quantitative criteria for the stationary operating condition are defined by using the properties of distribution of power and rotor speed, which were outlined in Chapter 3. Empirical PDF and Gaussian mixture model (GMM) techniques are employed to enable practical use of the proposed method in the field where exact PDF equations are not provided.

4.3.1 A Classification Method for Operating Conditions of a WT

As illustrated in Figure 4-5, the proposed methods aim to classify the operating conditions of WTs into five classes in terms of the rotor speed and the output power. Boundaries between the stationary and non-stationary operating conditions for power and rotor speed are represented as C_p and C_w, respectively.

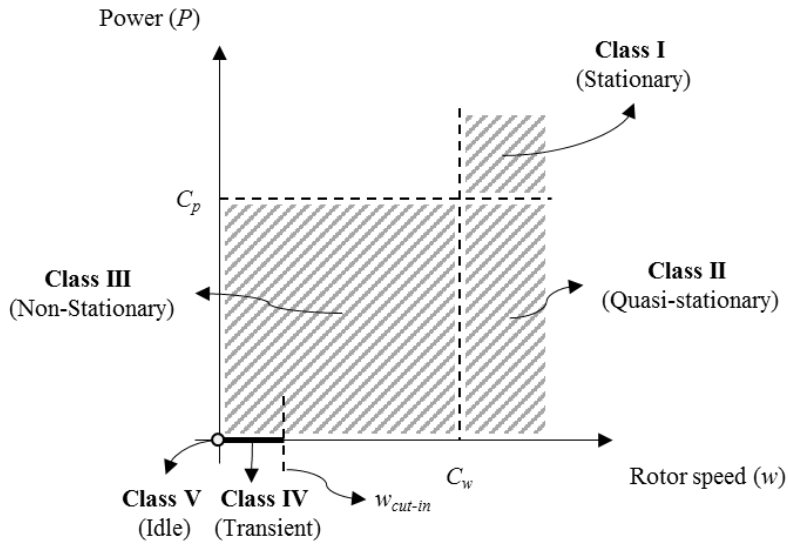

Figure 4-5 The proposed classification rule for operating conditions of a wind turbine.

When both the power and the rotor speed are greater than C_p and C_w simultaneously, the data collected for this operating regime is assigned to Class I. In this class, power and rotor speed should remain nominally constant at their rated values due to the pitch control of the WT. For this class, cost-effective signal processing techniques, such as fast Fourier transform and order analysis can serve as efficient tools for condition monitoring of the WT, since the monitoring signal is stationary and homogeneous. In Class II, WTs operate in a quasi-stationary operating condition with varying power production, despite the nominally constant rotor speed. This scenario can occur due to rapidly varying wind properties or through pitch and yaw error in the WT [81]. In this case, the energy contained in the measured condition monitoring signal can be dependent to the varying power profile [10], [13]. Next, non-stationary operating conditions

of WTs were defined as Class III where both the rotor speed and the power were significantly varying below C_p and C_w. In this case, the condition monitoring signal requires an advanced signal processing technique applicable to the varying operating conditions. The operating conditions of WTs in idle mode were defined as Class V, where the rotor speed and power are zero. Class IV is assigned for transient operating conditions between Class III and Class V, where rotor speed varies below the cut-in rotor speed, and power is zero. In Class IV and Class V, the condition monitoring signal is not likely to include meaningful information with respect to condition monitoring of the WTs. Figure 4-6 shows an illustrative example of the operating conditions of a WT for each class, where C_p and C_w were set to be equal for simplified representation.

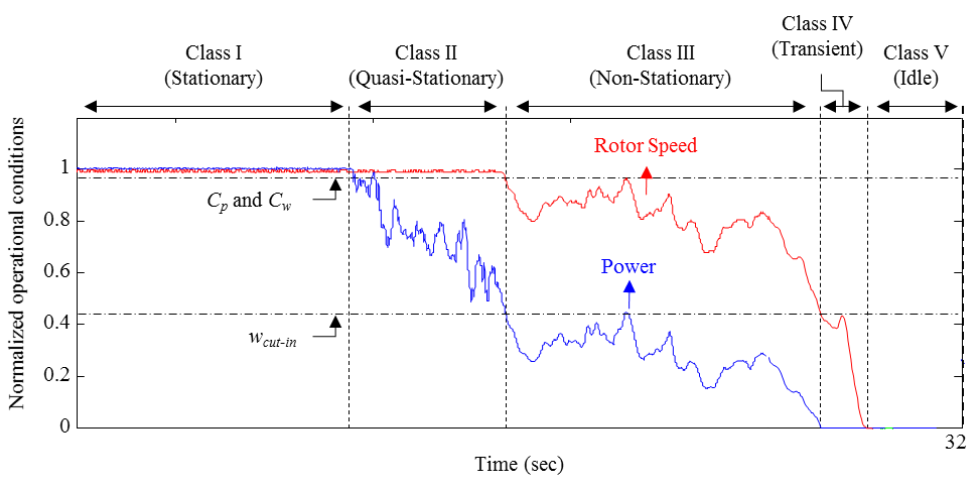

Figure 4-6 Sample results of the proposed method for classification of operating conditions of a wind turbine.

4.3.2 Definition of Quantitative Classification Criteria

This chapter defines quantitative criteria that define boundaries between stationary and non-stationary operating conditions of WTs (i.e., C_p and C_w). These boundaries are required for accurate classification. As shown in Figure 4-3 (c) and Figure 4-4 (c), clusters are formed around the rated operating condition due to the pitch control used by WTs when there is enough wind speed to warrant such control. The boundaries between the stationary and non-stationary operating conditions of WTs (i.e., C_p and C_w) can be defined as values that separate the clusters formed around the rated power and rotor speed. This chapter proposes two methods to define the appropriate values of C_p and C_w that satisfy the following conditions: (1) C_p and C_w should be small enough to obtain as much data as possible in Class I, and (2) C_p and C_w should not be excessively small such that they guarantee stationary operating conditions in Class I.

Method 1: Identification of minimum probability density using an Empirical PDF

Boundaries between stationary and non-stationary operating conditions can be defined based on the properties of the distribution of power and rotor speed. As the power (P) and the rotor speed (w) approach to the rated values, their probability densities (i.e., f_p and f_w) decrease where the noise term is not incorporated as shown in Figure 4-3 (b) and Figure 4-4 (b). When the PDFs of the power and the rotor speed incorporate inherent randomness, clusters are formed around the rated values by convolution of the noise term and the impulse

function with the magnitude of C_1, eventually increasing probability densities (See "Total" lines in Figure 4-3 (c) and Figure 4-4 (c)). As a result, the PDFs of power and rotor speed should have a concave form around the rated operating condition. Theoretical boundaries between stationary and non-stationary operating conditions can be defined as the point where the PDFs of power and rotor speed are minimized around the rated operating condition. Although it seems to be straightforward to find the minimum of the PDF around the rated operating condition, it is challenging to do this in field settings where the exact equations for the PDFs of power and rotor speed are not given. To solve this challenge, this study employed an empirical PDF. The empirical PDF is a data-oriented empirical measure of the probability distribution of a random variable, which is widely used in real field because of easy implementation and a general convergence property as a non-parametric density estimator [86]. The empirical PDF can be derived by numerical differentiation of an empirical CDF as:

$$f(x) = \frac{F(x+\Delta x) - F(x)}{\Delta x} \tag{4.21}$$

where $F(x)$ and x represent the empirical CDF and WT performance, respectively; Δx is the difference between two adjacent values. The empirical CDF ($F(x)$) can be defined as [87]:

$$F(x) = \frac{1}{N_s} \sum_{i=1}^{N_s} 1\{x_i \le x\} \tag{4.22}$$

where N_s is the number of samples; x_i is the measured WT performance at the i^{th} sample point (i=1, ···, N_s); $1\{A\}$ is the indicator function that computes one only

if the logic *A* is satisfied.

Figure 4-7 represents the relative histogram and the empirical PDFs for power and rotor speed around the rated operating condition that were calculated from the analytical WT model with an average wind speed of 7.5 m/s. The sampling rate was assumed to be one sample per second, and one-year of data was used. From the figure, it can be seen that C_p and C_w could be quantitatively defined by employing the empirical PDF.

Empirical PDFs, non-parametric density estimator, have been widely used in actual applications due to easy implementation and low computational cost compared to other density estimators. Theoretically, with the infinite number of data points, an empirical PDF will converge to the PDF of a population while

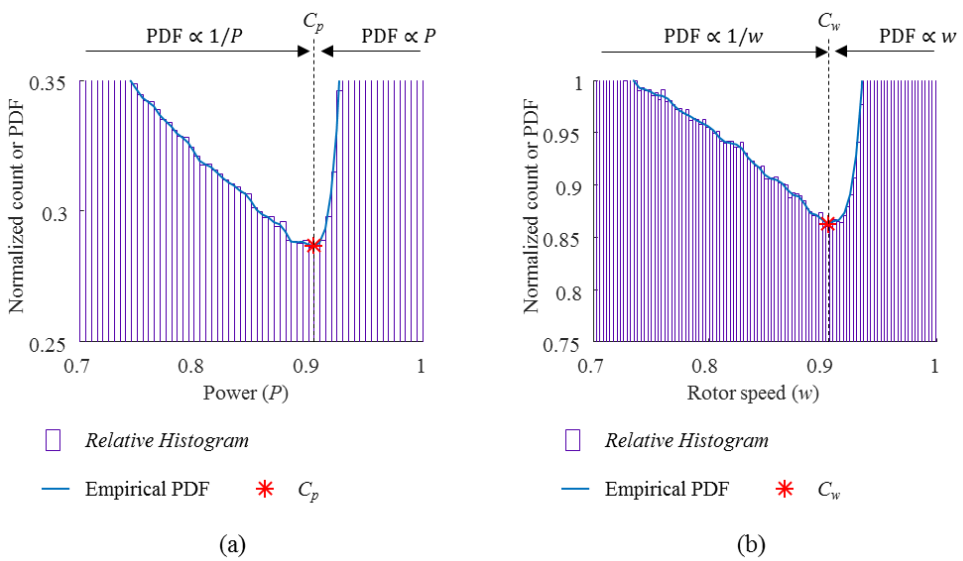

Figure 4-7 The probability density function (PDF) for the operating conditions of the WT model around the rated condition where an average wind speed of 7.5 m/s was used: (a) power and (b) rotor speed.

having a general property as a density estimator [86]. In reality, it is infeasible to collect the infinite number of data points. Thus, a general guideline should be given to define the appropriate number of data points for Method 1. The issue was addressed in several studies [88]. As an example, the ASME international standard suggests that the minimum number of data points should be calculated by [89]:

$$n = \left(\frac{3\sigma_o}{E} \right)^2 \tag{4.23}$$

where σ_o is the estimate of the standard deviation of the population; E is the maximum acceptable difference between the true mean and the sample mean. When σ_o is assumed to be 0.025 (difference between σ_p and σ_w in Eqs. (4.14) and (4.19)) and E is set to be 1 percent of the operating condition for an accurate estimation, the minimum number of data points required for Method 1 is 56.25. This amount of data corresponds to about 0.4 days of WT operation if a single data point is collected every 10 minutes [90].

Most of the guidelines for the determination of the appropriate number of data points including Eq. (4.23) assume that the probability distribution of the population follows a single-modal Gaussian distribution. However, the probability distribution of the operating data of WTs generally follows a multi-modal Gaussian distribution. As shown in Chapter 4.4, at least, five Gaussian distributions were needed for a proper fitting of the probability distribution of the WT operating data. Consequently, the empirical PDFs require much longer period of time (e.g., 4 days = 0.4 days × 10 safety factor).

Method 2: Deconvolution of stationary data using a Gaussian mixture model (GMM)

Criteria for the stationary operating condition of power and rotor speed (C_p and C_w) can be defined based on statistical moments (e.g., mean and standard deviation) of the clusters around the rated operating conditions of the WTs. A statistical moment of the clusters can be approximated by using a Gaussian mixture model (GMM) as it is widely used to fit multi-modal distributions [91]. A GMM can be expressed as a combination of multiple Gaussian distributions:

$$f\left(x;\theta\right)=\sum_{k=1}^{K} w_k N\left(x;\mu_k,\sigma_k\right) \tag{4.24}$$

where K is the number of Gaussian distributions used to fit the given distribution; w_k is the weight of the k^{th} Gaussian distribution; $N(x;\ \mu_k,\ \sigma_k)$ is the k^{th} Gaussian distribution with the mean of μ_k and the standard deviation of σ_k,. The PDF of a Gaussian distribution with the mean of μ_k and the standard deviation of σ_k is defined as:

$$N\left(x;\mu_k,\sigma_k\right)=\frac{1}{\sigma_k\sqrt{2\pi}}e^{-\frac{(x-\mu_k)^2}{2\sigma_k^2}} \tag{4.25}$$

This study estimated the optimal Gaussian mixture parameters (i.e., w_k, μ_k, and σ_k, where i=1, …, K) to achieve the maximum likelihood function by employing an expectation and maximization (EM) algorithm, as is commonly used for the GMM [92]. Figure 4-8 represents an example of the power and rotor

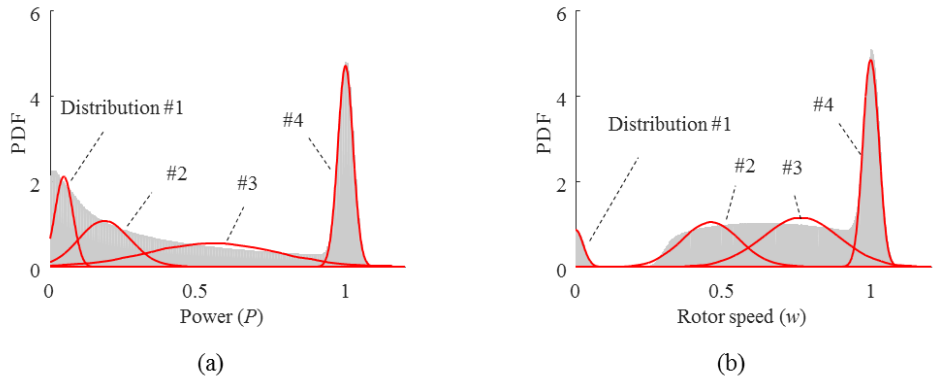

Figure 4-8 The probability density function (PDF) for operating conditions using a WT model fitted by a Gaussian mixture model with four Gaussian distributions where average wind speed of 7.5 m/s was used: (a) power and (b) rotor speed.

speed of the analytical WT model fitted using the GMM with four Gaussian distributions (i.e., K=4). It can be seen that the clusters located around the rated power and rotor speed were appropriately fitted by the last Gaussian distribution of the GMM. This is marked as '#4' in Figure 4-8.

The more distributions employed, the better the fitting capability of the GMM. However, one limitation of the GMM with EM is that the convergence can be extremely slow as the number of distributions (K) increases [92]. Moreover, an extremely large number of distributions can cause a single-modal distribution to be fitted by two or more distributions of the GMM to achieve better fitting results. This is an undesirable case because the purpose of employing the GMM in this study is to fit the clusters formed around the rated power and rotor speed with a single Gaussian distribution to estimate the statistical moments of data in the stationary operating condition. Thus, this thesis recommends the use of the minimum number of distributions as long as the clusters formed around the rated

operating condition are properly fitted.

To define the criteria for the stationary operating condition (C_p and C_w) based on the statistical moments of the last distribution of the GMM, the three sigma rule was employed. The three sigma rule is that 99.87 % of data is within three standard deviations of the mean. Because the desired situation is to secure as much data as possible in Class I, the three sigma rule can be used for defining the conservative criteria for the stationary operating condition. Based on the three sigma rule, C_p and C_w can be defined as:

$$C_p = \mu_{K,p} - 3\sigma_{K,p} \tag{4.26}$$

$$C_w = \mu_{K,w} - 3\sigma_{K,w} \tag{4.27}$$

where $\mu_{K,p}$ and $\mu_{K,w}$ are the means of the last Gaussian distribution for power and rotor speed, respectively; $\sigma_{K,p}$ and $\sigma_{K,w}$ are the standard deviations of the last Gaussian distribution for power and rotor speed, respectively.

4.4 Case Studies

This chapter presents two case studies to demonstrate the proposed classification method. First, classification of operating conditions was demonstrated using data calculated from an analytical WT model with various levels of wind speed. Second, field data measured from a 2.5 megawatt wind turbine was used for classification.

4.4.1 Case Study with the Analytical WT Model

This chapter considers WT models with different levels of average wind speeds (i.e., $\overline{v}$=7.5, 8.5, and 10 m/s). Figure 4-9 presents results corresponding to the empirical PDF of power and rotor speed. Solid vertical lines and dashed vertical lines represent the results from Methods 1 and 2, respectively. As the average level of wind speed increases, clusters around the rated operating condition of the WT showed a dense distribution with large populations due to the high wind speed. Table 4-1 summarizes the criteria for the stationary operating condition as defined by Methods 1 and 2. The criteria derived by

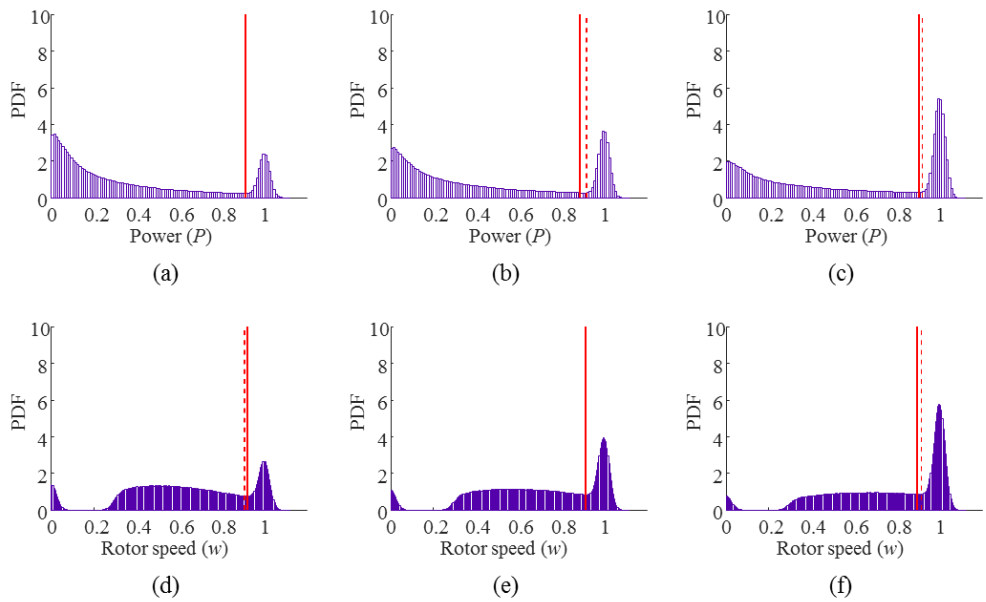

Figure 4-9 Criteria for the stationary operating condition where solid vertical lines represent the results from Method 1 and dashed vertical lines represent the results from Method 2: (a)-(c) power with average wind speed of 7.5, 8.5, and 10 m/s, respectively and (d)-(f) rotor speed with average wind speed of 7.5, 8.5, and 10 m/s, respectively.

Method 1 were unstable while having large standard deviations over three wind speeds. On the other hand, the criteria defined by Method 2 were in proportional to the level of wind speed while having small standard deviations.

Because it is beneficial for condition monitoring to obtain as many stationary vibration signals as possible, the criteria for the stationary operating condition can be defined as the minimum value between the results from Methods 1 and 2. However, the stationary operating condition is not likely to be guaranteed if the range of the stationary operating condition is set to be too large. In this case study, Method 1 required more data defined as Classes I and II than Method 2 does. Nevertheless, homogeneity of the vibration signals in Classes I and II defined using Method I should be carefully checked for ensuring the effective condition monitoring. A homogeneity evaluation method will be described in Chapter 4.5.1.

Table 4-1 Classification criteria defined using Methods 1 and 2 for the WT model with different levels of uncertainties

Criteria		Method 1 (Empirical PDF)	Method 2 (GMM)
C_p	v=7.5 m/s	0.910	0.915
	v=8.5 m/s	0.890	0.918
	v=10 m/s	0.905	0.920
Mean		0.902	0.918
Standard deviation		0.010	0.003
C_w	v=7.5 m/s	0.920	0.907
	v=8.5 m/s	0.915	0.912
	v=10 m/s	0.895	0.916
Mean		0.910	0.912
Standard deviation		0.013	0.005

4.4.2 Case Study with a 2.5 Megawatt Wind Turbine

This chapter used data from a 2.5 megawatt wind turbine in the Yeongheung wind farm, which is in the west side of the Republic of Korea. For the second case study, operating data from the WT (e.g., wind speed, rotor speed, and output power) were collected for one year at a one-Hz sampling rate. Collected data are represented in Figure 4-10 (a) and (b) as three dimensional histograms describing rotor speed and power. The principal operating mode of the WT was the idle control mode, which can be seen in the notable peak in Figure 4-10 (a) where both the power and rotor speed are around zero. When the data in the idle control mode was excluded, an additional cluster appeared around the rated power and rotor speed, as shown in Figure 4-10 (b). This cluster can be regarded as the data in the stationary operating condition, which was defined as Class I.

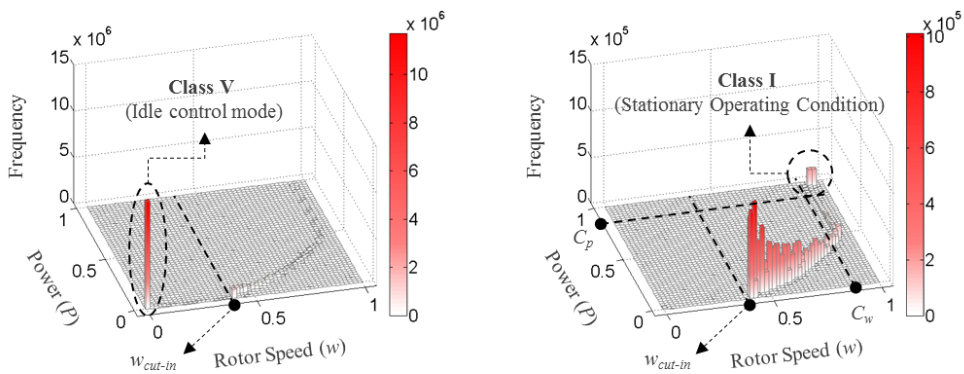

Figure 4-10 A three-dimensional histogram of power and rotor speed of the on-shore WT for one year: (a) full data and (b) data in which power is zero are filtered out.

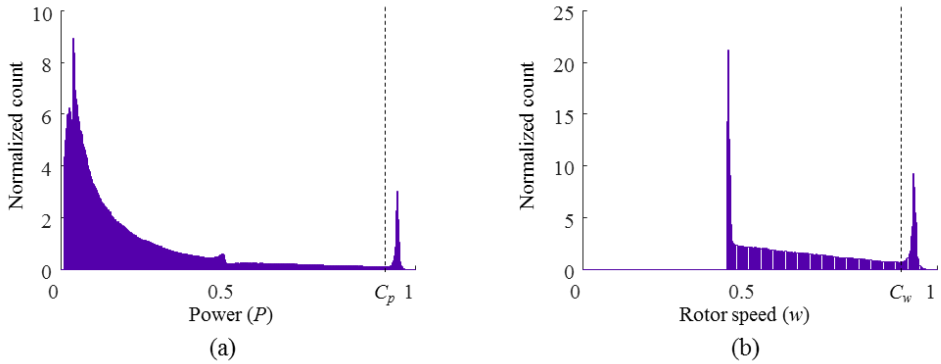

Figure 4-11 A relative histogram of the operating conditions of a WT for one year. Data in which power is equal to zero are filtered out for graphically tidy representation: (a) power and (b) rotor speed.

Table 4-2 The criteria for defining the stationary operating condition of the on-shore WT, as defined based on the two proposed methods

Criteria	Method 1 (Empirical PDF)	Method 2 (GMM)
C_p	0.915	0.920
C_w	0.890	0.920

Figure 4-11 (a) and (b) represent histograms for power and rotor speed data measured from the WT, respectively; Table 4-2 summarizes criteria for the stationary operating condition (i.e., C_p and C_w) as defined using Methods 1 and 2, respectively. Using the second method, it was found that at least five and four Gaussian distributions should be employed for the GMM to successfully fit the clusters formed around the rated power and rated rotor speed, respectively. In this case, results from the first method were smaller than those from the second method. Method 1 was thus used to define the criteria for the stationary operating

condition to obtain the greatest amount of possible homogeneous signals for condition monitoring. Note that if the homogeneity of the condition monitoring signals is not guaranteed, the classification criteria should be altered to use the results from Method 2.

The ratios of data observed for each of the defined classes are shown in Figure 4-12. It turned out that 2.85 percent of data were classified into Class I, which is thought to be most effective for condition monitoring. This amount of data corresponds to 41 minutes per day, on average. Class II, the quasi-stationary operating condition, consists of 5.65 percent of data, which corresponds to 81 minutes per day, on average. The WT operates in a nominally stationary rotational speed in both Class I and Class II. Thus, condition monitoring can be performed with a readily available, cost-effective signal processing techniques for data from about 122 minutes on average per day, without much concern about speed variation. However, power variation should also be considered for Class II data if the energy variation of the condition monitoring signal is evaluated and

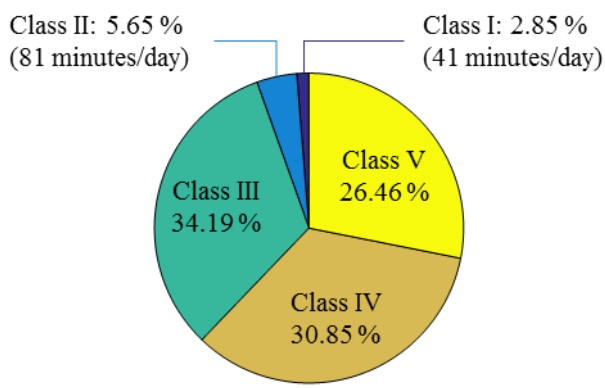

Figure 4-12 Classification results of the wind turbine data.

found to be large. It is also worth noting that Class IV and Class V, which may be trivial for condition monitoring of WTs, comprised an extremely large proportion of data (i.e., about 31% and 26% for Classes IV and V, respectively). This implies that unnecessary computational cost can be saved by excluding Class IV and Class V from the datasets to be processed for condition monitoring. Likewise, Class III, which has large variations in rotational speed and power, accounted for 34 percent of data.

4.5 Validation Study for Classification of Stationary Operating Conditions

To discuss the applicability of the proposed classification-based condition monitoring strategy, it is worth performing fault diagnostics under the various operating conditions that were defined in this research (i.e., Class I and II). However, it was not easy to gather condition monitoring signals from anomaly conditions from actual wind turbines. As an alternative, the research described in this chapter employed a two kilowatt testbed as shown in Figure 3-3. This testbed helps analyze the effect of the operating conditions on condition monitoring performance. For testbed operation, three representative operating conditions, representing Class I, Class II and Class III were measured for the 2.5 megawatt WT, as shown in Figure 4-13. Next, rotor speed and scaled torque were used for a control profile of the testbed. The vibration signal was measured using an accelerometer attached to the top of the gearbox with a sampling ratio of 25.6 kHz. The vibration signal from 100 minutes of operation was divided into 100

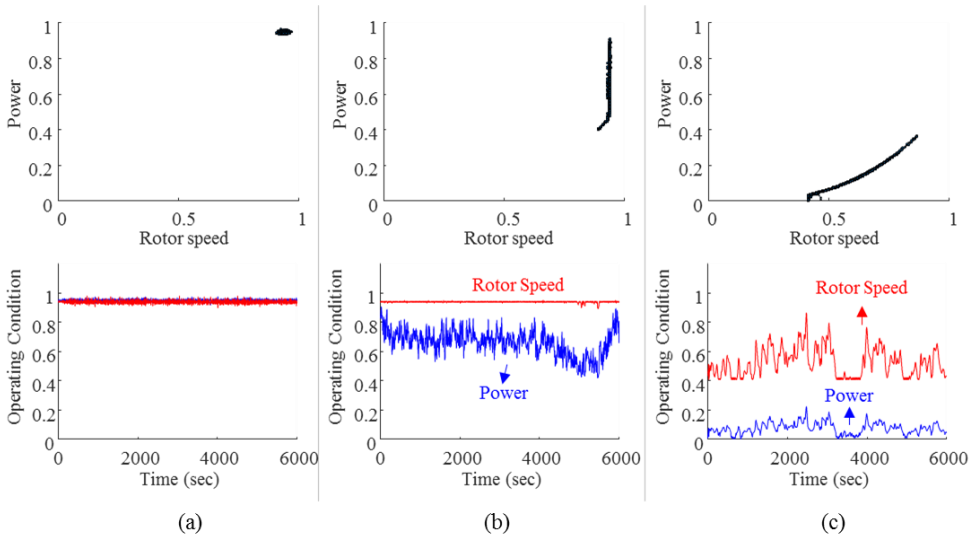

Figure 4-13 Representative operating conditions for control of the WT testbed: (a) Class I, (b) Class II and (c) Class III.

datasets for vibration-based fault diagnostics with one-minute vibration signals in each dataset. After the tests, the homogeneity of the vibration signals in each class was evaluated using a similarity test with a cross-correlation function. Finally, vibration-based condition monitoring was performed for each class.

4.5.1 Homogeneity Evaluation of the Vibration Signals

Provided that the vibration signal in a class is homogeneous, the vibration signal should have a similar vibration pattern and energy as long as the meshing condition of the gearbox remains identical. In this research, the homogeneity of the vibration signals in each class was evaluated by investigating the level of similarity of the vibration signals across datasets by means of a cross-correlation metric. Homogeneity of vibration signals was obtained by an average of

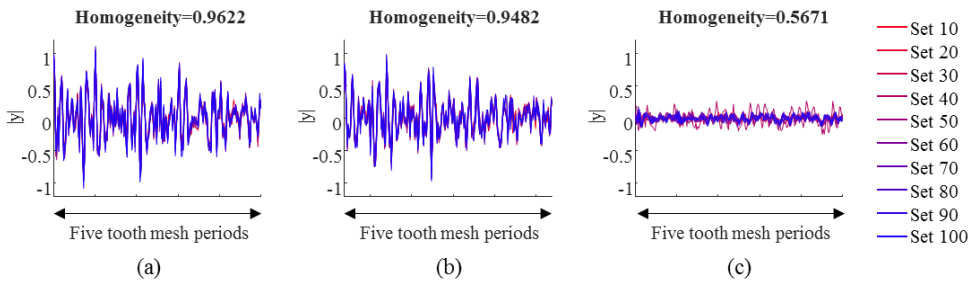

Figure 4-14 Homogeneity evaluation results of the vibration signals: (a) Class I, (b) Class II and (c) Class III

similarities evaluated from the number of the possible combinations of 100 datasets in each class, ${}_{100}C_2$ (=4950). Figure 4-14 compares the level of homogeneity of vibration signals for each class. For readability, vibration signals corresponding to only 10 datasets are aligned in Figure 4-14. As can be seen from the figure, the level of homogeneity of vibration signals in Classes I and II was greater than the level observed for vibration signals under Class III. Interestingly, the level of homogeneity of vibration signals in Classes I and II was similar despite the power variation in Class II. From these results, it can be concluded that variations in speed more significantly affect the level of homogeneity of vibration signals than do variations in power.

4.5.2 Vibration-based Condition Monitoring

To simulate an anomaly condition of the gearbox, a planet gear with line-type spalling was manufactured as shown in Figure 3-5 (a). For fault diagnosis of the gearbox, fast Fourier transform analysis was employed along with autocorrelation-based time synchronous averaging (ATSA) which will be

introduced in Chapter 5 [93]. Among various available health data, *FM*0 was used to evaluate the performance of the fault diagnostics results. *FM*0, which has been traditionally used for real-time condition monitoring of gearboxes, can be defined as Eq. (2.4).

Figure 4-15 (a)~(c) compares the histograms of *FM0* values derived from the tests performed during both normal and anomaly conditions of the gearbox under the Class I, Class II, and Class III, respectively. To quantify the degree of separability, Figure 4-15 indicates the probability of separation (POS), which gives one for perfect separation and zero for perfect overlap of PDFs from two classes [94]. In Class I and Class II, *FM0* from both the normal and anomaly conditions was clearly differentiated. This means that condition monitoring of the gearbox in Class I and Class II was feasible. In this case, the variation of the condition indicator in Class II was not large, despite the power variation. In Class III, *FM0* results from the normal and anomaly conditions were not perfectly separable, although there was some differentiation of overall magnitude between them. It is noteworthy that FM0 from the normal and anomaly conditions are not

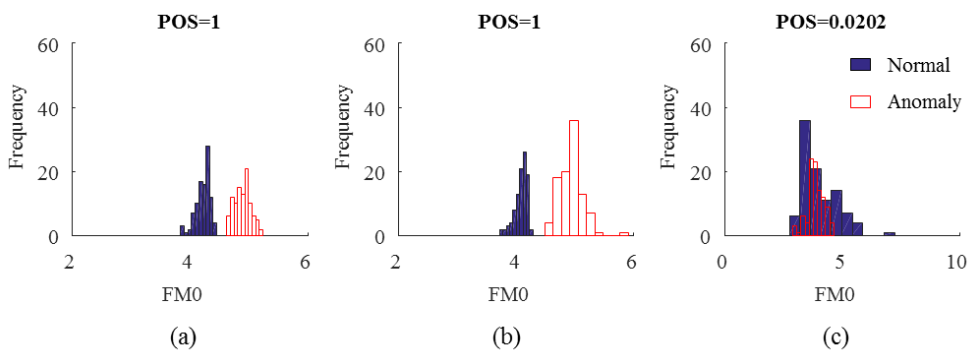

Figure 4-15 *FM0* obtained from normal and anomaly conditions of the planetary gearbox: (a) Class I, (b) Class II and (c) Class III.

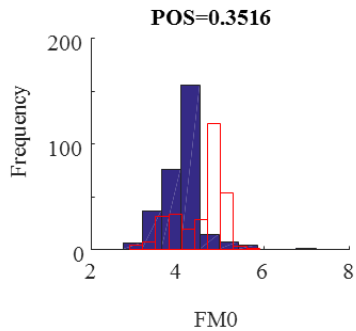

Figure 4-16 *FM0* obtained from normal and anomaly conditions of the planetary gearbox without considering operating condition.

differentiated when the proposed approach is not considered to classify the operating condition as shown in Figure 4-16.

4.6 Summary and Discussion

Techniques for monitoring the condition of gearbox have traditionally relied on the use of either stationary or non-stationary signals. However, to date, there has been no practical guideline outlining how to classify the operating condition of the gearbox for a class-wise condition monitoring purpose, and how to quantitatively define the ranges of the stationary operating condition. To address these challenges, this study devised a novel strategy to categorize the operating conditions of the gearbox using the empirical PDF and Gaussian mixture model (GMM).

For a representative study, this thesis employed a wind turbine (WT). In doing so, an analytical WT model with a generic control logic is adopted to analyze the fundamental characteristics of operating conditions. This strategy was used

because information about real-world control logic algorithms is proprietary and seldom released to the public. If available, a particular control logic for a real WT can be incorporated into the proposed method with only minor modifications. For example, for the case study using the WT in the field (See Figure 4-11 (b)), the classification method and criteria could be revised to consider the considerable amount of the data around the cut-in rotor speed.

Based on the analysis of fundamental characteristics of operating conditions identified by the analytic WT model, a strategy is proposed to classify the operation condition of WTs into five classes. WTs are expected to have distinct operating properties at each class. Furthermore, quantitative classification criteria are defined using the empirical PDF-based method (Method 1) and a Gaussian mixture model (GMM)-based method (Method 2). Class I and II data were extracted from WT signals using the proposed classification technique. For Class I and II data, the anomalous conditions of a gearbox in a WT testbed were clearly separated from the normal conditions through use of a low-cost signal processing technique (i.e., fast Fourier transform analysis with time synchronous averaging). With Class III data, there was overlap between the anomalous and normal conditions.

Method 2 requires considerable computational power for approximation of the optimal parameters for the GMM. The computational complexity of GMM is $O(KN_s^2)$ where K is the number of Gaussian distributions and N_s is the number of data points [95]. This challenge makes it difficult to update the classification criteria in real-time as more useful operating data are obtained. If the wind turbine requires a real-time update of the classification criteria using big data

while a high-power CPU is not available, thus, Method 1 would be more suitable for on-site utilization.

It is worth noting that the classification results of using Methods 1 and 2 can be inconsistent for different datasets. If both of Method 1 and 2 are available, it is recommended to adapt the method providing a lower level of criteria (C_p and C_w) to obtain the greatest data size used for the purpose of fault diagnostics, as long as the homogeneity of the signal is guaranteed.

From the case study, about 34% of data were classified into non-stationary operating condition classes, in which cost-efficient signal processing techniques cannot be effectively used for condition monitoring. It is worth noting that real data measured from a WT, about 120 minutes of data under the (quasi) stationary operating conditions (Class I and II) could be measured per day, on average. Thus, on average, 120 minutes of homogeneous condition monitoring signals are available for condition monitoring per day. Therefore, sufficient data exists such that, through the proposed method, an effective condition monitoring strategy can be implemented to support long-term operation and maintenance plans for wind turbines.

Chapter 5. Autocorrelation-based Time Synchronous Averaging (ATSA)

This chapter proposes autocorrelation–based time synchronous averaging (ATSA) to cope with the challenges associated with the current practice of TSA for planet gears. In the proposed approach, an autocorrelation function, which represents physical interactions between the ring, sun, and planet gears in the gearbox, defines optimum windows using actual kinetic responses, thereby preventing distortion of the signal during the TSA process. An order analysis with the ATSA signals makes accurate real-time diagnostics of planetary gearboxes practical.

5.1 Monitoring Position and Meshing Tooth of Planet Gears

For TSA of vibration signals measured from a planetary gearbox, position and meshing tooth of the gears should be tracked during the operation of the gearbox with an encoder. This can be achieved by accumulating meshing tooth information in a matrix form, which in this thesis is called the *meshing tooth matrix* of the ring gear (M_r) and the planet gear (M_p).

For identifying meshing tooth information, tooth numbers were pre-assigned to the inner gears of the planetary gearbox in meshing order as shown in Figure 2-6. Suppose that the tooth of a planet gear of interest indicated by “1” was

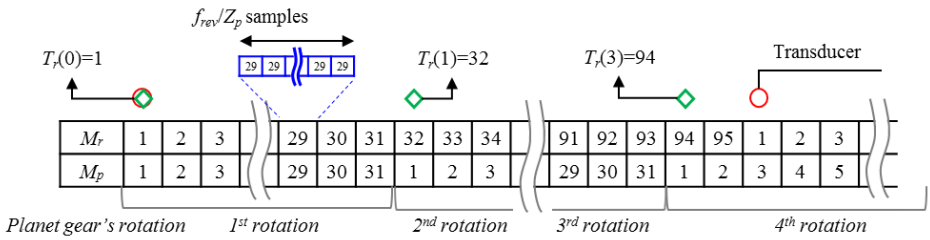

Figure 5-1 Meshing tooth matrix of the planet gear and the ring gear.

positioned under the sensor meshing with the tooth of the ring gear indicated by "1" at the initial state. The *meshing tooth matrix* of the ring gear and the planet gear starts from the number "1", and this value continues to be recorded for f_{rev_pr}/Z_p samples where f_{rev_pr} denotes the number samples assigned during one rotation of the planet gear relative to the ring gear, and Z_p is the number tooth of the planet gear. Thus, f_{rev_pr}/Z_p corresponds to the number of samples assigned during one-tooth meshing of the gear. As the next tooth of the gear begins to contact the ring gear, number "2" is accumulated in the M_r and M_p. After one rotation of the planet gear, M_p resets to "1" while M_r continues to record the next tooth number because typically the number of teeth of the ring gear is larger than the number of teeth of the planet gear.

Figure 5-1 shows an example of the *meshing tooth matrix* where a ring gear with 95 teeth and a planet gear with 31 teeth were used. Using *meshing tooth matrix* and *tooth sequence* defined from Eqs. (2.12) and (2.16), the position and the meshing tooth information of the ring gear and the planet gear of interest can be identified during the operation of the gearbox.

5.2 In-depth Study on the Autocorrelation Function for Vibration Signals

The autocorrelation function quantifies similarity between shape of the vibration signal at a current time and shape of the vibration signal after a typical time lag (τ) as:

$$R_{vv}(\tau) = E[v_{re}(t)v_{re}(t+\tau)] \tag{5.1}$$

where $E[\cdot]$ is the expectation operator; $v_{re}(t)$ is the resampled vibration signal in time domain; τ is the time lag.

When the time lag is zero, the autocorrelation becomes maximum with two identical signals, say $v(t)$, because of the same vibration pattern. Except for this special condition, autocorrelation is always equal to or smaller than the maximum. When the vibration signal after a typical time lag (τ) has no similar vibration pattern to the original vibration signal due to a different meshing condition (i.e., small similarity), the autocorrelation will give a small value. In the case of TSA for planetary gearboxes, similarity of the segments is not guaranteed because the meshing condition varies as the axes of the planet gears rotate. If one of the segments has no similarity, it should be excluded from the segments averaged by TSA. Thus, the range of the window function can be extended until 'similarity' of the extracted signal is assured.

Figure 5-2 shows an example of the autocorrelation function of vibration signals from a sensor that is attached to the top of the planetary gearbox in which ring gear with 95 teeth and three planet gears with 31 teeth are in mesh. As can be seen from the figure, the locally maximum autocorrelation values are observed when the rotation of the planet gear (n_{pr}) is at the particular integer numbers (e.g., 3, 6, 9, etc.), primarily at the interval of three.

Figure 5-3 explains how those peaks occur in the autocorrelation function. Suppose that the planet gear of interest is located under the sensor at the initial state. As the gearbox operates, the planet gear of interest starts to recede from the sensor, and vibration excited by the other gears and external sources begins to dominate the vibration signal measured from the sensor. This situation will give a small autocorrelation value by a small degree of similarity. The relative distance of the planet gear becomes short again after having three or six additional

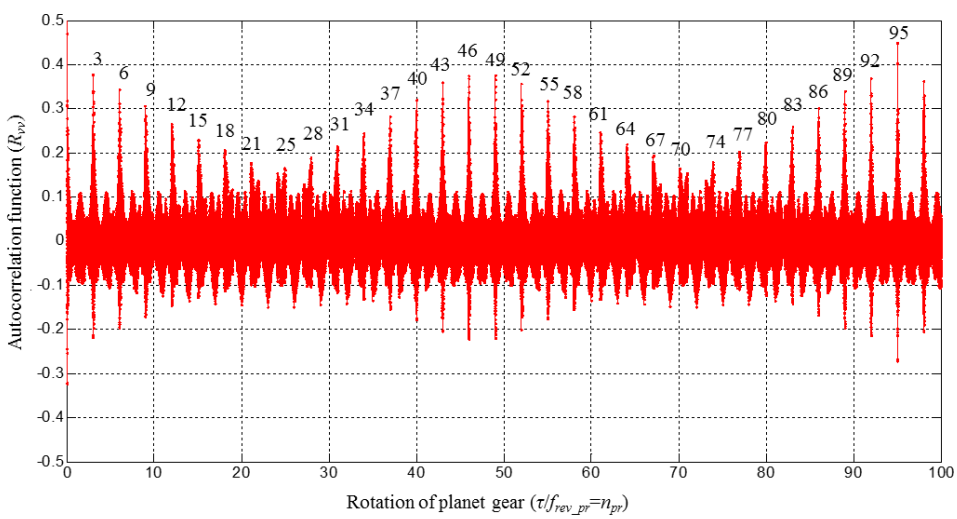

Figure 5-2 Autocorrelation function of vibration measured from a sensor attached to a gearbox housing.

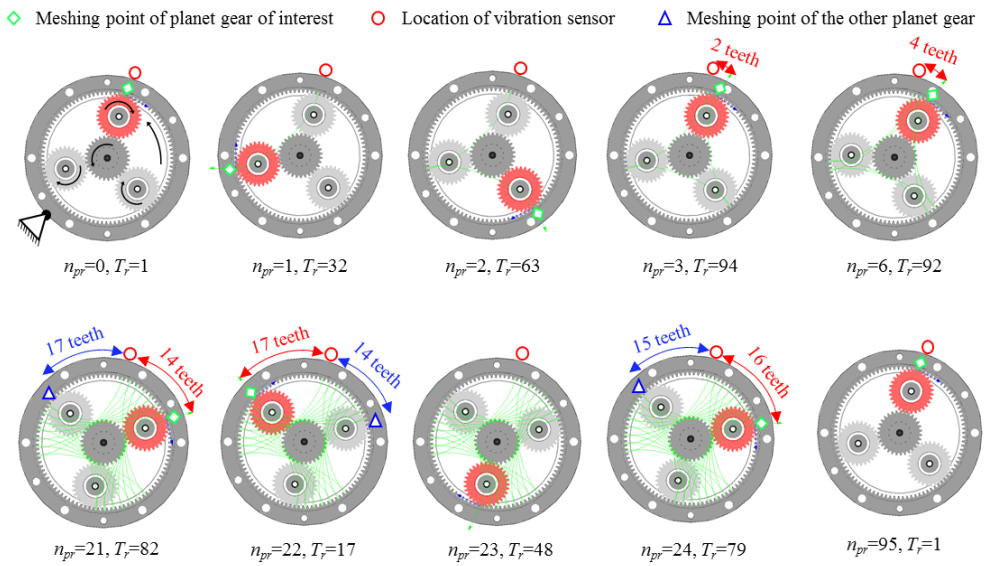

Figure 5-3 Meshing condition and transfer path along with rotation of planet gear.

rotations of the planet gear (n_{pr}=3 or n_{pr}=6). Because vibration from the planet gear of interest dominates the sensor data again at those moments, the sensor measures signals with a similar vibration pattern to the origin. The autocorrelation function, thus, has high peaks at n_{pr}=3 or n_{pr}=6. As a gearbox continues to run, the inner gears resets to the initial condition after $n_{pr|reset\_p}$ rotation of the planet gear relative to the ring gear as defined in (2.17). The example case employs the planetary gearbox with an $n_{pr|reset\_p}$ of 95. After 95 rotations of the planet gear (n_{pr}=95), the vibration signal measured from the sensor should show the maximum similarity to the original signal because of the identical meshing condition. As predicted, it is found from Figure 5-2 that the autocorrelation function has a high peak at n_{pr}=95.

From these observations, it is concluded that the similarity of the time-lagged vibration signal is guaranteed when the relative distance of the planet gear from

the sensor is short. Consequently, the range of the window function can be extended until the relative distance of the planet gear from the sensor is shorter than that of the other gears. Moreover, the autocorrelation function can help define the shape of the window function because the degree of similarity of the vibration signal was quantitatively modeled by the autocorrelation function. In other words, the newly designed window function gives a large weight when the similarity is guaranteed quite well, while it assigns a small weight when a small amount of similarity is assured. As a result, the proposed scheme enables to effectively isolate vibration signals produced by the planet gear of interest while minimizing interference of the other gears which are out of interest by considering actual kinetic responses of the gearbox.

5.3 Autocorrelation-based TSA

5.3.1 Representative Autocorrelation Function

As the gearbox operates, there are a number of chances to reproduce the initial meshing condition as the rotations of the planet gears reach multiples of the hunting tooth cycle for the planet gear (i.e., HTC_p). For every full cycle of the HTC_p, thus, the repetitive pattern of the autocorrelation function reappears. The autocorrelation function during the i^{th} full cycles of the HTC_p can be defined as:

$$R_{vv(i)}(\tau) = E\left[v_{re}\left(t-(i-1) f_{HTC\_p}\right) v_{re}\left(t-(i-1) f_{HTC\_p}+\tau\right)\right] \tag{5.2}$$

where f_{HTC_p} is the number of samples per HTC_p.

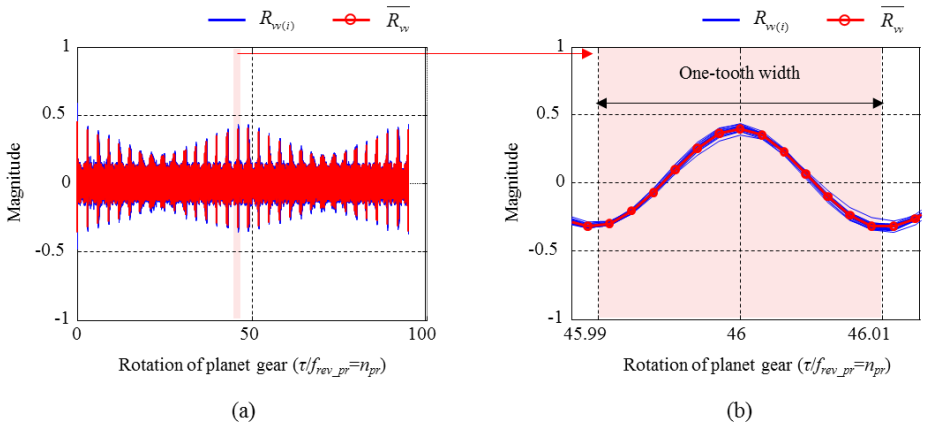

Figure 5-4 Representative autocorrelation function: (a) for 1 HTC and (b) for the period of one-tooth meshing around 46 rotations of the planet gear.

A representative autocorrelation function is defined as the ensemble average of the multiple sets of autocorrelation functions as illustrated in Figure 5-4.

$$\overline{R_{vv}}(\tau) = \frac{1}{N_{HTC\_p}} \sum_{i=1}^{N_{HTC\_p}} R_{vv(i)}(\tau) \tag{5.3}$$

where N_{HTC_p} is the number of hunting tooth cycles for the planet gear

5.3.2 Design of the Window Function

The range and shape of the autocorrelation-based window are defined in this chapter. First, the range of the window function is defined to extract the vibration signal only when the planet gear of interest is nearer than the other gears to the sensor. Second, the shape of the window function is defined by considering the degree of similarity. When a high level of similarity is assured, the window

function will have a high value to assign a large weight in extraction. Because similarity is quantitatively measured by the autocorrelation function, the shape of the window is derived by extracting the representative autocorrelation values where the planet gear of interest is nearest the sensor.

The number of planet gears' rotations at which the planet gear of interest is nearest the sensor can be identified by deducing it from a tooth sequence in Eq. (2.16) as:

$$T_r(n_{near}) \le D_{max} + 1 \text{ or } T_r(n_{near}) \ge N_r + 1 - D_{max} \tag{5.4}$$

where n_{near} is the number of rotations of the planet gear meshing with the ring gear nearest the sensor; D_{max} is the maximum distance of the planet gear to the sensor.

The maximum distance of the planet gear to the sensor (D_{max}) can be determined in the ring gear's domain to guarantee the range of 'nearest'. Because the ring gear can be divided into $2N_p$ regions based on the location of the N_p

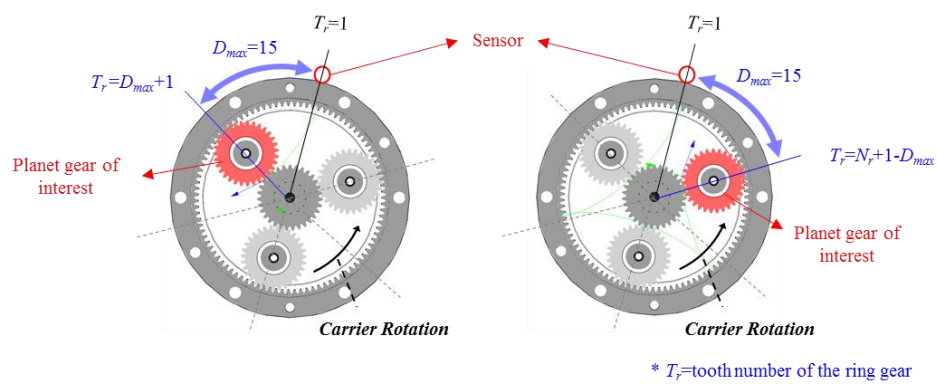

Figure 5-5 Maximum distance of the planet gear of interest to the sensor and corresponding position of the gears.

planet gears, D_{max} is defined in Eq. (5.5) as:

$$D_{max} = floor(\frac{Z_r}{2N_p}) \tag{5.5}$$

where $floor(a)$ rounds the value 'a' to the nearest integer less than or equal to a; For example, D_{max} of a planetary gearbox with three planet gears and a ring gear with 95 teeth is described in Figure 5-5.

The representative autocorrelation values satisfying Eq. (5.4) are marked as blue circles in Figure 5-6 (a). For design of the window function, the extracted autocorrelation values are transformed to the ring gears' tooth domain as shown in Figure 5-6 (b). Then, the autocorrelation-based window defined in the entire range of the signal (W_{ATSA}) can be constructed as shown in Figure 5-7. Every local window has its center as the planet gear of interest passes the sensor periodically in the carrier rotation.

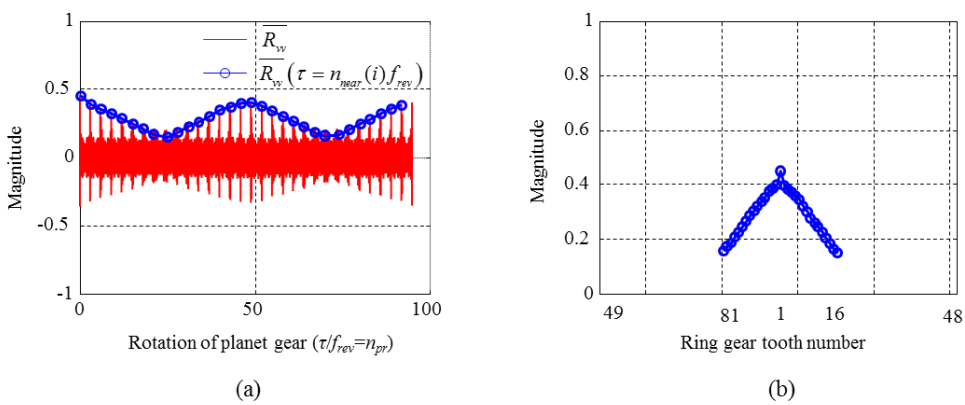

Figure 5-6 Derivation of the window function based on representative autocorrelation function: (a) extraction of window function and (b) window function along with ring gears' tooth.

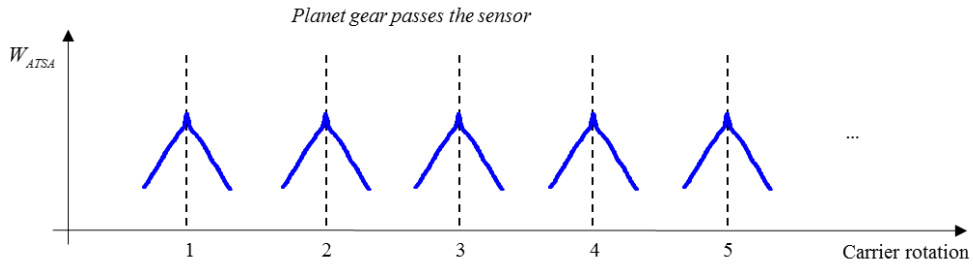

Figure 5-7 Autocorrelation-based window function.

5.3.3 Application of Window Function for TSA

Autocorrelation-based window defined in Chapter 5.3.2 can be employed for the general procedure of TSA for a planet gear, such as dividing, windowing, transforming, and averaging, which were introduced in Chapter 2.3.2. For a clarity, this chapter describes the abovementioned procedures in more detail.

Detailed procedures of autocorrelation-based TSA are illustrated in Figure 5-8. In windowing, the resampled vibration signal (v_{re}) is multiplied by the autocorrelation-based window (W_{ATSA}) to get the windowed signal (v_{win}). The windowed signal is then re-arranged to the planet gear's tooth domain through a transforming step. The *meshing tooth matrix* helps find which tooth of the planet gear produces the windowed signals. When tooth number i of the planet gear is of interest to the TSA, f_{rev_p}/Z_p samples corresponding to the number of samples assigned during one-tooth meshing of the gear can be found by searching i in the *meshing tooth matrix* of the planet gear (M_p). The k^{th} tooth meshing vibration vector of tooth number i of the planet gear is denoted as $v_{(i,k)}$. Figure 5-8 illustrates the tooth meshing vibration vectors of tooth number one as an example.

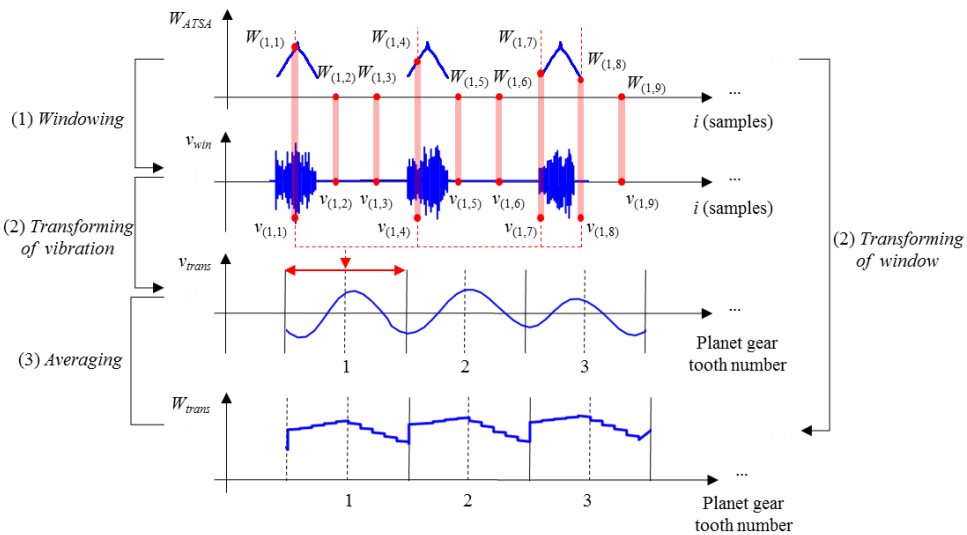

Figure 5-8 Averaging of signal for ATSA.

Then, the transformed vibration signal corresponding to tooth number *i* of the planet gear, which is denoted as v_{trans}, can be defined as:

$$v_{trans}((i-1)\cdot\frac{f_{rev\_pr}}{Z_p}+1:i\cdot\frac{f_{rev\_pr}}{Z_p})=\sum_{k}v_{(i,k)} \tag{5.6}$$

During windowing, the vibration signals are deformed by the non-unity shape of the windows. Moreover, the summation of the windowed signals produces undesirable modulation of the signal. To remove the undesirable modulation of the signal, the pure effect of modulation should be identified. For this purpose, all procedures for defining a transformed vibration signal are performed by applying the constant function with the magnitude of one on behalf of the vibration signal, which results in a transformed window signal (W_{trans}). Transformed window signal corresponding to tooth number *i* of the planet gear can be defined as:

$$W_{trans}((i-1)\cdot\frac{f_{rev\_pr}}{Z_p}+1:i\cdot\frac{f_{rev\_pr}}{Z_p})=\sum_k W_{(i,k)} \tag{5.7}$$

where $W_{(i,k)}$ is extracted from the window function as tooth number i of the planet gear mesh with the ring gear for the k^{th} time. In Figure 5-8, $W_{(i,k)}$ that corresponds to tooth number i of the planet gear is illustrated as an example.

If there is no modulation effect, the transformed window function should have a unit value. However, as shown in Figure 5-8, the transformed window signal (W_{trans}) is varying, which represents the pure effect of the undesirable modulation. To remove this undesirable effect, the ATSA signal can be defined by dividing the transformed vibration signal by the transformed window.

5.4 Case Studies

Two case studies are employed to demonstrate the effectiveness of ATSA: vibration signals generated by the analytical model and those measured from a testbed ran for 100 minutes (i.e., 6000 seconds) with slight speed and torque variation under the stationary operating condition as shown in Figure 4-13 (a). First, the operating data was divided into 100 data sets in which one minute of operating data is included. It corresponds to 393 carrier cycles of the gearbox. Second, the identical operating data was divided into 300 data sets so that each data set contains 131 carrier cycles of the gearbox. Signals from TSA with a Tukey window having five-tooth width, which is the most recently developed TSA for planetary gearboxes, are used for a comparison study.

5.4.1 Case Study #1: Analytical Model

This chapter focuses only on the instances when the planet gear meshes with the ring gear under the sensor. Consequently, a faulty signal caused by contact between the faulty tooth of planet gear and the sun gear was not considered. In this study, a half-period sine wave with the amplitude of 0.07 was added to tooth number 5 of the planet gear to describe 7% of the amplitude of vibration signal from the faulty tooth. Non-coherent random noise was also considered by adding 0.1 for A_{noise} in Eq. (3.1) to emulate many noise sources including measurement error, environmental noise, etc. For simulation of modulation effect, signal transfer function due to the revolving planet gears (i.e., a_n in Eq. (3.1)) was designed to have less weight (i.e., $\min(a_n)=0.5$) when the planet gear recedes from the sensor, and greater weight (i.e., $\max(a_n)=1$) when the planet gear is positioned under the sensor [69], [70].

The simulated vibration signals were processed with the TSA and the ATSA. Then, v_{RES} and v_{DIF} of the processed signals were investigated. It was found that v_{DIF} in the tooth domain was sufficient to figure out the abnormal signature in analytical model. Figure 5-9 compares two difference signals resulting from ATSA and conventional TSA with the Tukey window. Figure 5-9 (a) and (b) used the simulated vibration signals for 393 carrier cycles and 131 carrier cycles, respectively. Size of data (e.g., 393 and 131 carrier cycles) was determined to correspond with the case study with testbed. TSA with the Tukey window failed to clearly show the abnormal signature in the case with operating data for 131 carrier cycles since the size of data was too limited to perform sufficient TSA processing with such a narrow-range window. An abnormal signature clearly

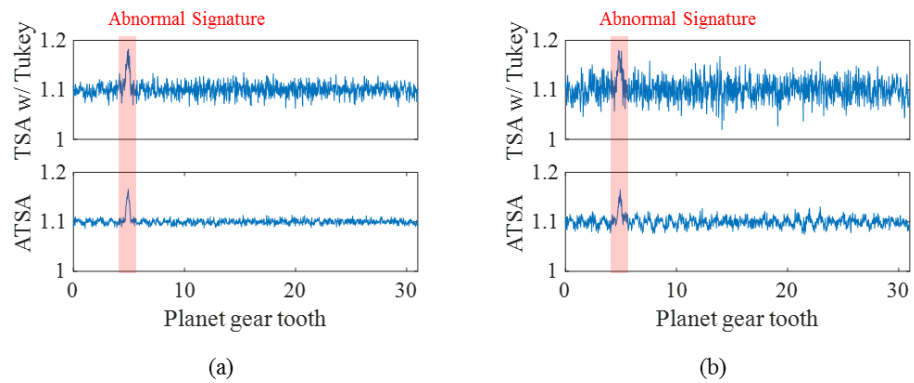

Figure 5-9 DIF of vibration signal produced by a planet gear from the simulation: (a) data length: 393 carrier cycles and (b) data length: 131 carrier cycles.

appeared when 393 carrier cycles of operating data were used for the TSA with the Tukey window. In contrast, ATSA results showed that it can clearly detect an abnormal signature in both cases: operation data for 131 carrier cycles and also even more clearly for operation data for 393 carrier cycles.

5.4.2 Case Study #2: Testbed

In this study, a planet gear with partial tooth breakage was tested to evaluate the performance of ATSA as shown in Figure 3-5 (b). To detect the signature generated by the faulty planetary gear, this case study employed various health data that can be defined from the TSA and difference signal. First, this study employed *FM0* which is the simplest form of health data that does not require any further process except the TSA. Additionally, to detect the impact-type fault signatures cause by short-term engagement of the faulty tooth, high-level statistical moment of difference signal (i.e., FM4, M6A and M8A) can be

employed. We found that *M8A* that shows high correlation to *M6A* for most of cases. Thus, in this paper, *FM4* and *M6A* are employed for fault diagnosis. The signals in the tooth domain were not presented since the analysis of residual signal and difference signal did not show any signature associated with the fault because of the large amount of noise from uncertainties of the testbed.

In Figure 5-10 and Figure 5-11, a comparison of the results using Tukey-based TSA and ATSA is presented using *FM4* and *M6A*. Each data point represents health data (HD) processed with Tukey-based TSA and ATSA for which 393 carrier cycles or 131 carrier cycles of operational data were used. As shown in Figure 5-10 and Figure 5-11, the HD from the abnormal condition represent the large magnitude compared to those from the normal condition, as can be inferred from the definition of the HD. When a sufficient amount of data is available (e.g., 393 carrier cycles), in Figure 5-10, HD processed with ATSA can clearly differentiate the normal condition from the abnormal condition whereas HD processed with TSA are uncertain, at best. When the available data is limited (e.g., 131 carrier cycles), HD from TSA failed to differentiate the normal condition and the abnormal condition of the gearbox, whereas HD from ATSA could did as shown in Figure 5-11. When one more HD (*FM0*) is employed, it can be shown in Figure 5-12 that ATSA effectively distinguished the normal condition from the abnormal condition with the limited amount of data whereas TSA couldn't do.

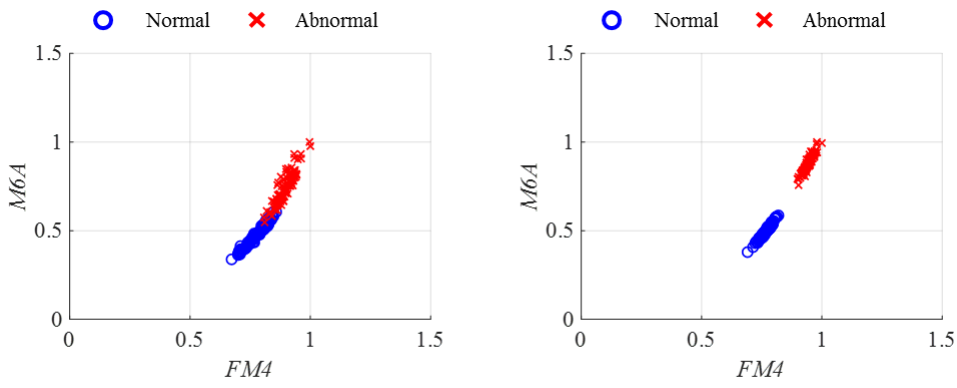

Figure 5-10 Two health data (*FM4* and *M6A*) using 393 carrier cycles of operational data measured from the testbed: (a) processed with TSA and (b) processed with ATSA.

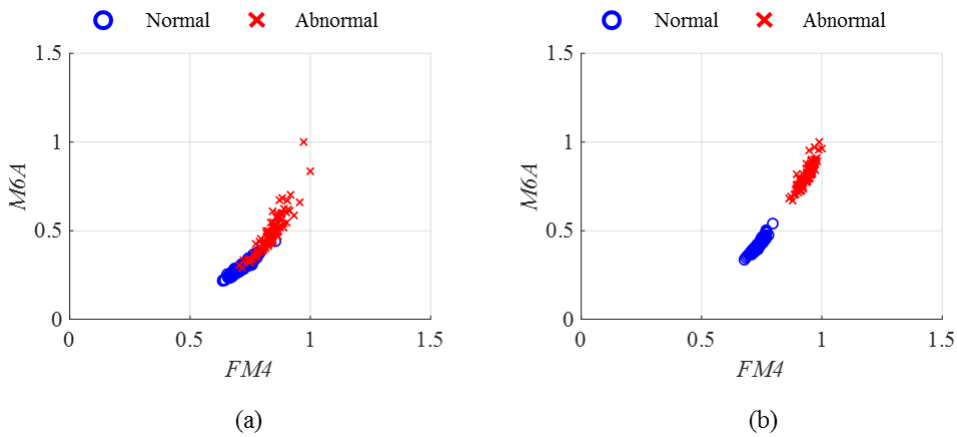

Figure 5-11 Two health data (*FM4* and *M6A*) using 131 carrier cycles of operational data measured from the testbed: (a) processed with TSA and (b) processed with ATSA

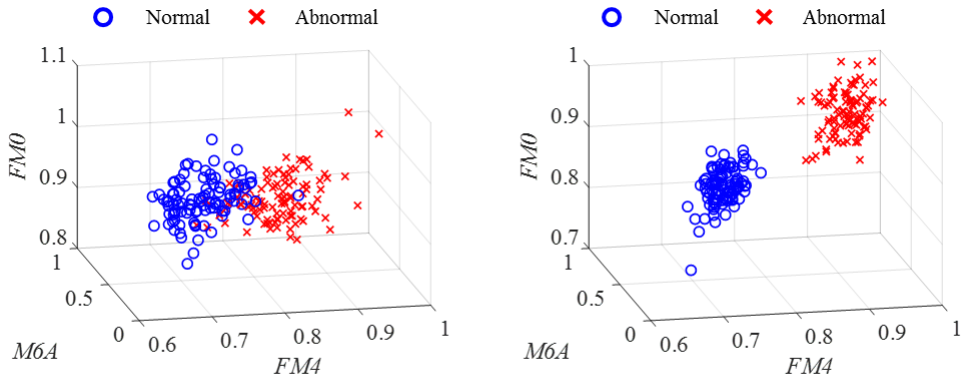

Figure 5-12 Three health data (*FM4*, *M6A* and *FM0*) using 131 carrier cycles of operational data measured from the testbed: (a) processed with TSA and (b) processed with ATSA.

5.5 Summary and Discussion

The autocorrelation-based time synchronous averaging (ATSA) method was proposed as an improved pre-processing technique for fault diagnosis of planetary gearboxes. Autocorrelation analysis of the vibration signal was performed to identify the instances when a similar pattern of vibration occurred. A window function with an optimized size and shape was designed based on the autocorrelation function to overcome the limitations of the narrow-range and full-range windows. It was demonstrated that, using the simulated vibration signals, ATSA with the newly designed window function outperformed the Tukey window-based TSA in identifying a fault signature in the tooth domain. Another case study was performed by employing 393 and 131 carrier cycles of operational data. It was verified that TSA is feasible when the available data is

sufficient. However, such a long time period of stationary operation rarely happens in a real field. For example, this amount of data corresponds to about 20 minutes of stationary operation for a wind turbine operating at 20 rpm at the blade. Therefore, it is reasonable to conclude that ATSA is an efficient pre-processing technique for fault diagnosis of planetary gearboxes, especially where the amount of available stationary data is limited (e.g., less than 7 minutes of operation), where conventional TSA is not feasible. With the signal processed with ATSA, effectiveness of any kinds of works related to condition monitoring of the gear, such as fault alarming, fault diagnostics, prognostics, etc. can be enhanced significantly compared to the methods with the conventional TSA.

Chapter 6. Tooth-wise Fault Identification of Gearbox using Health Data Map (HDMap)

This chapter proposes an original idea for tooth-wise fault identification of a planetary gearbox based on a health data map that can be used even with unexpected vibration modulation characteristics. To do so, enveloped kurtosis in a moving window is calculated as health data in the sample domain without the extraction and mapping process required for conventional TSA with the narrow-range window function. Health data in the sample domain is aligned on a health data map in the domains of a pair of gear teeth (i.e., ring-planet gear teeth pairs and ring-sun gear teeth pairs), which leads to a synthesized visualization of faults in planet gears and a sun gear. In addition, this chapter propose an encoder-less health data map using a roughly reconstructed angle information based on a Hilbert-based phase estimation [96], [97].

This chapter is organized as follows. First, time synchronous averaging (TSA) and difference signal is defined for one hunting tooth cycle (HTC) in sample domain without the use of the signal extraction window function. In Chapter 6.2, health data which quantifies the fault of the gearbox is defined from the difference signal in sample domain. In Chapter 6.3, difference signal and health data in sample domain are represented in tooth domain for a synthesized visualization of the faults in gears. In addition, encoder-less health data map is introduced in the same chapter. Chapter 6.5 presents two case studies using the analytical model and the testbed.

6.1 TSA and Difference signal for One Hunting Tooth Cycle (HTC) in Sample Domain

An overview of the procedures used to calculate the TSA signal and the difference signal (v_{DIF}) for one *HTC* is illustrated in Figure 6-1. For a general description of the procedures in this chapter, HTC_p & HTC_s and $n_{c|reset\_p}$ & $n_{c|reset\_s}$ in Eqs. (2.14) and (2.15) are denoted as unified notations that are *HTC* and $n_{c|reset}$, respectively. First, vibration signals are divided into multiple sets based on *HTC* in such a way that one set contains signals for $n_{c|reset}$ carrier rotations of the gearbox. Each set has equivalent meshing combinations of the ring-target gear teeth pairs. Next, the divided signals are ensemble averaged to reduce the non-

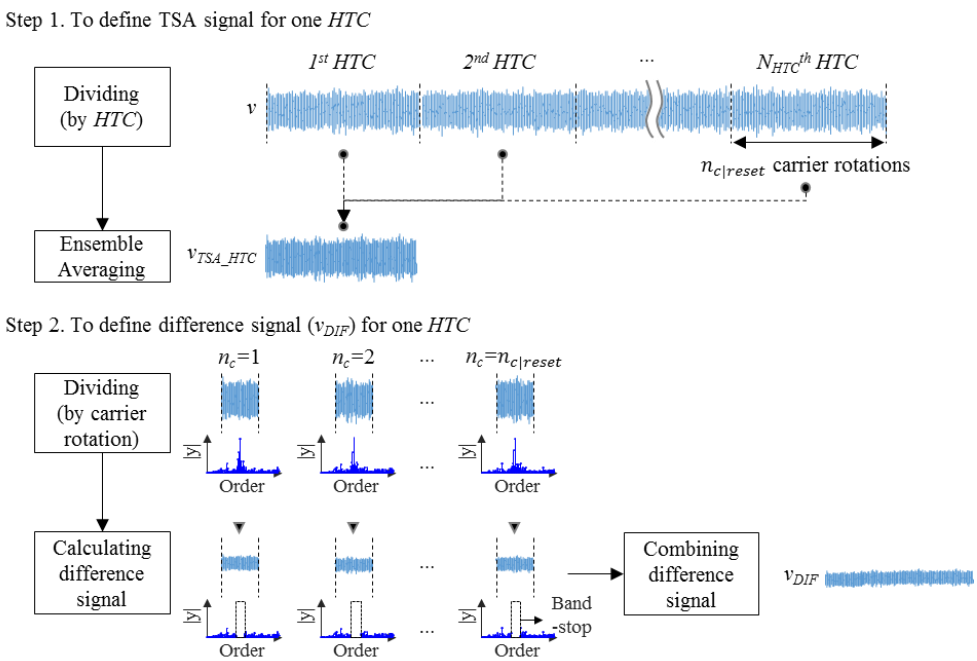

Figure 6-1 Procedures for calculating time synchronous averaging signal and difference signal for one hunting tooth cycle

coherent noise. Because the resulting TSA signal accounts for every possible meshing combination of the teeth pairs for one *HTC*, it can now serve as a source for tooth-wise fault identification of the gearbox.

Despite the TSA processing, fault-related features can be buried by the remaining regular components generated from gear meshes. Thus, for an effective fault diagnostics of a gearbox, it is commonly suggested to use difference signal (v_{DIF}) as introduced in Chapter 2.2.2. In general, resolution of the order domain for a TSA signal is "1" because the size of the signal corresponds to one rotation of the shaft [38]. Thus, it is convenient to exactly remove the regular components from the order domain using an ideal band-stop filter [42]. However, resolution of the order domain for v_{TSA_HTC} is much finer because the data contains signals corresponding to multiple rotations of the shaft (i.e., $n_{c|reset}$ carrier rotations). In this case, it is almost impossible to exactly remove the regular components that will be represented by a few decimal places in the order domain.

To solve this difficulty, the averaged signal is divided into multiple sets based on the carrier rotation so that one set corresponds to one carrier rotation, as shown in the second step of Figure 6-1. While the resolution in the order domain gets lower through this process, gear mesh frequencies and their harmonics converge to the integer frequency components in the order domain. Then, the difference signal can be easily obtained from each set using ideal band-stop filters. The calculated difference signal at each set can be combined to form a v_{DIF} for one *HTC*. The number of harmonics and sidebands removed for v_{DIF} is dependent on the characteristics of the system [38]. In this thesis, up to 10

harmonics and 5 sidebands at each side of the harmonics are removed from the TSA signal.

6.2 Health Data for One Hunting Tooth Cycle (HTC) in Sample Domain

Health data is a quantified measure of a fault in a system. If the regular components and the non-coherent noise are effectively removed by calculating the difference signal, the difference signal can be used as sample-wise health data.

However, rather than using the difference signal itself, it is sometimes suggested to calculate various health data to enhance sensitivity to the faults. Among various health data that can be derived from the difference signal, the research described in this chapter employed *FM4*, which is known to be robust to the torque variation, while being sensitive to a fault of the gears [41]. *FM4* can be obtained by calculating a normalized kurtosis of the difference signal. Because kurtosis is sensitive to a small number of outliers in a dataset [98], *FM4* is specialized to detect a single tooth defect that causes an abrupt peak in the vibration signal during the short-term engagement of the faulty tooth [99].

To fully utilize the property of kurtosis in detecting outliers in a time series, Constantinos et al. proposed use of a sliding window in which a localized kurtosis is calculated sequentially [100]. Kurtosis in a sliding window abruptly increases at the instances when either the window starts to contain the outliers or when the window gets out of the outlier range. Because the window contains a

relatively small number of outliers at those instances, detecting performance of the outlier can be enhanced. In addition, location and duration of the outliers in the time domain can be identified by analyzing the location of a sliding window with a high value of kurtosis [100]. Using this concept, this thesis proposes to calculate the *FM4* with a sliding window in the sample domain, which can be defined by the following equation:

$$FM4(n) = \frac{L\sum_{i=n-L/2+1}^{n+L/2}\left(v_{DIF}(i) - \frac{1}{L}\sum_{i=n-L/2+1}^{n+L/2}\left(v_{DIF}(i)\right)\right)^4}{\left[\sum_{i=n-L/2+1}^{n+L/2}\left(v_{DIF}(i) - \frac{1}{L}\sum_{i=n-L/2+1}^{n+L/2}\left(v_{DIF}(i)\right)\right)^2\right]^2} \quad (6.1)$$

where L is width of the sliding window function and $v_{DIF}(i)$ is i^{th} point of v_{DIF}.

It has been previously reported that kurtosis performs better when the sliding window has wider width. [100]. However, windows with too wide a range, and thus with multiple anomaly events, lead to low sensitivity for outlier detection [98], [100]. Thus, the sliding window should be designed to have the maximum possible width, while still being narrower than the period of the anomalies [53]. For fault diagnosis of a gearbox, the period of the anomalies can be characterized by the fault characteristic period of the planet gear (T_{pf}) and the sun gear (T_{sf}), which can be defined by the following equations [55]:

$$T_{pf} = Z_p\, tmp \quad (6.2)$$

$$f_{sf} = \frac{Z_s}{N_p} tmp \tag{6.3}$$

where *tmp* denotes tooth meshing period.

For a planet gear, a faulty tooth meshes with the ring gear once per rotation, with a Z_p tooth-meshing period. On the other hand, signals from a faulty tooth of the sun gear are generated by N_p planet gears. Thus, a faulty signal is generated as often as the number of planet gears for each single rotation of the sun gear with a Z_s/N_p tooth-meshing period. The width of the window can be defined as shortest period of anomalies that can be defined by Eq. (6.3).

The difference signal (i.e., v_{DIF}) and health data (i.e., *FM4*) were defined to represent the condition of the teeth pairs in the sample domain. To enhance the sensitivity and robustness of the calculated values to the faults, Hilbert transform can be employed to obtain an envelope of the signals as:

$$v_{DIF}\_env(n) = \sqrt{v_{DIF}(n)^2 + \mathrm{HT}\left(v_{DIF}(n)\right)^2} \tag{6.4}$$

$$FM4\_env(n) = \sqrt{FM4(n)^2 + \mathrm{HT}\left(FM4(n)\right)^2} \tag{6.5}$$

where HT(·) represent Hilbert transform.

The envelope of the signals via Hilbert transform has two distinct features. First, it traces the global amplitude with a smoothed response, which results in

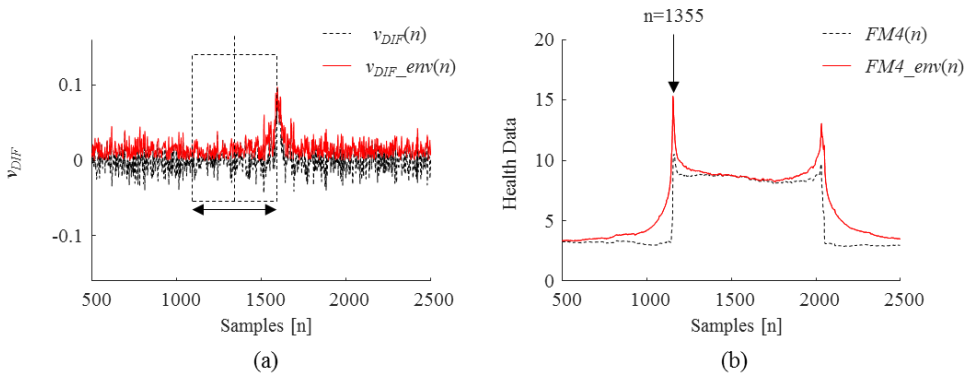

Figure 6-2 FM4 with sliding window: (a) difference signal and (b) enveloped FM4 with the sliding window.

low fluctuation in the sample domain. Second, any abrupt increase of the calculated values by engagement of a faulty tooth is further magnified by the property of Hilbert transform that converges to infinity with abrupt peaks, such as the Dirac delta function and increasing edge of a rectangular function [101].

Figure 6-2 describes how the calculated values are represented in the sample domain. As shown in Figure 6-2 (a), the difference signal from the faulty gearbox can be considered as a Gaussian noise with a short-term anomaly generated by the meshing of the faulty tooth of the gear. In this example, the width of the sliding window was set to be 500 for purposes of illustration. It can be found that the short-term anomaly of the difference signal in Figure 6-2 (a) is divided into two maximized health data by the sliding window, as shown in Figure 6-2 (b). Health data increases as the sliding window starts to include the anomaly or starts to get out of the anomaly in the difference signal. It is also noteworthy that the envelope of v_{DIF} represents a trend of the data in the sample domain, while excluding negative values of data. In addition, the increasing health data gets highlighted when the envelope is applied to *FM4*, as shown in Figure 6-2 (b).

6.3 Health Data (HD) in Tooth Domain: HDmap

Health data in the sample domain represent the condition for every possible meshing combination of teeth pairs between the ring gear and the target gear. By tracking the tooth information for the increasing difference signal and health data, the location of the faulty tooth can be identified. However, it is time-consuming to check the tooth information and periodicity of the anomaly in the sample domain. Moreover, it is almost impossible to identify periodically repeated anomalies in the sample domain if the regular components and random noise are not perfectly removed. To enhance the data interpretability, this research proposes to advance the concept of the local meshing plane [54] to represent the difference signal and health data in the domains of a pair of gear teeth (i.e., ring-planet gear teeth pairs and ring-sun gear teeth pairs). Visualization of the difference signal and health data in the tooth domain is called an HD-map in this thesis.

For *HD map*, continuous tooth-meshing matrix for ring gear (M_{r_con}), planet gear (M_{p_con}) and sun gear (M_{s_con}) for one *HTC* should be constructed. Different

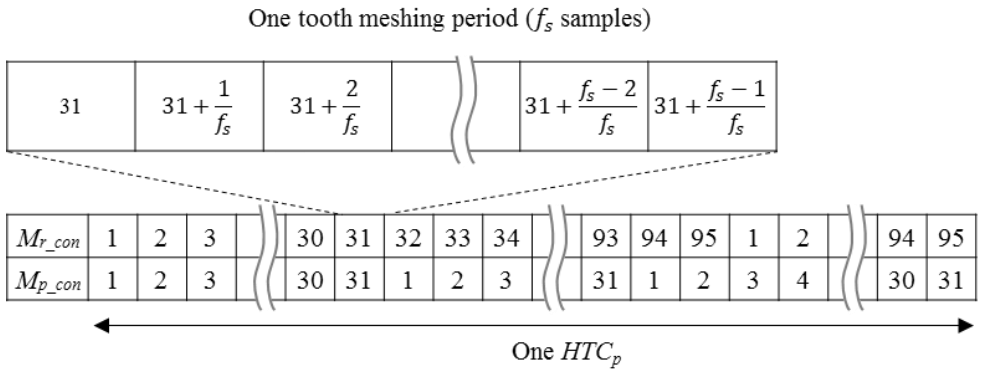

Figure 6-3 Meshing tooth matrix of a ring gear and a planet gear for one hunting tooth cycle

from the meshing tooth matrix defined in Chapter 5.1, tooth-meshing matrix in this chapter should be continuous with the intervals of $1/f_s$ where f_s is the number of samples assigned during one tooth meshing period. A typical example of the tooth-meshing matrix is shown in Figure 6-3. Each element monotonically increases with the intervals of $1/f_s$, and is reset to '1' as it reaches $Z+(f_s-1)/f_s$, where Z is the number of teeth in the target gear and f_s is the number of samples assigned during one tooth-meshing period. The number of elements of the tooth-meshing matrix for the ring-planet gear teeth pairs (i.e., M_{r_con} and M_{p_con}) or ring-sun gear teeth pairs (i.e., M_{r_con} and M_{s_con}) is equivalent to the number of samples in the difference signal and *FM4* for one HTC_p or one HTC_s, respectively. Thus, the enveloped difference signal and *FM4* for the planet gear and the sun gear can be represented in the tooth domain by the following relationships:

$$\text{HD-map}_{(\cdot)\_planet}(r,p) = (\cdot)\_env\left(M_{r\_con}(n) = r \,\&\, M_{p\_con}(n) = p\right) \tag{6.6}$$

$$\text{HD-map}_{(\cdot)\_sun}(r,s) = (\cdot)\_env\left(M_{r\_con}(n) = r \,\&\, M_{s\_con}(n) = s\right) \tag{6.7}$$

where $(\cdot)$ can be v_{DIF} or *FM4, and r, p,* and *s* are axes of HD-map that represent the domains of the ring gear tooth, planet gear tooth, and sun gear tooth, which are ranging from 1 to $Z+(f_s-1)/f_s$ with the resolution of $1/f_s$ and where Z is the number of teeth in the corresponding gear.

As found in Eqs. (6.6)-(6.7), an HD-map is a representation of the enveloped difference signal or *FM4* in terms of ring-planet gear teeth pairs or ring-sun gear teeth pairs. If a typical tooth of the planet gear or sun gear has a fault, values for the corresponding tooth of the axes in the HD-map will be highlighted as a

horizontal line. In particular, a fault in the sun gear will be represented as multiple separate horizontal lines because the faulty tooth of the sun gear meshes with multiple planet gears.

To analyze the effect of the fault on each gear domain, the calculated signal can be projected for each axis of the HD-map by averaging the values. For example, projection of HD-map$_{(\cdot)_planet}$ and HD-map$_{(\cdot)_sun}$ to *x*-axis (i.e., ring gear domain) can be defined as:

$$(\cdot)_{\_proj\_planet}(r) = \frac{1}{N}\sum_{p} \text{HD-map}_{(\cdot)\_planet}(r, p) \tag{6.8}$$

$$(\cdot)_{\_proj\_sun}(r) = \frac{1}{N}\sum_{s} \text{HD-map}_{(\cdot)\_sun}(r, s) \tag{6.9}$$

Likewise, projection of the HD-map to *y*-axis (i.e., planet gear domain or the sun gear domain) can be simply obtained from each HD-map.

Figure 6-4 represents an HD-map using the enveloped difference signal for a planet gear of interest from the analytical model under the healthy condition. To represent the noise, 0.1 of A_{noise} in Eq. (3.1) is considered. As shown in Figure 6-4 (a), the condition of the gearbox for every possible tooth-meshing combination can be visually identified. Because the gear is in the healthy condition in this case, the HD-map has no distinct features. Figure 6-4 (b) is an enlarged view of Figure 6-4 (a) around tooth numbers 48 and 16 of the ring gear and the planet gear, respectively. The enveloped difference signal from one tooth-

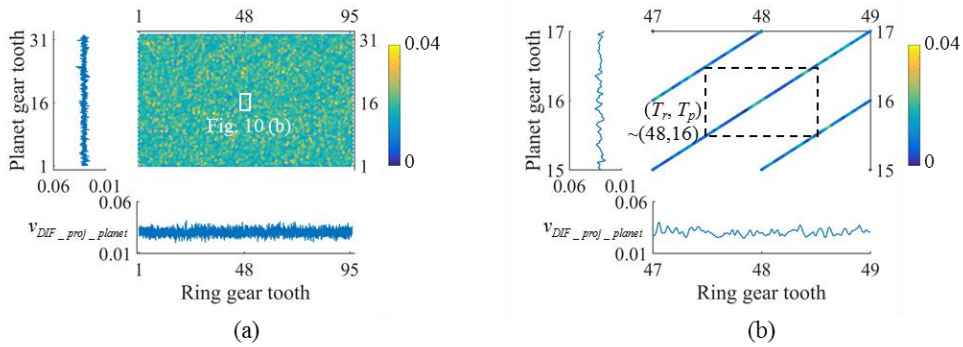

Figure 6-4 Health data map using an enveloped difference signal: (a) fault of a planet gear and (b) fault of a sun gear.

meshing period is highlighted with a dotted box where f_s samples are included. Because the HD-map for the sun gear or the HD-map using *FM4* for the planet or sun gear are similar to Figure 6-4 under the healthy condition, they are not represented in this chapter. Results of HD-maps under the faulty condition are presented in Chapter 6.5 with the case studies.

6.4 Encoder-less Health Data Map

Hilbert transform (HT) operates convolution of the signal by 1/πt, which can be defined as [102]:

$$\mathrm{HT}\left(f(t)\right) = \hat{f}(t) = f(t) * \frac{1}{\pi t} \tag{6.10}$$

By definition, frequency components of Hilbert transformed signal can be

expressed as:

$$\hat{F}(w)=\begin{cases} -F(w)i=F(w)e^{-i\frac{\pi}{2}}, & for\ w>0 \\ 0, & for\ w=0 \\ F(w)i=F(w)e^{i\frac{\pi}{2}}, & for\ w<0 \end{cases} \tag{6.11}$$

Using this property, an analytic signal can be defined as [103]:

$$z=f(t)+i\hat{f}(t) \tag{6.12}$$

where frequency component of the analytic signal is expressed as:

$$Z(w)=\begin{cases} 2F(w) & for\ w>0 \\ 0 & for\ w\le 0 \end{cases} \tag{6.13}$$

Because the vibration signal and the analytic signal has identical positive frequency component (i.e., w>0), phase of the vibration signal (i.e., rotational phase of the gear) can be deduced from the phase of the analytic signal. Using the property of the analytic signal, Bonnardot (2005) proposed to perform angular resampling based on the phase information estimated from the vibration signal itself [104]. Later, Coats et al. extended the concept and performed encoder-less TSA [105]. However, because TSA requires an accurate phase information for a signal alignment, encoder-less TSA using Hilbert-based phase estimation could lead to signal distortion through ensemble average in real world with massive noise.

This thesis proposes to draw health data map using a roughly resampled vibration signal based on the Hilbert-based phase estimation method. Because the roughly resampled vibration signal cannot be accurately aligned in real world, step 1 in Figure 6-1 (i.e., averaging signal for one *HTC*) is omitted. Alternatively, roughly resampled vibration signal is directly used to calculate the difference signal for one *HTC* in step 2 of Figure 6-1.

6.5 Case Study

6.5.1 Case Study #1: Analytical Model

To analyze the performance of the proposed method, results from an HD-map for analytical models with faults are presented in this chapter. To simulate the pure effect the modulation characteristics, signal transfer function is designed to have zero at minimum as shown in Figure 3-1. First, the HD-maps for an analytical model with faults of the planet gear and the sun gear are visually compared. The maximum amplitude of the anomalies from a faulty tooth of the gears is set to be 0.1. Second, maximum values of the enveloped difference signal and *FM4* in the HD-map are analyzed in terms of the size of the fault, whose amplitude ranges from 0 to 0.2. For all cases, data for ten cycles of HTC_p and HTC_s are used.

Figure 6-5 represents an HD-map using the enveloped difference signal and *FM4* from the analytic signal of a planetary gearbox where tooth number 5 of the planet gear and sun gear are in a fault condition, respectively. As shown in Figure 6-5 (a), features from a faulty tooth of the planet gear (i.e., T_p=5) are represented

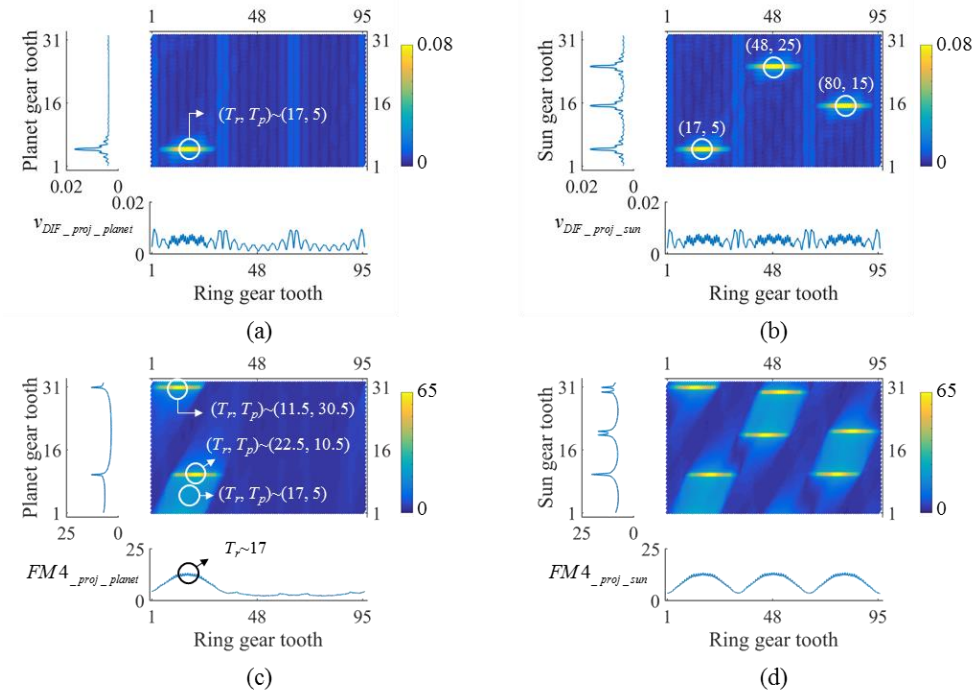

Figure 6-5 Health data map: (a) Difference signal for planet gear fault, (a) Difference signal for sun gear fault, (a) FM4 for planet gear fault and (d) FM4 for sun gear fault

as a horizontal line around the corresponding tooth in the *y*-axis. Because vibration signals from the planet gear of interest are designed to have maximum amplitude around tooth number 17 of the ring gear (i.e., T_r=17), features from a faulty tooth of the planet gear are actually represented as a localized horizontal line with a limited range in the *x*-axis. It is noteworthy that the features from the faulty tooth of the planet gear can also be identified from the projected difference signal, which is located on left side of *y*-axis in Figure 6-5 (a). However, due to the low density in the x-axis, the projected difference signal on the ring gear

tooth domain does not clearly represent the faulty condition.

On the other hand, as shown in Figure 6-5 (b), faults of the sun gear are represented as multiple horizontal lines; as many as the number of planet gears. This is because a faulty tooth in the sun gear actually meshes with the multiple planet gears. Although the sun gear meshes with multiple planet gears, it should be noted that the teeth numbers of the sun gear are assigned in order of the meshing sequence with the first planet gear, as shown in Figure 2-6. To explain this phenomenon, Figure 6-6 (a) and (b) respectively illustrate the positions of the gears at the initial state and at the instance that the faulty tooth of the sun gear (i.e., T_s=5) meshes with the second planet gear (i.e., Planet #2) positioned under the sensor. At that instance, the first planet gear (i.e., Planet #1) meshes with tooth number 25 of the sun gear (i.e., T_s=25) and tooth number 48 of the ring gear (i.e., T_r=48) simultaneously. The horizontal line is thus localized around tooth

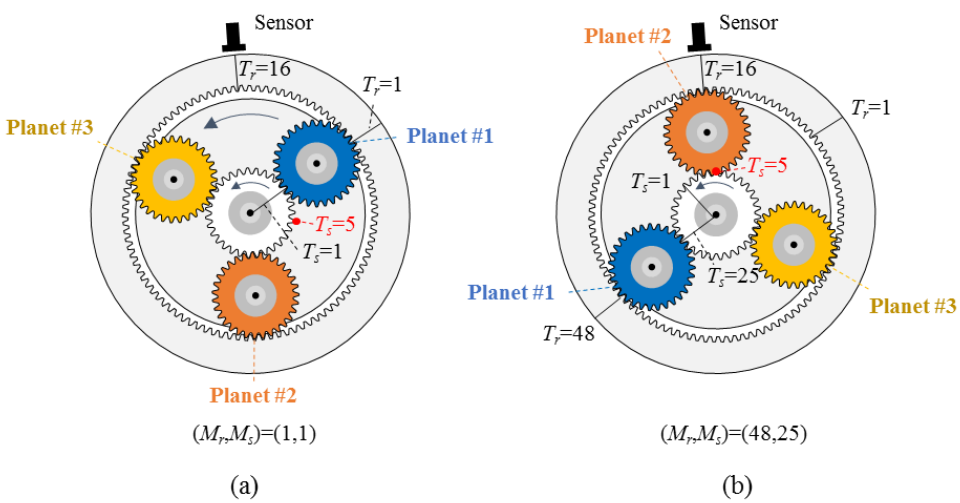

Figure 6-6 Positions of the planet gears: (a) initial state and (b) instance that the faulty tooth of the sun gear meshes with planet #2 under the sensor

number 48 of the ring gear (i.e., 48 at *y*-axis in Figure 6-5 (b)). Likewise, a third horizontal line around 80 and 15 of *x*-axis and *y*-axis is generated by the third planet gear (i.e., Planet #3) meshing with the faulty tooth of the sun gear. The three anomalies per rotation of the sun gear can also be identified by the three peaks in the projected difference signal in the *y*-axis.

Figure 6-2 shows that the short-term anomaly in the difference signal is propagated into two peaks in the health data. In a similar way, one horizontal line in the HD-map$_{(vDIF)}$ is divided into two horizontal lines in the HD-map $_{(FM4)}$ with the intervals of the width of the sliding window, as shown in Figure 6-5 (c) and (d). To explain this phenomenon, Figure 6-7 represents a typical range of the tooth-meshing matrix when the faulty tooth of the planet gear is engaged under the sensor. In this case, the fault was seeded to tooth number 5 of the planet gear, and the width of the window was set to be 10, based on Eq. (6.3). The *FM4* in the sliding window has the highest amplitude when the center of the window is around (11.5, 30.5) and (22.5, 10.5) where the number of anomalies included in the sliding window is small. These points can be found in Figure 6-5 (c) with the highest values of *FM4*. In addition, the position of the planet gear with the highest values of health data can be identified in terms of ring gear tooth by the

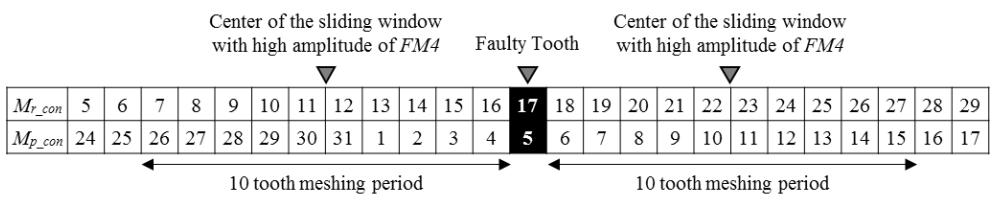

M_{r_con}	5	6	7	8	9	10	11	12	13	14	15	16	**17**	18	19	20	21	22	23	24	25	26	27	28	29
M_{p_con}	24	25	26	27	28	29	30	31	1	2	3	4	**5**	6	7	8	9	10	11	12	13	14	15	16	17

Figure 6-7 Typical range of the tooth-meshing matrix of a ring gear and a planet gear when the faulty tooth of the planet gear is engaged under the sensor

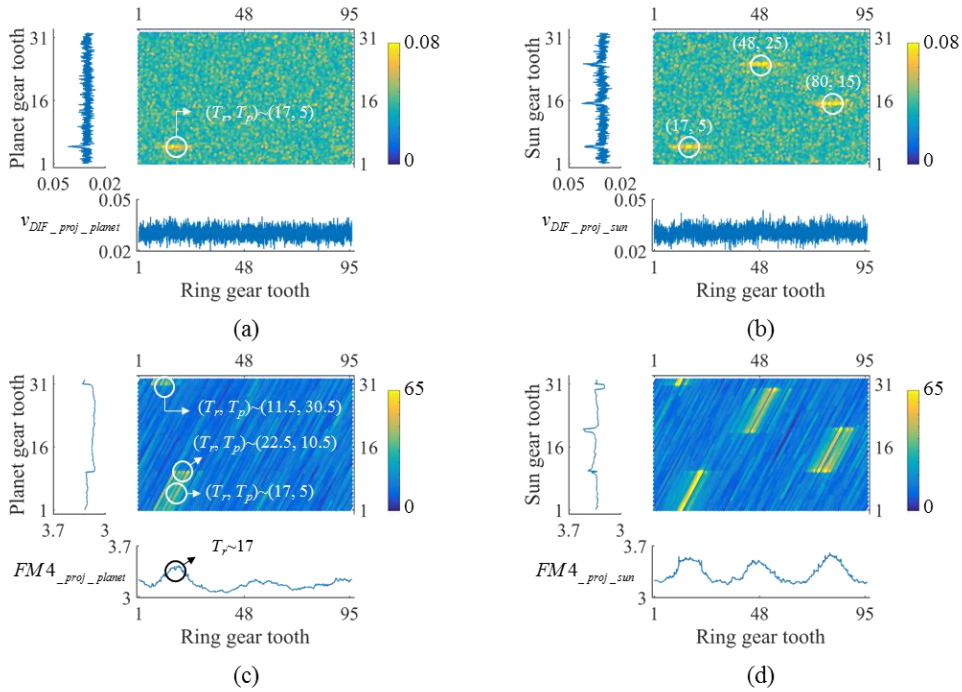

Figure 6-8 Health data map with noise of 0.1: (a) Difference signal for planet gear fault, (b) Difference signal for sun gear fault, (c) FM4 for planet gear fault and (d) FM4 for sun gear fault

projected values in the *x*-axis, as shown in Figure 6-5 (c). For the sun gear fault, similar results are obtained except that three separate lines are divided into six lines, as shown in Figure 6-5 (d).

When the noise of the signal is considered by incorporating 0.1 of A_{noise} in Eq. (3.1), the clear fault-induced features in HD-map are somehow vagued as shown in Figure 6-8. Figure 6-9 quantitatively compares the fault diagnosis performance of the maximum values of the enveloped difference signal and the *FM4* in the sliding window, along with the size of the noise. The enveloped difference signal

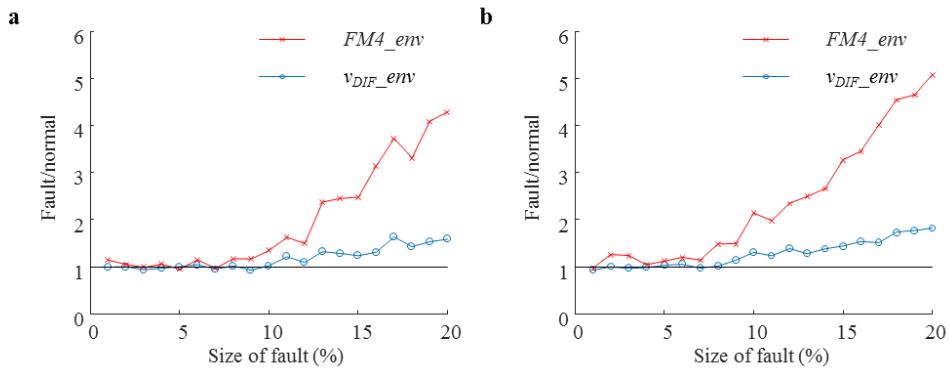

Figure 6-9 Fault diagnosis performance of maximum values of an enveloped difference signal and *FM4*, along with the size of noise: (a) fault of a planet gear and (b) fault of a sun gear.

and the *FM4* from the faulty gearbox are divided by the ones from the normal gearbox. Overall performance of *FM4* in the sliding window to differentiate the faulty condition from the normal condition is shown in this case study to be better than the difference signal.

6.5.2 Case Study #2: Testbed

The second case study described in this chapter employs a 2-kw testbed equipped a one-stage planetary gearbox with configuration of Z_r=95, Z_p=31, Z_s=31, and N_p=3, as shown in Chapter 3.2. The testbed was operated with speed and torque profiles measured from a real wind turbine to simulate the slight speed fluctuations that occur even under stationary operating conditions of the system. A detailed description of the stationary operating conditions of a wind turbine can be found in [24]. For this purpose, two motors (i.e., Motor 1 and Motor 2 in Figure 3-3) were controlled based on a speed and scaled torque

measured from the wind turbine, respectively.

To analyze the effect of the relative distance of the planet gears from the sensor, two sensors – indicated as Sensor # 1 and #2 in Figure 6-10 – are mounted with a 45-degree interval on the gearbox housing around tooth number 1 and 84 of the ring gear (i.e., T_r=1 and 84). From each sensor, vibration signals are measured with sampling rate of 25.6 kHz. A surface defect was seeded on tooth number 1 of a planet gear (Figure 3-5 (c)) and a sun gear (Figure 3-5 (d)) to emulate a faulty condition of the gearbox. For each test, initial position of the gears was set to be identical to Figure 2-6. According to the assembled direction of the planet gear, the tooth with a surface defect contacts either the ring gear or the sun gear [60]. In this research, the planet gear was assembled in such a way that the faulty tooth surface meshed with the ring gear. In addition, the position of the gears was tracked in real-time by means of a high-quality encoder system connected to a high-speed shaft of the gearbox.

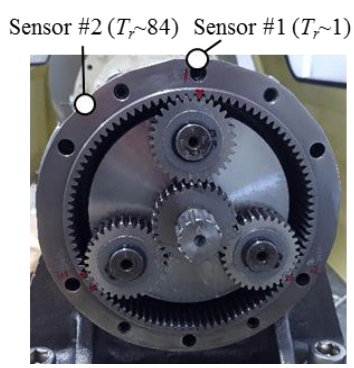

Figure 6-10 Planetary gearbox with two sensors

HDmap with encoder system

Results of the proposed method for the testbed signal are shown in Figure 6-11 and Figure 6-12. In Figure 6-11 (a) and (c), the anomalies and the highlighted range in the x-axis are marked with the dotted circles and lines, respectively. From the results, using sensor # 1 in Figure 6-11 (a), fault-related features by the faulty tooth of the planet gear (i.e., T_p=1) are highlighted localized around typical ranges of the ring gear (i.e., $7<T_r<26$, $37<T_r<47$ and $60<T_r<77$). These ranges are similar to the results using sensor # 2, as shown in Figure 6-11 (c). This is also found from the projected *FM4* on the x-axis, as shown in Figure 6-12 (a) and (c), where the health data are maximized around tooth numbers 13, 43, and 77 of the ring gear. From the results, it can be deduced that the vibration signal is undesirably modulated to have maximum amplitude at a typical location of the ring gear, regardless of the positions of the sensors. Even under these kinds of undesired vibration modulation, the results show that the proposed method performs well. Figure 6-11 (b) and (d) show that multiple localized horizontal lines are generated by the faulty tooth of the sun gear. In this case, fault-related features could be found from almost the entire range of the ring gear tooth domain. These kinds of flat-like modulation characteristics can be made by the geometrical and operational properties of the gearbox [66]. This phenomenon is also represented in Figure 6-12 (b) and (d), although slight modulations are visible from the projected *FM4* on the x-axis.

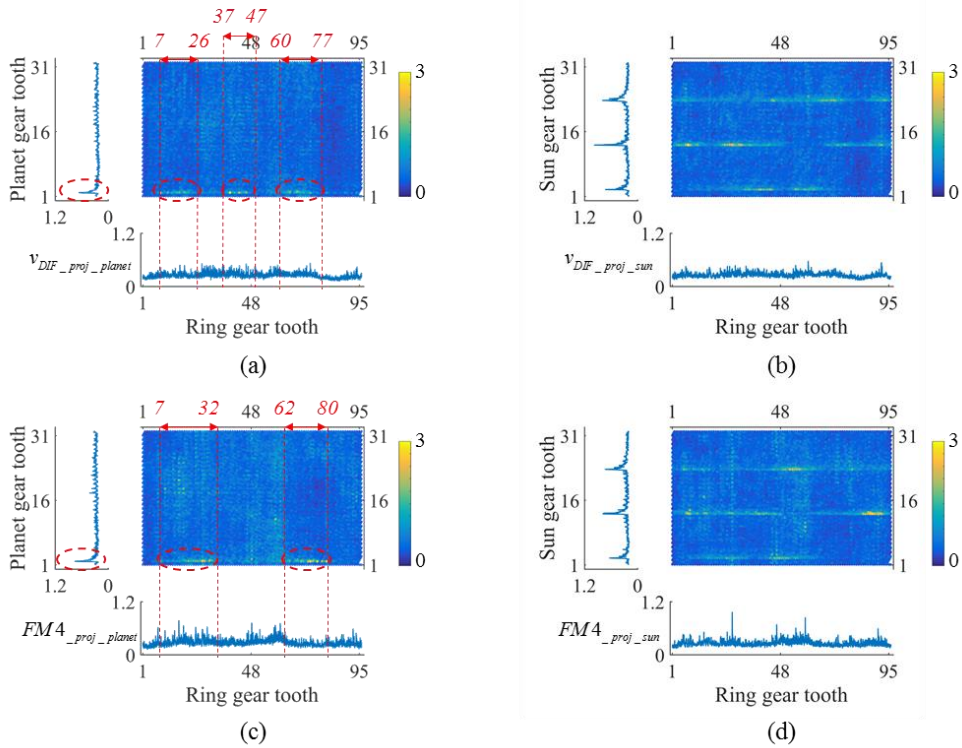

Figure 6-11 Health data map using an enveloped difference signal: (a) fault of a planet gear with Sensor #1, (b) fault of a sun gear with Sensor #1, (c) fault of a planet gear with Sensor #2, (d) fault of a sun gear with Sensor #2.

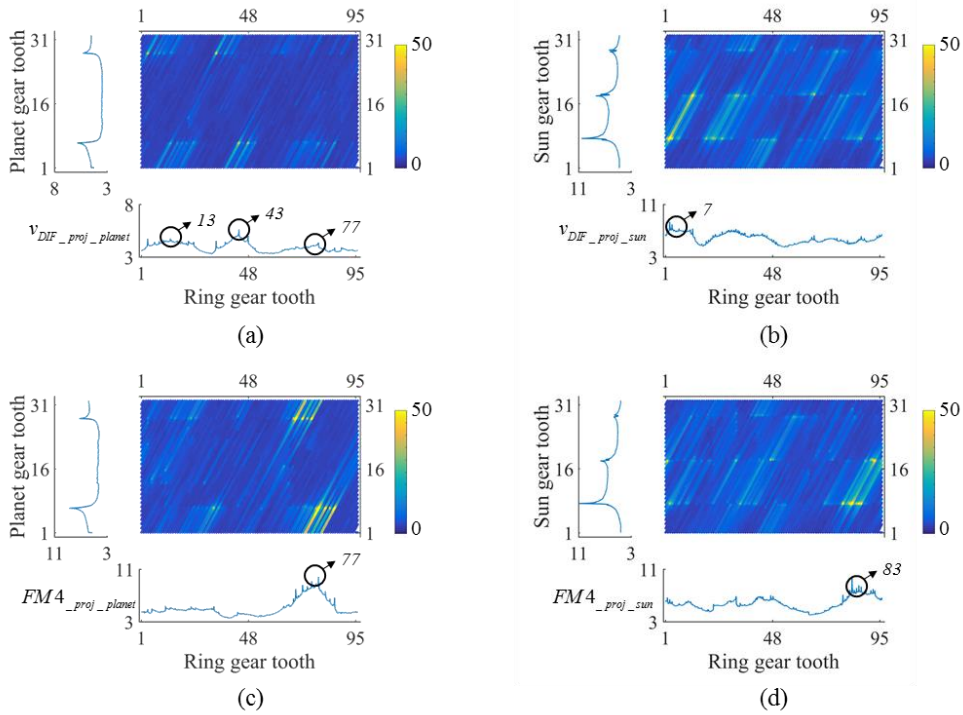

Figure 6-12 Health data map using an enveloped *FM4*: (a) fault of a planet gear with Sensor #1, (b) fault of a sun gear with Sensor #1, (c) fault of a planet gear with Sensor #2, (d) fault of a sun gear with Sensor #2.

To discuss the results, conventional TSA with five-teeth Tukey window function [60] is demonstrated as shown in Figure 6-13 for which vibration signals measured from sensor # 1 in Figure 6-10 is considered. The window function is positioned around tooth number 1 where the sensor # 1 is mounted. As shown in Figure 6-13 (a), difference signal from the planet gear does not show any signature associated with the fault. While fault of the sun gear is represented as small-size anomalies as indicated by the dotted circle in Figure 6-13 (b), they are

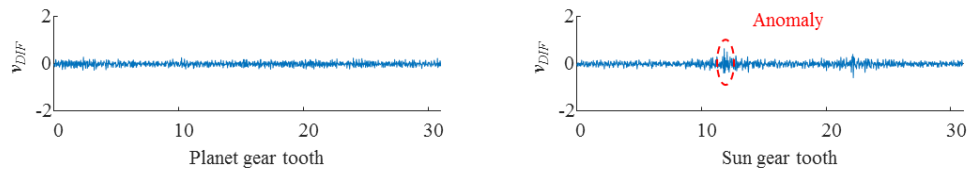

Figure 6-13 Difference signal from sensor # 1 using conventional TSA with five-teeth Tukey window function: (a) fault of a planet gear and (b) fault of a sun gear

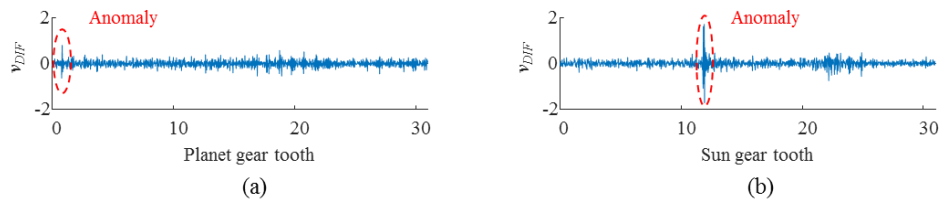

Figure 6-14 Difference signal from sensor # 1 using TSA with adjusted position of the window function: (a) fault of a planet gear with window positioned around T_r=43 and (b) fault of a sun gear with window positioned around T_r=7

uncertain at best. This corresponds to the findings in Figure 6-12 and Figure 6-11 that the fault-related features are not clearly represented around tooth number 1 of the ring gear; they are maximized around tooth number 43 and 7 of the ring gear for the cases of planet gear fault and sun gear fault, respectively. Figure 6-14 represents difference signal where positions of the Tukey window function for TSA are adjusted to tooth number 43 and 7 of the ring gear. The results show that the fault-induced anomalies are clearly represented in tooth domain, which means that they are highlighted around typical location of the ring gear regardless of the position of the sensor due to the uncertain vibration modulation characteristics.

Encoder-less HDmap

For an effective Hilbert-based phase estimation, one should select the most valuable frequency components that can represent the rotational characteristics of the system with high signal-to-noise ratio (SNR). This thesis selects first harmonic of the high speed shaft as the most valuable frequency for phase estimation due to its high local SNR [106]. To reduce the edge effect of the data, second *HTC* is used for the case study. Figure 6-15 represents the phase estimation results which are defined as difference between the phase measured from the encoder system and the phase estimated from the vibration signal. In some cases, the estimated phases have a huge amount of bias error over than 200 degrees, which means that the original positions of the gears cannot be deduced from the results. However, estimated phase has a reasonable range of fluctuation which help to find a rough relative position of the gears in the dataset.

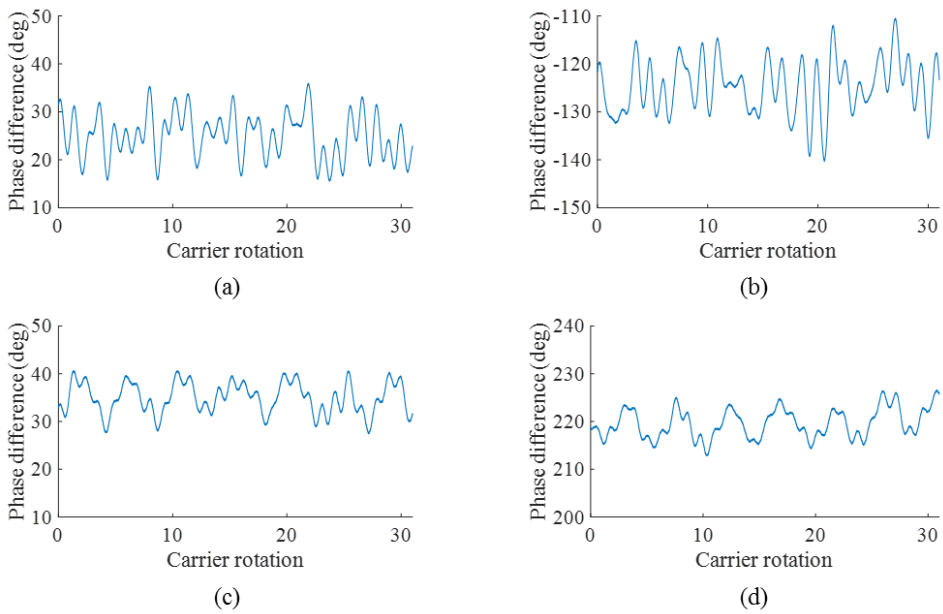

Figure 6-15 Phase estimation results: (a) fault of a planet gear with Sensor #1, (b) fault of a sun gear with Sensor #1, (c) fault of a planet gear with Sensor #2, (d) fault of a sun gear with Sensor #2.

Figure 6-16 and Figure 6-17 represent HDmap drawn without the use of encoder system. Because the TSA couldn't be used, there are noise visible in the HDmap. However, overall features from the faulty tooth of the gears are represented as horizontal lines as shown in the figures. Because the original positions of the gears are missing, horizontal lines are generated at a typical location of HDmap which are not related to the faulty tooth of the gear. In some cases, the horizontal lines caused by faulty tooth of the gears are squashed.

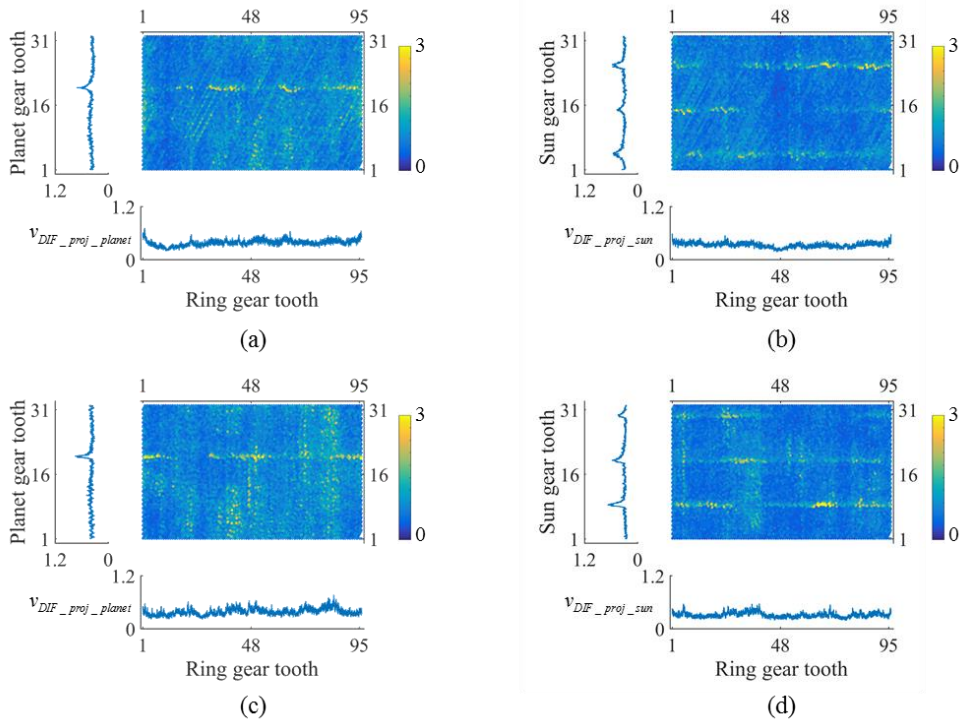

Figure 6-16 Health data map using an enveloped difference signal without encoder system: (a) fault of a planet gear with Sensor #1, (b) fault of a sun gear with Sensor #1, (c) fault of a planet gear with Sensor #2, (d) fault of a sun gear with Sensor #2.

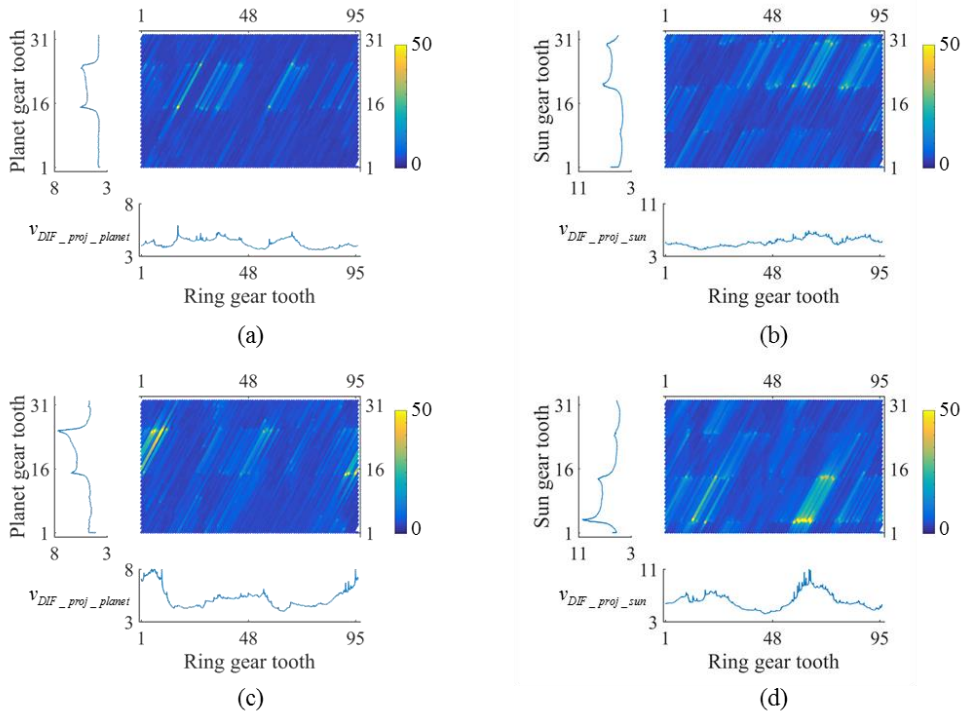

Figure 6-17 Health data map using an enveloped *FM4* without encoder system : (a) fault of a planet gear with Sensor #1, (b) fault of a sun gear with Sensor #1, (c) fault of a planet gear with Sensor #2, (d) fault of a sun gear with Sensor #2.

6.6 Summary and Discussion

This paper presents an original idea to identify a faulty tooth of a planet gear and/or the sun gear in a gearbox through the use of a health data map (i.e., HD-map). By representing time-domain health data in the tooth-domain, tooth-wise fault identification can be performed regardless of the vibration modulation

characteristics of the gearbox. For the case study with the testbed, two sensors were mounted around teeth 1 and 84 of the ring gear. However, it was found that fault-induced anomalies were generated regardless of the position of the sensors because of the uncertain vibration modulation characteristics. This challenge makes the conventional TSA, which extracts the vibration signals at the instances that the planet gears are positioned under the sensor, inapplicable to the real-world case where exact positions of the planet gears cannot be monitored during the entire life of the operation. Moreover, even if the positions of the planet gears are exactly recorded, undesired vibration modulation characteristics induced by the operational and geometrical uncertainties of the gearbox make it unable to determine the optimal position of the narrow-range window function for the conventional TSA. As a case study, it was demonstrated that the conventional TSA filters out the fault-related features by the misuse of the window function under the uncertain vibration modulation characteristics. On the other hand, the proposed method does not employ the vibration extraction window function. Thus, there is no concern about filtering out the significant portion of the signal. In addition, proposed HD-map enables to identify tooth-wise fault in the gearbox through the synthesized visualization of the features in tooth domain. Thus, it can be concluded that the proposed method should outperform conventional TSA with the window function if undesired vibration modulation characteristics occur. In particular, encoder-less HDmap verifies that the proposed fault identification method can be employed even if the position of the inner gears is unknown. Although the HDmap without encoder system has worse results compared to the HDmap with encoder system, fault diagnosis could be performed by the overall trend of HDmap.

Chapter 7. Conclusions

7.1 Contributions and Significance

This thesis presented a vibration-based fault diagnosis technique for planetary gearboxes that is capable of coping with the challenges associated with environmental and operational uncertainties. The research is composed of three research thrusts: 1) quantitative definition of the stationary operating condition, 2) autocorrelation-based time synchronous averaging, and 3) a health data map. The contributions and significance of the research can be summarized as follows.

First, classification of the operating condition was proposed to develop a class-wise condition monitoring strategy under the uncertain operating conditions of the system. Based on a physical understanding of the control logic of a wind turbine, a reasonable qualitative classification method was presented. In addition, quantitative criteria for the stationary operating condition were defined using an empirical PDF and a Gaussian mixture model. The proposed method can be employed to develop an enhanced data acquisition system at the system design stage, or to perform data analysis at the post-processing stage. The proposed method is expected to give a guideline on how to store and analyze the vibration signals considering the fluctuating operating conditions. The method offers the following advantages: i) most of the trivial data that causes unnecessary storage and analysis can be discarded, ii) time-frequency analysis, which requires an extensive amount of computational cost, is only required for Class III conditions, iii) data in the stationary operating condition can be treated as the most valuable

asset, for which readily available condition monitoring techniques can be directly applied, and iv) torque variation is only required to be considered for Class II and Class III conditions. Although this research examined a wind turbine, the proposed classification method can be extended to other kinds of systems that are equipped with a gearbox and where the control logic is given.

Second, data-efficient time synchronous averaging (TSA) was developed with the help of physical understanding of the vibration signals. The proposed method (i.e., ATSA) designed a window function based on the level of similarity of the extracted vibration signals. It gives less weight where the extracted vibration signals have low similarity to reduce the signal distortion that is caused from averaging the heterogeneous signals. An autocorrelation function was employed to quantitatively evaluate the similarity of the extracted vibration signals. The autocorrelation function has been widely used for pattern recognition for time-series classification based on the level of similarity; however, it has never previously been used for evaluation of vibration similarity to design the window function for TSA. Because the proposed method extends the range of the window function with an optimized shape, there is no need to be concerned about importing vibration signals that are out of interest that decrease the signal-to-noise ratio. As a result, the noise reduction performance can be enhanced, even with only a small amount of data. The proposed method is expected to be most useful where a large amount of non-coherent random noise is prevalent during operation of the system.

Third, a health data map was proposed to enable robust, tooth-wise fault diagnosis of a planetary gearbox. The properties of anomalies are characterized

by the vibration modulation characteristics of the gearbox, which is significantly affected by various environmental and operational uncertainties. Conventional TSA with a fixed window function doesn't consider that kind of uncertainty, and filters out most of the out-of-range data. This may lead to removal of the data related to faulty tooth of the gearbox. In contrast, the proposed method utilizes the entire range of the signals to calculate sample-domain health data without using the narrow-range window function. Thus, there is no need to be concerend about removing the signals of ineterest. Because it is time-consuming to identify periodicity of anomalies in the sample domain, this research is proposed to represent the health data in the pairs of teeth of the gears (i.e., ring-planet teeth pairs or ring-sun teeth pairs). The proposed fault identification method helps to easily find the fault-related features from the visualized health data map in the tooth domain.

7.2 Suggestions for Future Research

This thesis performed extensive work to develop a fault diagnosis method for a planetary gearbox under various uncertainties. However, there is room to verify and improve fault diagnosis techniques for planetary gearboxes in future work. We identified several pieces of future work to make the proposed techniques applicable to fault diagnosis of actual gearboxes, which are subjected to various environmental and operating conditions. Subsequent topics that can build upon the research outlined in this thesis are as follows.

- The length of the stationary vibration signal should be long enough for

reliable fault diagnosis of the gearbox. However, data length was not considered in defining the stationary operating condition in this thesis. A real-world system can maintain at the stationary operating condition for only a moment, which cannot generate enough vibration signal for signal processing. In future work, the length of the valuable data should be defined, and this new data set should be considered to define the stationary operating condition of a gearbox.

- The first research thrust reported that torque variation in quasi-stationary operating condition doesn't matter in performing vibration-based fault diagnosis of a gearbox, given the condition that the speed remains almost constant. However, the testbed used for demonstration of the class-wise fault diagnosis method has a torque ranging from 0 to 4 Nm, which is not a significant variation. To verify fault diagnosis in quasi-stationary operating condition, demonstration using a system with a more considerable amount of torque variation should be considered.

- The first research thrust examined a wind turbine that had a control logic designed to maintain the speed and torque at the rated condition to maximize the generating energy. However, most industrial gearboxes would have a different kind of control logic for other purposes. Thus, the proposed method for classification of the operating condition should be extended to various kinds of applications.

- In the second research thrust, ATSA was demonstrated under a slightly varying rotational speed, which can be compensated for using a simple

resampling technique. In future work, the performance of the proposed ATSA should be verified with data that contains a large amount of speed fluctuation. From this verification, it would also be possible to identify with what amount of speed fluctuation TSA remains applicable without any other advanced signal processing techniques. This could be another criterion to define the stationary operating condition in terms of fault diagnosis performance.

- In this thesis, ATSA was demonstrated using a well-controlled testbed that contains less noise than what would be observed in real-world field settings. However, ATSA had a significant impact on reducing massive noise, even with a small amount of data. Thus, the demonstration results would be not enough to fully highlight the advantages of ATSA. In future work, ATSA should be demonstrated using a system that contains a considerable amount of noise.

- It was verified that the fault-related features are highlighted at a typical location of the ring gear with the localized horizontal line in the health data map. To describe the reason, this thesis presented references reporting that vibration modulation characteristics are significantly affected by various factors, such as manufacturing and assembly errors. In future work, vibration modulation characteristics of the gearbox should be deeply studied using a dynamics model or an analytical model to verify the reason for the highlighted features in the health data map. These models would help to 1) advance the health data map and 2) quantify the health data map based on physical meanings.

- Hilbert-based phase estimation was employed to draw the health data map without an encoder system. However, it is well known that Hilbert-based phase estimation is applicable to only a slight amount of speed variation. Thus, in future work, other kinds of phase estimation methods (e.g., peak detection of time-frequency analysis) should be considered for development of an encoder-less health data map.

- It was not easy to gather condition monitoring signals under the anomaly conditions from an actual system with a gearbox. As an alternative, the research described in this thesis employed a two kilowatt gearbox testbed. However, in real field, gearbox is exposed to the uncontrollable and noisy operating condition which makes the signal to noise ratio low. Moreover, typical gearbox from the real field have larger size than the gearbox from the testbed, which may affect the vibration characteristics. In future research, proposed condition monitoring techniques should be demonstrated with the signals measured from real field.

References

1. Y. Feng, P. J. Tavner, H. Long, and J. W. Bialek, “Review of early operation of UK Round 1 offshore wind farms,” *IEEE PES Gen. Meet.*, pp. 1–8, Jul. 2010.

2. J. Land and C. Weitzman, “How HUMS systems have the potential of significantly reducing the direct operating cost for modern helicopters through monitoring,” in *ANNUAL FORUM PROCEEDINGS-AMERICAN HELICOPTER SOCIETY*, 1995, vol. 51, p. 744.

3. D. Mcmillan and G. W. Ault, “Quantification of condition monitoring benefit for offshore wind turbines,” *Wind Eng.*, vol. 31, no. 4, pp. 267–285, 2007.

4. Honeywell, “Study Documents Economic Benefits of HUMS.”

5. S. Sheng, “Investigation of various condition monitoring techniques based on a damaged wind turbine gearbox,” in *Proceedings of 8th International Workshop on Structural Health Monitoring*, 2011, no. October.

6. F. P. García Márquez, A. M. Tobias, J. M. Pinar Pérez, and M. Papaelias, “Condition monitoring of wind turbines: techniques and methods,” *Renew. Energy*, vol. 46, p. 169~178, Oct. 2012.

7. R. Zimroz, W. Bartelmus, T. Barszcz, and J. Urbanek, “Diagnostics of bearings in presence of strong operating conditions non-stationarity—A procedure of load-dependent features processing with application to wind

turbine bearings," *Mech. Syst. Signal Process.*, vol. 46, no. 1, pp. 16–27, May 2014.

8. E. M. Huff, M. Field, and M. Mosher, "An Experimental Comparison of Transmission Vibration Responses from OH-58 and AH-1 Helicopters," 2001.

9. D. Zappal, P. J. Tavner, C. J. Crabtree, and S. Sheng, "Side-band algorithm for automatic wind turbine gearbox fault detection and diagnosis," *IET Renew. Power Gener.*, vol. 8, no. 4, pp. 380–389, 2014.

10. C. J. Stander, P. S. Heyns, and W. Schoombie, "Using vibration monitoring for local fault detection on gears operating under fluctuating load conditions," *Mech. Syst. Signal Process.*, vol. 16, no. 6, pp. 1005–1024, Nov. 2002.

11. C. J. Crabtree, Y. Feng, and P. J. Tavner, "Detecting Incipient Wind Turbine Gearbox Failure : A Signal Analysis Method for On-line Condition Monitoring," in *European Wind Energy Conference (EWEC 2010)*, 2010, no. Ewec.

12. M. Yang and V. Makis, "ARX model-based gearbox fault detection and localization under varying load conditions," *J. Sound Vib.*, vol. 329, no. 24, pp. 5209–5221, Nov. 2010.

13. N. Baydar and A. Ball, "Detection of gear deterioration under varying load conditions by using the instantaneous power spectrum," *Mech. Syst. Signal Process.*, vol. 14, no. 6, pp. 907–921, Nov. 2000.

14. P. J. Dempsey and J. J. Zakrajsek, “Minimizing Load Effects on NA4 Gear Vibration Diagnostic Parameter,” in *Proceedings of the 55th Meeting of the Society for Machinery Failure Prevention Technology.*, 2001.

15. W. Bartelmus, F. Chaari, R. Zimroz, and M. Haddar, “Modelling of gearbox dynamics under time-varying nonstationary load for distributed fault detection and diagnosis,” *Eur. J. Mech. - A/Solids*, vol. 29, no. 4, pp. 637–646, Jul. 2010.

16. D. Toshkova, N. Lieven, P. Morrish, B. Titurus, N. Brinkworth, and W. Moore, “Gearbox condition monitoring under variable operational conditions,” in *7th European Workshop on Structural Health Monitoring*, 2014.

17. L. F. Villa, A. Reñones, J. R. Perán, and L. J. de Miguel, “Statistical fault diagnosis based on vibration analysis for gear test-bench under non-stationary conditions of speed and load,” *Mech. Syst. Signal Process.*, vol. 29, pp. 436–446, May 2012.

18. W. Bartelmus and R. Zimroz, “A new feature for monitoring the condition of gearboxes in non-stationary operating conditions,” *Mech. Syst. Signal Process.*, vol. 23, no. 5, pp. 1528–1534, Jul. 2009.

19. Z. Chen, Z. Zhu, and Y. Shao, “Fault feature analysis of planetary gear system with tooth root crack and flexible ring gear rim,” *Eng. Fail. Anal.*, vol. 49, pp. 92–103, 2015.

20. A. Bodas and A. Kahraman, “Influence of carrier and gear manufacturing

errors on the static load sharing behavior of planetary gear sets," *JSME Int. J. Ser. C*, vol. 47, no. 3, pp. 908–915, 2004.

21. G. U. Xiaoyu, "Influence of planet position errors and eccentricities on planetary gear dynamics," L'INSTITUT NATIONAL DES SCIENCES APPLIQUEES DE LYON, 2012.

22. P. Ma and M. Botman, "Load sharing in a planetary gear stage in the presence of gear errors and misalignment," *J. Mech. Transm. Autom. Des.*, vol. 107, no. 1, pp. 4–10, Mar. 1985.

23. W. Bartelmus and R. Zimroz, "Vibration condition monitoring of planetary gearbox under varying external load," *Mech. Syst. Signal Process.*, vol. 23, no. 1, pp. 246–257, Jan. 2009.

24. J. M. Ha, H. Oh, J. Park, and B. D. Youn, "Classification of operating conditions of wind turbines for a class-wise condition monitoring strategy," *Renew. Energy*, vol. 103, pp. 594–605, 2017.

25. Y. Lei, J. Lin, M. J. Zuo, and Z. He, "Condition monitoring and fault diagnosis of planetary gearboxes: A review," *Meas. J. Int. Meas. Confed.*, vol. 48, no. 1, pp. 292–305, 2014.

26. J. Lin, "A Review and strategy for the diagnosis of speed- varying machinery," in *Prognostics and Health Management (PHM), 2014 IEEE Conference on. IEEE*, 2014.

27. W. Bartelmus and R. Zimroz, "A new feature for monitoring the condition of gearboxes in non-stationary operating conditions," *Mech. Syst. Signal*

Process., vol. 23, no. 5, pp. 1528–1534, Jul. 2009.

28. International Electrotechnical Commission (IEC), “Wind turbines: communications for monitoring and control of wind power plants - Logical node classes and data classes for condition monitoring,” 2007.

29. W. Yang, P. J. Tavner, C. J. Crabtree, Y. Feng, and Y. Qiu, “Wind turbine condition monitoring: Technical and commercial challenges,” *Wind Energy*, vol. 17, no. 5. pp. 673–693, 2014.

30. Germanischer Lloyd (GL), “Rules and guidelines industrial services part 4 - guideline for the certification of condition monitoring systems for wind turbines,” Germanischer Lloyd (GL), 2013.

31. C. J. Crabtree, D. Zappala, and P. J. Tavner, “Survey of commercially available condition monitoring systems for wind turbines,” Technical Report of the University of Durham, 2011.

32. Harry Timmerman, “SKF WindCon - condition monitoring system for wind turbines,” in *New Zealand Wind Energy Conference 2009*, 2009.

33. “Lifetime reliability for wind turbines,” Acoem group, 2012.

34. D. Hochmam and M. Sadok, “Theory of synchronous averaging,” in *IEEE Aerospace Conference Proceedings*, 2004, pp. 3636–3653.

35. P. D. McFadden, “A revised model for the extraction of periodic waveforms by time domain averaging,” *Mech. Syst. Signal Process.*, vol. 1, no. 1, pp. 83–95, Jan. 1987.

36. P. D. McFadden, “Interpolation techniques for time domain averaging of gear vibration,” *Mech. Syst. Signal Process.*, vol. 3, no. 1, pp. 87–97, Jan. 1989.

37. H. J. Decker and J. J. Zakrajsek, “Comparison of interpolation methods as applied to time synchronous averaging,” NASA/TM—1999-209086, NASA Glenn Research Center, Cleveland, Ohio, 1999.

38. M. Lebold, K. Mcclintic, R. Campbell, C. Byington, and K. Maynard, “Review of vibration analysis methods for gearbox diagnostics and prognostics,” in *Proceedings of the 54th Meeting of the Society for Machinery Failure Prevention Technology*, 2000, pp. 623–634.

39. P. D. McFadden, “Examination of a technique for the early detection of failure in gears by signal processing of the time domain average of the meshing vibration,” *Mech. Syst. Signal Process.*, vol. 1, no. 2, pp. 173–183, Apr. 1987.

40. Y. Li, K. Ding, G. He, and H. Lin, “Vibration mechanisms of spur gear pair in healthy and fault states,” *Mech. Syst. Signal Process.*, vol. 81, pp. 183–201, 2016.

41. P. D. Samuel and D. J. Pines, “A review of vibration-based techniques for helicopter transmission diagnostics,” *J. Sound Vib.*, vol. 282, no. 1–2, p. 475~508, Apr. 2005.

42. P. Večeř, M. Kreidl, and R. Šmíd, “Condition indicators for gearbox condition monitoring systems,” vol. 45, no. 6, pp. 35–43, 2005.

43. J. J. Zakrajsek, “A review of transmission diagnostics research at NASA Lewis research center,” National Aeronautics and Space Administration (NASA), Army Research Laboratory, ARL-TR-599, 1994.

44. A. Aherwar and M. S. Khalid, “Vibration analysis techniques for gearbox diagnostic: a review,” *Int. Jouranl Adv. Eng. Technol.*, 2012.

45. A. H. P. and E. M. H. M. Mosher, “Evaluation of standard gear metrics in helicopter flight operation,” in *56th Mechanical failure Prevention Technology Conference*, 2002, pp. 4–11.

46. R. M. Stewart, “Some useful data analysis techniques for gearbox diagnostics,” MHM/R/10/77, Machine Health Monitoring Group, Institute of Sound and Vibration Research, University of Southampton, Southampton, 1977.

47. M. A. Alattas and M. O. Basaleem, “Statistical analysis of vibration signals for monitoring gear condition,” *Damascus Univ. J.*, vol. 23, no. 2, 2007.

48. J. Hanna, C. Hatch, M. Kalb, A. Weiss, and H. Luo, “Detection of wind turbine geartooth defects using sideband energy ratio,” in *China Wind Power 2011*, 2011.

49. S. Sheng, “Wind turbine gearbox condition monitoring round robin study – vibration analysis,” Technical Report NREL/TP-5000-54530, National Renewable Energy Laboratory (NREL), 2012.

50. J. J. Zakarjsek, D. P. Townsend, H. J. Decker, J. J. Zakrajsek, D. P. Townsend, and H. J. Decker, “An analysis of gear fault detection methods

as applied to pitting fatigue failure data," NASA TM-105950 / AVSCOM 92-C-035, NASA Lewis Research Center, Cleveland, Ohio, 1993.

51. H. J. Decker, R. F. Handschuh, and J. J. Zakrajsek, "An enhancement to the NA4 gear vibration diagnostic parameter," 1994.

52. H. R. Martin, "Statistical moment analysis as a means of surface damage detection," in *Proceedings of the 7th International Modal Analysis Conference*, 1989.

53. N. Sawalhi, R. B. Randall, and H. Endo, "The enhancement of fault detection and diagnosis in rolling element bearings using minimum entropy deconvolution combined with spectral kurtosis," *Mech. Syst. Signal Process.*, vol. 21, no. 6, pp. 2616–2633, 2007.

54. J. Mączak, "Local meshing plane analysis as a source of information about the gear quality," *Mech. Syst. Signal Process.*, vol. 38, no. 1, pp. 154–164, 2013.

55. Z. Feng and M. J. Zuo, "Vibration signal models for fault diagnosis of planetary gearboxes," *J. Sound Vib.*, vol. 331, no. 22, pp. 4919–4939, Oct. 2012.

56. P. D. McFadden and I. M. Howard, "The detection of seeded faults in an epicyclic gearbox by signal averaging of the vibration," AR-006-087 / ARL-PROP-R-183, Commonwealth of Australia, Austrailia, 1990.

57. A. Hood and P. Darryll, "Sun gear fault detection on an OH-58C helicopter transmission," in *American Helicopter Society 67th Annual Forum*, 2011,

pp. 1664–1690.

58. P. D. McFadden, “A Technique for calculating the time domain averages of the vibration of the individual planet gears and the sun gear in an epicyclic gearbox,” *J. Sound Vib.*, vol. 144, no. 1, p. 163~172, 1991.

59. P. D. McFadden, “Window functions for the calculation of the time domain averages of the vibration of the individual planet gears and sun gear in an epicyclic gearbox,” *J. Vib. Acoust.*, vol. 116, no. 2, pp. 179–187, Apr. 1994.

60. D. G. Lewicki, R. T. Ehinger, and J. Fetty, “Planetary gearbox fault detection using vibration separation techniques,” NASA/TM—2011-217127, NASA Glenn Research Center, Cleveland, Ohio, 2011.

61. M. R. de Smidt, “Internal vibration monitoring of a planetary gearbox,” Master of Engineering, Department of Mechanical and Aeronautical Engineering, University of Pretoria, 2009.

62. P. D. Samuel, J. K. Conroy, and D. J. Pines, “Planetary transmission diagnostics,” NASA/CR-2004-213068, NASA Glenn Research Center, Cleveland, Ohio, 2004.

63. J. Yu, “Early fault detection for gear shaft and planetary gear based on wavelet and hidden markov modeling,” Ph.D. Thesis, Department of Mechinical and Industrial Engineering, University of Toronto, 2011.

64. B. D. Forrester, “Method for the separation of epicyclic planet gear vibration signatures,” United States patent US 6,298,725 B12001.

65. J. M. Ha, B. D. Youn, H. Oh, B. Han, Y. Jung, and J. Park, "Autocorrelation-based time synchronous averaging for condition monitoring of planetary gearboxes in wind turbines," *Mech. Syst. Signal Process.*, vol. 70–71, 2016.

66. G. D'Elia, E. Mucchi, and M. Cocconcelli, "On the identification of the angular position of gears for the diagnostics of planetary gearboxes," *Mech. Syst. Signal Process.*, vol. 83, pp. 305–320, 2017.

67. X. Liang, M. J. Zuo, and L. Liu, "A windowing and mapping strategy for gear tooth fault detection of a planetary gearbox," *Mech. Syst. Signal Process.*, vol. 80, pp. 445–459, 2016.

68. M. Inalpolat and a. Kahraman, "A theoretical and experimental investigation of modulation sidebands of planetary gear sets," *J. Sound Vib.*, vol. 323, no. 3–5, pp. 677–696, Jun. 2009.

69. R. Patrick, A. Ferri, and G. Vachtsevanos, "Effect of planetary gear carrier-plate cracks on vibration spectrum," *J. Vib. Acoust.*, vol. 134, no. 6, p. 61001, Sep. 2012.

70. C. Vicuña, "Vibration characteristics of single-stage planetary gear transmissions," *Ingeniare. Rev. Chil. Ing.*, vol. 22, pp. 88–98, 2014.

71. P. D. Mcfadden, "An explanation for the asymmetry of the modulation sidebands about the tooth meshing frequency in epicyclic gear vibration," *Proc. Inst. Mech. Eng. , Part C J. Mech. Eng. Sci.*, 1985.

72. Z. Feng and M. J. Zuo, "Vibration signal models for fault diagnosis of

planetary gearboxes," *J. Sound Vib.*, vol. 331, no. 22, pp. 4919–4939, 2012.

73. M. Inalpolat and a. Kahraman, "A theoretical and experimental investigation of modulation sidebands of planetary gear sets," *J. Sound Vib.*, vol. 323, no. 3–5, pp. 677–696, 2009.

74. K. E. Johnson, "Adaptive torque control of variable speed wind turbines," National Renewable Energy Laboratory (NREL) TP-500-36265, 2008.

75. T. Burton, D. Sharpe, N. Jenkins, and E. Bossanyi, *Wind energy handbook*, 2nd ed. John Wiley & Sons, 2001.

76. E. Muljadi and C. P. Butterfield, "Pitch-controlled variable-speed wind turbine generation," *IEEE Trans. Ind. Appl.*, vol. 37, no. 1, pp. 240–246, 2001.

77. W. Hu, K. K. Choi, O. Zhupanska, and J. H. J. Buchholz, "Integrating variable wind load, aerodynamic, and structural analyses towards accurate fatigue life prediction in composite wind turbine blades," *Struct. Multidiscip. Optim.*, 2015.

78. Z. Xi, B. D. Youn, B. C. Jung, and J. T. Yoon, "Random field modeling with insufficient field data for probability analysis and design," *Struct. Multidiscip. Optim.*, vol. 51, no. 3, pp. 599–611, 2015.

79. T. Jin and Z. Tian, "Uncertainty analysis for wind energy production with dynamic power curves," *2010 IEEE 11th Int. Conf. Probabilistic Methods Appl. to Power Syst.*, pp. 745–750, 2010.

80. O. Rodriguez-Hernandez, O. a. Jaramillo, J. a. Andaverde, and J. a. del Río, "Analysis about sampling, uncertainties and selection of a reliable probabilistic model of wind speed data used on resource assessment," *Renew. Energy*, vol. 50, pp. 244–252, 2013.

81. J. F. Manwell, J. G. McGowan, and A. L. Rogers, *Wind energy explained: theory, design and application*, 2nd ed. John Wiley & Sons, 2010.

82. International Electrotechnical Commission (IEC), "IEC 61400-1, Wind turbine-part 1: design requirements," International Electrotechnical Commission (IEC), Switzerland, 2005.

83. J. A. Gubner, *Probability and random processes for electrical and computer engineers*. Cambridge University Press, 2006.

84. L. F. Shampine, "Vectorized adaptive quadrature in MATLAB," *J. Comput. Appl. Math.*, vol. 211, no. 2, pp. 131–140, 2008.

85. M. Lydia, a. I. Selvakumar, S. S. Kumar, and G. E. P. Kumar, "Advanced algorithms for wind turbine power curve modeling," *IEEE Trans. Sustain. Energy*, vol. 4, no. 3, pp. 827–835, 2013.

86. M. S. Waterman and D. E. Whiteman, "Estimation of probability densities by empirical density functions†," *Int. J. Math. Educ. Sci. Technol.*, vol. 9, no. 2, pp. 127–137, 1978.

87. A. W. van der Vaart, *Asymptotic statistics*. Cambridge University Press, 2000.

88. J. E. Bartlett, J. W. Kotrlik, and C. C. Higgins, “Organizational research: determining appropriate sample size in survey research,” *Inf. Technol. Learn. Perform. J.*, vol. 19, no. 1, pp. 43–50, 2001.

89. ASTM International, “ASTM E122-07 Standard practice for calculating sample size to estimate , with specified precision , the average for a characteristic of a lot or process,” *Annu. B. ASTM Stand.*, pp. 1–5, 2009.

90. Y. Feng, Y. Qiu, C. Crabtree, H. Long, and P. Tavner, “Use of SCADA and CMS signals for failure detection and diagnosis of a wind turbine gearbox,” *Ewea*, 2011.

91. D. Reyanolds, “Gaussian mixture models,” *Encycl. Biometrics*, no. 2, pp. 659–663, 2009.

92. R. A. Redner and H. F. Walker, “Mixture densities, maximum likelihood and the EM algorithm,” *Soc. Ind. Appl. Math.*, vol. 26, no. 2, pp. 195–239, 1984.

93. J. M. Ha, B. D. Youn, H. Oh, B. Han, Y. Jung, and J. Park, “Autocorrelation-based time synchronous averaging for condition monitoring of planetary gearboxes in wind turbines,” *Mech. Syst. Signal Process.*, vol. 70–71, pp. 161–175, 2016.

94. B. C. Jeon, J. H. Jung, B. D. Youn, Y.-W. Kim, and Y.-C. Bae, “Datum unit optimization for robustness of a journal bearing diagnosis system,” *Int. J. Precis. Eng. Manuf.*, vol. 16, no. 11, pp. 2411–2425, 2015.

95. Z. Chen, S. Haykin, J. J. Eggermont, and S. Becker, *Correlative learning: A*

basis for brain and adaptive systems. Wiley, 2008.

96. B. Boashash, “Estimating and interpreting the instantaneous frequency of a signal - part 2: algorithms and applications,” *Proc. IEEE*, vol. 80, no. 4, pp. 540–568, 1992.

97. B. Boashash, “Estimating and interpreting the instantaneous frequency of a signal. I. Fundamentals,” *Proc. IEEE*, vol. 80, no. 4, pp. 520–538, 1992.

98. Y. Harpaz, S. E. Robinson, M. Medvedovsky, and A. Goldstein, “Improving the excess kurtosis (g2) method for localizing epileptic sources in magnetoencephalographic recordings,” *Clin. Neurophysiol.*, vol. 126, no. 5, pp. 889–897, 2015.

99. H. J. Decker and D. G. Lewicki, “Spiral bevel pinion crack detection in a helicopter gearbox,” no. June, 2003.

100. C. S. Hilas, I. T. Rekanos, and P. A. Mastorocostas, “Change point detection in time series using higher-order statistics: A heuristic approach,” *Math. Probl. Eng.*, vol. 2013, 2013.

101. A. Poularikas, *The Transforms and Applications Handbook*. CRC-Press, 2000.

102. H. Luo, X. Fang, and B. Ertas, “Hilbert transform and its engineering applications,” *AIAA J.*, vol. 47, no. 4, pp. 923–932, Apr. 2009.

103. M. Feldman, “Hilbert transform in vibration analysis,” *Mech. Syst. Signal Process.*, vol. 25, no. 3, pp. 735–802, Apr. 2011.

104. F. Bonnardot, M. El Badaoui, R. B. Randall, J. Danière, and F. Guillet, “Use of the acceleration signal of a gearbox in order to perform angular resampling (with limited speed fluctuation),” *Mech. Syst. Signal Process.*, vol. 19, no. 4, pp. 766–785, Jul. 2005.

105. M. D. Coats and R. B. Randall, “Order-tracking with and without a tacho signal for gear fault diagnostics,” *Aust. Acoust. Soc. Conf. 2012, Acoust. 2012 Acoust. Dev. Environ.*, no. November, pp. 447–454, 2012.

106. F. Combet and L. Gelman, “An automated methodology for performing time synchronous averaging of a gearbox signal without speed sensor,” *Mech. Syst. Signal Process.*, vol. 21, no. 6, pp. 2590–2606, 2007.

Abstract (Korean)

유성 기어박스의 진동 기반 고장진단 기법은 대형 공학 시스템의 유지보수 비용을 절감시킬 수 있는 효과적인 방법으로 알려져 있다. 하지만 다양한 환경 및 운행적 불확실성이 기어박스의 진동 특성에 심각한 영향을 미치는 경우 이러한 진동 기반 고장진단 기법의 성능이 저하된다는 문제가 있다. 이 논문에서는 다양한 불확실성에 의해 발생할 수 있는 유성 기어박스의 진동기반 고장진단의 문제점들을 해결하기 위해 세 가지 연구 주제를 제안한다. 첫 번째는 정상(stationary) 운행 조건의 정량적 정의이고, 두 번째는 데이터 활용성이 뛰어난 자기상관함수 기반 시간 동기 평균화 기법의 개발이며, 세 번째는 엔코더 장비 없이 어느 진동 특성에서도 사용할 수 있는 건전성 데이터 맵 기반 기어 치별 고장 판별 기법 개발이다. 첫 번째 연구 주제에서는 불확실한 환경 및 운행 조건에서부터 발생할 수 있는 고장 진단의 문제를 해결하기 위해 운행 환경별 고장 진단 전략을 제안한다. 제안된 방법은 기어박스의 운행 환경을 다양한 클래스로 나누어, 각 클래스에서 동질의 진동 신호를 측정할 수 있도록 하는 것을 특징으로 한다. 두 번째 연구 주제에서는 기존 시간 동기 평균화의 문제를 해결하기 위한 과정을 소개한다. 유성 기어박스를 위한 기존 시간 동기 평균화 기법은 노이즈 대비 신호 크기를 향상시키기 위해 좁은 범위의 윈도우 함수를 사용하여 특정 범위의 진동 신호를 추출하는 과정을 동반한다. 하지만 이 경우 대부분의 윈도우 함수 범위 밖의 신호를 활용하지 않기 때문에, 운행적 불확실성이 내제된 실제 현장에서 측정할 수 없을 정도의

대량의 데이터를 필요로 한다. 이 논문에서는 자기 상관함수에 기반하여 진동 추출 윈도우 함수의 범위를 확장하고 최적 형상을 설계함으로써 적은 양의 신호만으로도 효과적인 고장 진단을 가능하게 하기 위한 방법을 제안한다. 세 번째 연구 주제에서는 불확실한 진동 특성을 갖는 기어 박스에서도 기어 치별 고장 판별이 가능하도록 하는 방법을 제안한다. 논문에서 제안된 2차원의 건전성 데이터 맵은 기어 치들의 모든 가능한 조합에 대해 건전성을 평가함으로써 고장 기어의 위치를 판별할 수 있도록 한다. 또한 힐버트 변환에 기반한 위상 추정 기법을 활용하여 엔코더 장비 없이도 건전성 데이터 맵을 그릴 수 있는 방법을 제안하였으며, 작은 양의 속도 변화에 노출된 경우에도 활용이 가능하다는 것을 증명하였다.

주제어: 고장 진단
유성 기어박스
운행 데이터 분류
자기상관함수 기반 시간 동기 평균화
건전성 데이터 맵

학 번: 2013-30953

This work was supported by the Technology Innovation Program (10050980, System Level Reliability Assessment and Improvement for New Growth Power Industry Equipment) funded by the Ministry of Trade, Industry and Energy (MI, Korea).